Department of Micro and Nanosciences

Electrical properties of granular semiconductors – Modelling and experiments on metal-oxide gas sensors

Aapo Varpula

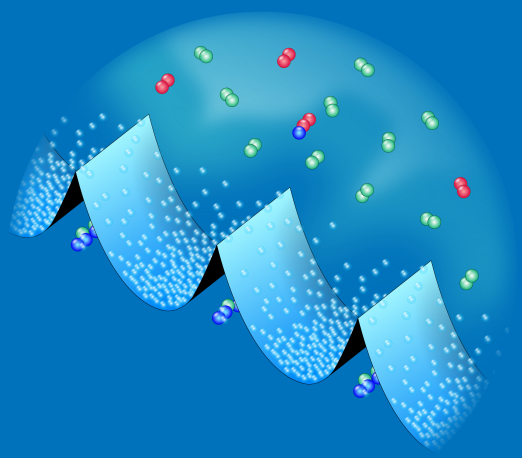

Aalto University

DOCTORAL DISSERTATIONS

Aalto University publication series
DOCTORAL DISSERTATIONS 21/2011

Electrical properties of granular semiconductors – Modelling and experiments on metal-oxide gas sensors

Aapo Varpula

Doctoral dissertation for the degree of Doctor of Science in Techology to be presented with due permission of the School of Electrical Engineering for public examination and debate in the Large Seminar Hall of Micronova at the Aalto University (Espoo, Finland) on the 8th of April 2011 at 12 noon

Aalto University
School of Electrical Engineering
Department of Micro and Nanosciences
Electron Physics Group

Supervisor
Professor Pekka Kuivalainen

Preliminary examiners
Professor Tapio Rantala, Tampere University of Technology, Finland
Dr. Simo Eränen, VTT Technical Research Centre of Finland

Opponent
Professor János Mizsei, Budapest University of Technology and Economics, Hungary

Aalto University publication series
DOCTORAL DISSERTATIONS 21/2011

ISBN 978-952-60-4063-9 (pdf)
ISBN 978-952-60-4062-2 (printed)
ISSN-L 1799-4934
ISSN 1799-4942 (pdf)
ISSN 1799-4934 (printed)

Aalto Print
Helsinki 2011

The dissertation can be read at http://lib.tkk.fi/Diss/2011/isbn9789526040639/

Aalto University

Abstract

Aalto University, P.O. Box 11000, FI-00076 Aalto www.aalto.fi

Author
Aapo Varpula

Name of the doctoral dissertation
Electrical properties of granular semiconductors – Modelling and experiments on metal-oxide gas sensors

Publisher School of Electrical Engineering

Unit Department of Micro and Nanosciences

Series Aalto University publication series DOCTORAL DISSERTATIONS 21/2011

Field of research Semiconductor physics, chemical sensors, electrophysics

Manuscript submitted 15.11.2010 **Manuscript revised** 18.02.2011

Date of the defence 08.04.2011 **Language** English

☐ **Monograph** ☒ **Article dissertation (summary + original articles)**

Abstract

DC, AC, and the transient characteristics of granular n-type semiconductors are modelled using the drift-diffusion theory. The transient model describes the electrical large-signal response to both voltage and temperature changes. The analysis is based on the dynamic electrical model of the grain-boundary region and electronic trapping in the acceptor-type electronic interface states at the grain boundaries.

The use of different approximations in the model derivation results in a simple fully analytical model and a semianalytical model, which requires numerical methods in the solution. The models are verified by performing numerical device simulations with SILVACO ATLAS. The models are also fitted to experimental data. They are in excellent agreement with ATLAS and the experimental data. Compared to ATLAS the transient calculations employing the semianalytical model are four orders of magnitude faster on a standard PC computer, yet having the same accuracy.

The existence of electronic traps at grain boundaries results in nonlinear DC, extraordinary AC, and highly complex and nonlinear transient electrical characteristics. The current–voltage curves can be divided into four characteristic regions: linear, sublinear, superlinear, and series resistance limited regions. The electrical-equivalent-circuit presentations of the AC characteristics have, in addition to the common resistors and capacitors, special RL and RC circuit branches associated with the electronic trapping. These circuit branches have negative admittance.

In the experimental part an atomic-layer-deposited SnO_2 microhotplate gas sensor was designed and fabricated for the first time. The sensors exhibit good response and recovery to ethanol, acetone, and acrylonitrile vapours, and good stability. In addition, the developed model is extended to the case of n-type gas-sensitive surface-type metal oxides. The adsorption of gases is described by a surface-state model. The model is employed in the quantitative explanation of the new effects in metal-oxide gas sensors: the bias-dependent sensitivity and negative admittance effects, which were observed experimentally in commercial WO_3 gas sensors. These effects can be used for increasing the selectivity of the gas sensors.

Keywords Granular semiconductor, micro gas sensor, metal oxide, drift-diffusion theory, electronic trapping

ISBN (printed) 978-952-60-4062-2 **ISBN (pdf)** 978-952-60-4063-9

ISSN-L 1799-4934 **ISSN (printed)** 1799-4934 **ISSN (pdf)** 1799-4942

Pages 144 **Location of publisher** Espoo **Location of printing** Helsinki **Year** 2011

The dissertation can be read at http://lib.tkk.fi/Diss/2011/isbn9789526040639/

Aalto-yliopisto

Tiivistelmä

Aalto-yliopisto, PL 11000, 00076 Aalto www.aalto.fi

Tekijä(t)
Aapo Varpula

Väitöskirjan nimi
Rakeisten puolijohteiden sähköiset ominaisuudet – Mallinnus ja kokeita metallioksidikaasuantureilla

Julkaisija Sähkötekniikan korkeakoulu

Yksikkö Mikro- ja nanotekniikan laitos

Sarja Aalto-yliopiston julkaisusarja VÄITÖSKIRJAT 21/2011

Tutkimusala Puolijohdefysiikka, kemialliset anturit, sähköfysiikka

Käsikirjoituksen pvm 15.11.2010 **Korjatun käsikirjoituksen pvm** 18.02.2011

Väitöspäivä 08.04.2011 **Kieli** Englanti

☐ **Monografia** ☒ **Yhdistelmäväitöskirja (yhteenveto-osa + erillisartikkelit)**

Tiivistelmä

Rakeisten n-tyypin puolijohteiden DC-, AC- ja transienttiominaisuudet mallinnetaan käyttäen drift–diffuusio-teoriaa. Transienttimalli kuvaa sekä jännite- että lämpötilavaihteluista johtuvia sähköisiä suursignaalivasteita. Analyysi perustuu dynaamiseen sähköiseen malliin ja elektroniseen loukkuuntumiseen raerajoilla oleviin akseptori-tyyppisiin elektronisiin rajapintatiloihin.

Käyttämällä eri approksimaatioita mallin johtamisessa päädytään yksinkertaiseen, täysin analyyttiseen malliin sekä puolianalyyttiseen malliin, joka vaatii numeeristen menetelmien käyttöä. Nämä mallit osoitetaan oikeaksi vertaamalla niitä SILVACO ATLAS -ohjelmistolla tehtyihin numeerisiin simulaatioihin. Lisäksi mallit sovitetaan kokeellisiin tuloksiin. Mallien tulokset vastaavat erinomaisesti ATLAS-simulaatiota ja sopivat erinomaisesti kokeellisiin tuloksiin. Puolianalyyttista mallia käyttävä laskenta tavallisella PC-tietokoneella neljä kertaluokkaa vastaavaa ATLAS-simulaatiota nopeampi, vaikka ne ovat yhtä tarkkoja.

Elektronisten loukkujen olemassaolo raerajoilla johtaa epälineaarisiin DC-, poikkeuksellisiin AC-, ja hyvin monimutkaisiin ja epälineaarisiin transienttiominaisuuksiin. Virta–jännite-käyrät voidaan jakaa neljään alueeseen: lineaariseen, alilineaariseen, ylilineaariseen ja sarjavastusrajoitteeseen alueeseen. AC-ominaisuuksien vastinpiiriesityksissä on tavallisten vastusten ja kondensaattoreiden lisäksi elektronien loukkuuntumiseen liittyvät poikkeukselliset RL- ja RC-piirit, joilla on negatiivinen admittanssi.

Kokeellisessa osassa ALD-atomikerroskasvatettua tinadioksidikalvoa käyttävä mikrolämpölevykaasuanturi suunniteltiin ja valmistettiin. Antureilla ovat hyvät vasteet ja palautumiset etanoli-, asetoni- ja akrylonitriilihöyryille sekä hyvä stabiilius. Lisäksi kehitetty malli laajennetaan n-tyyppisten kaasuherkkien pintatyypin metallioksidien tapaukseen. Kaasujen adsorptio mallinnetaan pintatilamallilla. Tätä mallia käytetään metallioksidikaasuantureissa ilmenevien uusien bias-jännitteestä riippuvan herkkyys- ja negatiivinen admittanssi-ilmiöiden selittämiseen. Ilmiöt havaittiin kokeellisesti kaupallisissa WO_3-kaasuantureissa. Näitä ilmiöitä voidaan käyttää kaasuantureiden selektiivisyyden parantamiseen.

Avainsanat Rakeinen puolijohde, mikrokaasuanturi, metallioksidi, drift–diffuusio-teoria, elektronien loukkuuntuminen

ISBN (painettu) 978-952-60-4062-2 **ISBN (pdf)** 978-952-60-4063-9

ISSN-L 1799-4934 **ISSN (painettu)** 1799-4934 **ISSN (pdf)** 1799-4942

Sivumäärä 144 **Julkaisupaikka** Espoo **Painopaikka** Helsinki **Vuosi** 2011

Luettavissa verkossa osoitteessa http://lib.tkk.fi/Diss/2011/isbn9789526040639/

Preface

I thank my supervisors professors Juha Sinkkonen and Pekka Kuivalainen for the opportunity to work in the fascinating field of semiconductor physics and technology and for their guidance in the theoretical part of this work. I am also obliged to Sergey Novikov, whose help was invaluable in the experimental work, as well as for giving insight into chemical science in general.

The financial support from the Graduate School in Electronics, Telecommunications and Automation (GETA), Finnish Foundation for Technology Promotion (Tekniikan edistämissäätiö), Finnish Foundation of Electronics Engineers (Elektroniikkainsinöörien säätiö), and the Nordic Innovation Centre (project Threatgården of the "Everyday Nano" project portfolio of the Nordic MINT initiative) are gratefully acknowledged.

In addition, I thank Marko Yli-Koski and Ville Vähänissi for fruitful discussions on the use of SILVACO® ATLAS™ device simulation software. I am also grateful to Antti Haarahiltunen for commenting on the publications and fruitful discussions on semiconductor physics, to Charlotta Tuovinen for improving my English in the publications, and to William Martin for proofing the final version. I also thank all the people in our joint-research project and publications: Antti J. Niskanen, Mikko Utriainen, Gomathi Natarajan, prof. David C. Cameron, Veli-Matti Airaksinen, and prof. Sami Franssila. Furthermore, I am grateful to all the other people I have worked with over the years, especially Nikolai Chekurov, Kimmo Kokkonen, and Aila Blomberg.

Finally, I thank my family and friends for their encouragement, support, and assistance. Especially, I express my gratitude to my wife Sointu, mother Pirkko, father Timo, and sister Soili.

Otaniemi, Espoo, 18th of February 2011

Matti Aapo Ilari Varpula

List of included publications

This Thesis consists of an overview and the following peer-reviewed publications:

I A. Varpula, J. Sinkkonen, and S. Novikov, *Modelling of dc characteristics for granular semiconductors*, Physica Scripta **T141**, 014003 (2010). doi: 10.1088/0031-8949/2010/T141/014003

II A. Varpula, J. Sinkkonen, and S. Novikov, *Small-signal analysis of granular semiconductors*, Physica Scripta **T141**, 014002 (2010). doi: 10.1088/0031-8949/2010/T141/014002

III A. Varpula, *Modeling of transient electrical characteristics for granular semiconductors*, Journal of Applied Physics **108**, 034511 (2010). doi: 10.1063/1.3457854

IV A. J. Niskanen, A. Varpula, M. Utriainen, G. Natarajan, D. C. Cameron, S. Novikov, V.-M. Airaksinen, J. Sinkkonen, and S. Franssila, *Atomic layer deposition of tin dioxide sensing film in microhotplate gas sensors*, Sensors and Actuators B: Chemical **148**, 227-232 (2010). doi: 10.1016/j.snb.2010.05.018

V A. Varpula, S. Novikov, J. Sinkkonen, and M. Utriainen, *Bias dependent sensitivity in metal-oxide gas sensors*, Sensors and Actuators B: Chemical **131**, 134-142 (2008). doi: 10.1016/j.snb.2007.12.013

VI A. Varpula, S. Novikov, J. Sinkkonen, and M. Utriainen, *Negative admittance in resistive metal oxide gas sensors*, Journal of Physics: Conference Series **100**, 082036 (2008). doi: 10.1088/1742-6596/100/8/082036

Author's contribution

Publications I–III: The author developed the theoretical models based on prof. Juha Sinkkonen's guidance, performed the numerical calculations using MATLAB® and SILVACO® ATLAS™, and wrote the paper.

Publication IV: The author conducted the sensor characterization experiments and contributed to the writing of the paper. Sergey Novikov guided in the planning of the experimental work.

Publications V–VI: The author conducted the experiments, developed the theoretical models based on prof. Juha Sinkkonen's guidance, performed the numerical calculations, and wrote the paper. Sergey Novikov guided in the planning of the experimental work.

Contents

Nomenclature

Abbreviations

1D	One dimension
2D	Two dimensions
3D	Three dimensions
AFM	Atomic force microscope
ALD	Atomic layer deposition
BLM	Brick layer model
CMOS	Complementary metal-oxide-semiconductor
CPU	Central processing unit
CVD	Chemical vapour deposition
CWA	Chemical-warfare agent
DLTS	Deep-level transient spectroscopy
EEC	Electrical equivalent circuit
FEM	Finite element method
FFT	Fast Fourier transform
GB	Grain boundary
GPIB	General purpose interface bus
I–*V*	Electric current–voltage
MBD	Molecular beam deposition
MBE	Molecular beam epitaxy
MFP	Mean free path
OLED	Organic light-emitting diode
PCB	Printed circuit board
PECVD	Plasma-enhanced chemical vapour deposition
PTC	Positive temperature coefficient
PVD	Physical vapour deposition
Region I	The left-hand-side grain-boundary depletion region (see Figs. 5 and 6)
Region II	The right-hand-side grain-boundary depletion region (see Figs. 5 and 6)

RFID	Radio-frequency identification
RGTO	Rheotoxial growth and thermal oxidation
RH	Relative humidity
RMS	Root mean square
SOI	Silicon on insulator
VDR	Voltage-dependent resistor

Chemical symbols and compounds

$BaTiO_3$	Barium titanate
CdS	Cadmium sulfide
CdSe	Cadmium selenide
Cl_2	Chlorine gas molecule
CO	Carbon monoxide
Co_3O_4	Cobalt(II,III) oxide
CuO	Copper(II) oxide
e^-_{free}	A free electron
Fe_2O_3	Iron(III) oxide
GaAs	Gallium arsenide
Ge	Germanium
H_2	Hydrogen gas molecule
H_2S	Hydrogen sulfide
HfO_2	Hafnium(IV) oxide
In_2O_3	Indium(III) oxide
KOH	Potassium hydroxide
NH_3	Ammonia
NiO	Nickel(II) oxide
NO	Nitrogen monoxide
NO_2	Nitrogen dioxide
O^-_{ads}	An ionized oxygen adatom (i.e. adion)
O_2	Oxygen gas molecule

O_3	Ozone
O_{ads}	A chemisorbed neutral oxygen atom (i.e. adatom)
PbS	Lead(II) sulfide
R	A reducing gas molecule
S_{ads}	An adsorption site
Si	Silicon
SiC	Silicon carbide
SiO_2	Silicon dioxide
SnO_2	Tin dioxide
$SrTiO_3$	Strontium titanate
TiO_2	Titanium dioxide
WO_3	Tungsten trioxide
ZnO	Zinc oxide

Quantities and variables

α_J	The exponent of the electric current–voltage (I–V) curve, $J_{DC} \propto U_{DC}^{\alpha_J}$
α_R	The parameter determing how strongly the reducing gas removes the oxygen ions
$\Delta\nu$	The magnitude of change of ν
ΔT	The step change in temperature
ΔU_{GB}	The step change in voltage
$\Im\{Y\}$	The imaginary part of the admittance
$\mathcal{I}_I$	The integral in Eqs. 13–16
$\mathcal{I}_{II}$	The integral in Eqs. 13–16
$\mathcal{I}_{tot}$	The integral in Eqs. 13–16
i	The imaginary unit
μ	The mobility of electrons
ν	The normalized density of the occupied electronic grain-boundary states, $\nu = N_B/N_B^{eq}$
ν_0	The normalized density of the occupied grain-boundary states before the step change
ν_{DC}	The normalized density of the occupied electronic grain-boundary states in the steady state
ω	The angular frequency

ϕ	The electric potential
$\Re\{Y\}$	The real part of the admittance (i.e. the effective parallel conductance)
ρ	The density of total electric charge
σ_n	The capture cross-section of electrons
τ	The time constant
ε	The permittivity of the material
ε_r	The relative permittivity
ξ	The delay coefficient
ξ_{eq}	The value of the delay coefficient ξ at the absolute temperature T_{eq}
A	The cross-sectional area of the sample
a_+	The coefficient in the electric current density formula (Eq. 19)
a_-	The coefficient in the electric current density formula (Eq. 19)
A_{eff}	The effective cross-sectional area of the gas-sensing film
C_b	The capacitor of the converted electrical equivalent circuit (see Fig. 8b)
C_s	The series capacitance
C_{char}	The capacitor of the circuit branch corresponding to the charging and discharging the grain-boundary traps (see Fig. 7)
C_{dep}	The capacitance of the depletion regions of the grain-boundary region
D	The diffusion constant of electrons
E	The electric field
e'	The coefficient in the normalized rate equation (Eq. 30)
e''	The coefficient in the analytical solution of the rate equation (Eq. 33)
E_0^{max}	The maximum electric field in the grain-boundary region in the thermodynamical equilibrium
E_I^{max}	The maximum electric field in region I
E_{II}^{max}	The maximum electric field in region II
E_c	The bottom of the conduction band
E_F	The Fermi level
E_g	The band gap
E_I	The electric field in region I

E_T	The energy level of the electronic interface state (i.e. trap state) at the grain boundary
E_v	The top of the valence band
f_n^{eq}	The occupation probability of the trap states in the thermodynamical equilibrium at the absolute temperature T_{eq}
G_{sh}^{air}	The sheet conductance of the gas-sensing film in clean air
G_{sh}^{gas}	The sheet conductance of the gas-sensing film in the presence of the target gas
I	The electric current
I_{GB}^{DC}	The DC electric current flow through the grain boundary
I_0	The coefficient in the electric current formula (Eq. 46)
I_{air}	The electric current in the gas-sensing film in clean air
I_{DC}	The DC electric current
I_{gas}	The electric current in the gas-sensing film in the presence of the target gas
J	The density of the electric current
J_{GB}^{DC}	The DC electric current density in the grain-boundary region
J_{GB}^{tot}	The total current density in the grain-boundary region
J_0	The coefficient in the electric current density formulas (Eqs. 19, 21, and 23)
J_I	The density of electric current in region I
J_{DC}	The density of the electric DC current flow through the sample
J_{II}	The density of electric current in region II
k_0	The coefficient in the normalized rate equation (Eq. 30)
k_B	Boltzmann's constant
k_i	The forward rate constant for oxygen ionization
k_n	The capture coefficient of electrons
k_{-i}	The reverse rate constant for oxygen ionization
k_{-n}	The emission coefficient of electrons
L	The length of the sample
L_{GB}^{eq}	The length of the grain-boundary region in the thermodynamical equilibrium at T_{eq}
L_{GB}	The length of the grain-boundary region
L_{mod}	The inductor of the circuit branch corresponding to the modulation of the grain-boundary potential barrier (see Fig. 7)

m_n^*	The effective mass of electrons
m_0	The mass of a free electron
n	The density of electrons
N_B^{DC}	The density of the occupied electronic grain-boundary states in the steady state
n_B^{DC}	The density of electrons at the grain boundary in the steady state
N_{GB}^{eff}	The effective number of grain boundaries in the path of the electric current
N_B^{eq}	The density of the occupied electronic grain-boundary states in the thermodynamical equilibrium at T_{eq}
N_{O}^{tot}	The total density of the adsorbed oxygen
N_B^{tot}	The total density of the grain-boundary states
N_{O}	The density of the neutral adsorbed oxygen
N_a	The density of ionized acceptors
N_B	The density of the occupied grain-boundary states
n_B	The density of electrons at the grain boundary
N_d	The density of ionized donors
$N_{\mathrm{O}^-_{\mathrm{ads}}}$	The density of ionized oxygen adatoms
N_{BF}	The density of fixed electronic grain-boundary states
N_{GB}	The number of grain boundaries
p	The density of holes
q	The unit charge
Q_i	The total electric charge corresponding to the interface states.
Q_{sc}	The total net charge in the semiconductor (i.e. space charge)
[R]	The concentration of the reducing gas
R_b	The resistor of the converted electrical equivalent circuit (see Fig. 8b)
R_s	The series resistance
r_{BF}	The ratio of the density of the fixed and the total density of the non-fixed grain-boundary states, $r_{BF} = N_{BF}/N_B^{tot}$
R_{bulk}	The bulk resistance
R_{char}	The resistor of the circuit branch corresponding to the charging and discharging the grain-boundary traps (see Fig. 7)

R_{diff}	The resistor corresponding to the grain-boundary-potential-barrier-limited differential conductance (see Fig. 7)
R_{GB}	The resistance of the grain-boundary region
R_{mod}	The resistor of the circuit branch corresponding to the modulation of the grain-boundary potential barrier (see Fig. 7)
R_{par}	The resistor of the converted electrical equivalent circuit (see Fig. 8b)
S	The sensitivity of the gas sensor: the ratio of electric current in the presence of the target gas and in clear air
T	The absolute temperature
T_0	The absolute temperature before the step change
T_1	The absolute temperature after the step change
$t_{50\%}$	The 50% response time (the time taken for 50% of the overall response to occur)
$t_{90\%}$	The 90% response time (the time taken for 90% of the overall response to occur)
T_{eq}	The absolute temperature corresponding to the thermodynamical equilibrium case used in the normalization (see Section 2.2.1)
U	The voltage applied across the sample
U_{GB}^{DC}	The DC voltage applied across a single grain boundary
U_{DC}	The DC voltage applied across the sample
U_{GB0}	The voltage applied across the grain boundary before the step change
U_{GB1}	The voltage applied across the grain boundary after the step change
U_{GB}	The voltage applied across a single grain-boundary region
V	The potential for electrons, $V = -\phi$
V_B'	The coefficient in Eqs. 21 and 22
$V_{B_0}^{eq}$	The height of the grain-boundary potential barrier in the thermodynamical equilibrium at T_{eq}
$V_{B_0}^{max}$	The maximum of the GB potential barrier height V_{B_0}, which corresponds to the filled GB states
V_B	Grain-boundary potential barrier
V_{B_0}	The height of the GB potential barrier in the thermodynamical equilibrium
V_{B_I}	The effective grain-boundary potential barrier in region I
$V_{B_{II}}$	The effective grain-boundary potential barrier in region II

v_{Tn}	The thermal velocity of electrons
x_{d_1}	The depletion width in region I
x_{d_2}	The depletion width in region II
x_{L_1}	The length of the linear potential profile in region I (see Eq. 10)
x_{L_2}	The length of the linear potential profile in region II (see Eq. 10)
Y	Admittance
Y_{GB}	The admittance of the grain-boundary region
Z	Impedance

List of Figures

List of Tables

Introduction

Granular materials consist of grains which have various sizes, shapes, and crystal orientation. The grains are also called crystallites, and the granular materials polycrystalline. Granular semiconductors often have unusual electrical properties, which originate from electronic interface states at grain boundaries (GBs) within the material [1, 2]. The presence of either impurity atoms, defects, or adsorbed gases at grain boundaries gives rise to these electronic states [1–5].

Typically granular materials are wide-band gap semiconductors such as metal oxides (e.g. ZnO, TiO_2, SnO_2, $BaTiO_3$, and $SrTiO_3$) and compound semiconductors (e.g. SiC, CdS, CdSe, and PbS) [1, 2, 6–8]. Grain boundaries are also present in other common semiconducting materials such as Si, Ge, GaAs, and ternary compound semiconductors [1, 2, 6]. The electrically active GBs may either benefit or harm the operation of devices in which granular materials are utilized. Granular semiconductors, such as polycrystalline silicon (i.e. polysilicon), are widely used as a low-cost and versatile material in the microfabrication of devices and integrated circuits [1, 2]. In this kind of application the presence of the electrically active grain boundaries in the material is often deleterious. For example, in solar cells fabricated from polycrystalline materials the grain boundaries reduce the efficiency of the solar cells considerably [1]. Therefore, much effort is put in the passivation of the grain boundaries [1].

In granular semiconductors the transport of charge carriers across the grain boundaries depend exponentially on the height of the GB potential barrier at the grain boundary [1]. This results in nonlinear electric current–voltage (I–V) characteristics [1]. The height of the grain-boundary potential barrier, in turn, depends quadratically on the electric charge at the grain boundary, which originates from the electronic interface states at the grain boundary [1]. Very small changes in the grain-boundary charge result in large changes in the electric resistance due to its exponential dependence on the height of the GB potential barrier. This exponential amplification effect is exploited, e.g., in very sensitive sensor devices. The dynamics of the electrical effects in the granular materials cover a broad frequency range [1, Publications II, III, and VI]: the fastest effects are related to the bulk regions of the material, the slower effects to the ordinary GB conductance and capacitance, and the slowest ones to the electronic trapping at grain boundaries. These electronic trapping effects cause extraordinary features such as negative admittance and capacitance [1, Publications II and VI].

Several devices are directly based on the special electrical properties of GBs: Varis-

tors (i.e. variable resistors or voltage-dependent resistors (VDR)), positive temperature coefficient (PTC) resistors, grain-boundary capacitors, pressure gauges, light detectors, and gas sensors [1, 9].

The use of polycrystalline semiconductors in the varistor application is based on their nonlinear I–V characteristics [1, 9]. Metal oxides, for example ZnO, are usually employed because of their large-energy-handling capabilities [1, 9]. Applications of varistors range from power switching in electrical transmission systems to voltage surge protection in automotive and semiconductor electronics [9]. The operation principle of a varistor as a solid-state switch is simple: In the off-state the varistor is operated in the Ohmic (i.e. linear) part of the I–V curve, and only leakage current flows through the device. In the on-state the nonlinear part of the I–V curve, where the current is high, is employed.

Metal-oxide semiconductors are frequently used as gas sensors [7, 8, 10, 11]. A common gas sensor is a resistive sensor where the electrical resistance of the gas-sensitive material changes in the presence of target gas molecules. Usually the change in the electrical resistance is caused by a change in the density of ions adsorbed on the surfaces of the grains of the gas-sensing film. This is a very sensitive gas-sensing mechanism, since the electrical resistance depends exponentially on the GB potential barriers created by the adsorbed ions.

In the first half of the present thesis the electrical properties of granular n-type semiconductors having acceptor-type electronic interface states at the GBs are modelled. Over the past decades the electrical properties of granular semiconductors have been modelled extensively [1, 2, 6, 12]. The aim of the present thesis is to derive general and accurate analytical and numerical models, which are not too complicated and which allow rapid calculations. These kinds of models are needed in the electrical modelling of devices made of granular semiconductors. Of course, the models should also be able to predict correctly the behaviour of these devices. Fitting these models to experimental data is much simpler and faster than fitting a finite-element-method (FEM) model created using a numerical device simulator. In addition, analytical models give a far better insight into the underlying physical phenomena than all-numerical approaches. Numerical models often have no convergent solution either.

In the present thesis the DC, AC, and transient characteristics of granular semiconductors are modelled. The electrical transients induced by both voltage and temperature changes are calculated. The modelling is carried out at three different levels: (*i*) a simple fully analytical model, (*ii*) a semianalytical model, and (*iii*) numerical device simulation. The semianalytical model here refers to a more approximative model than those typically used in the numerical device simulations,

but which still requires numerical methods when solving the equations of the model. The fully analytical model is obtained by approximating further the semianalytical model. The results of the present models are compared with the results obtained using SILVACO® ATLAS™ device simulation software [13]. The advantage of this approach is that we can compare real intrinsic properties that are not affected by external parasitic effects as may be the case with experimental results. The semi-analytical model is also fitted to the experimental data obtained from the DC and transient measurements of ZnO powder samples [14].

In the present thesis the granular material is modelled with a geometrical model [2], where the material is represented by a number of identical grain boundaries separated by bulk regions. Numerous studies (see, for instance, Refs. [1, 2, 12] and references therein) have shown that this approach is general enough to explain most experimental results. The modelling is based on the drift-diffusion theory, which has not previously been employed in the modelling of granular semiconductors in such a broad scale as in the present thesis, even though the drift-diffusion theory is more appropriate in granular semiconductors utilized, e.g., in gas sensors [12].

The latter half of the present thesis discusses resistive metal-oxide based gas sensors. In a modern resistive gas sensor a metal-oxide gas-sensing film is deposited on a micromachined microhotplate structure [11, 15]. The microhotplate is needed for keeping the gas-sensing film at an elevated temperature (typically 200–400°C), which is necessary for sensor operation [11, 15]. In the present thesis tin dioxide (SnO_2) gas-sensing film deposited by atomic layer deposition (ALD) has been integrated for the first time on a microhotplate gas sensor. Due to the special demands of the ALD process, the fabrication process differs from the standard microhotplate process. The novel sensor is characterized and tested on chemical vapours representing common flammable and toxic materials: ethanol, acetone, and acrylonitrile.

In addition, in the present thesis the general model of granular semiconductor is extended to resistive metal-oxide gas sensors by describing the gas adsorption by the so-called surface state model. This model is employed in a quantitative explanation of the bias-voltage dependent sensitivity and negative-admittance effects, which were also observed experimentally in commercial gas sensors. As it will be shown, these effects originate from the intrinsic electrical properties of granular semiconductors.

The first half of the present thesis discusses the general modelling of granular semiconductors: the background of the modelling is presented in Section 1, the model employed in Section 2, and the modelling results in Section 3. The latter half of the present thesis, Section 4, discusses the resistive metal-oxide based gas sensors: the fabrication and characterization of the novel sensor is presented in Section 4.1, the

modelling of these kinds of sensors in Section 4.2, and the bias voltage dependent sensitivity and negative admittance effects in Sections 4.3 and 4.4, respectively. The notation differs slightly from publication to publication. In this thesis the notation has been unified. Thus, the formulas and parameter values may differ slightly from the individual publications.

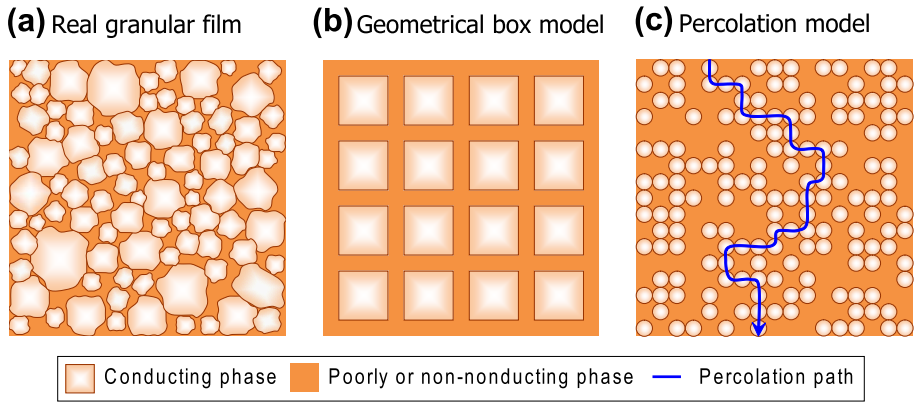

Figure 1: (a) Schematic picture of a real granular film. (b) Two-dimensional box model of a granular film. (c) Two-dimensional percolation model of a granular film at the percolation threshold. The percolation path is shown.

1 Introduction to modelling

1.1 Modelling granular material

Granular materials are usually very complex and their structures are far from ideal. An example of a real granular film is sketched in Fig. 1a. The grains consisting of conductive material are surrounded by material which is poorly or non-conductive, such as air or segregated atoms. The shape, and orientation of the grains may vary. In addition, the adjacent grains may be connected to each other with a small or large contact area [12], or they may not be connected at all.

Generally, a film consisting of grains can be modelled with an electric circuit consisting of electrical equivalent circuit (EEC) presentations of the grains and grain boundaries. Mathematically this approach is challenging. In order to calculate the electric current passing through the granular film the electric properties of each grain and grain-boundary must be known. In practice experimental determination of the each part of the film is, of course, impossible. Several approximative models exist for the calculation of the electric current passing through an inhomogeneous material: Geometrical models, and percolation and effective medium theories [2]. The largest difference between the models is that in the geometrical models the material is assumed to be highly ordered, and in the percolation and effective medium theories completely random [2]. In other words, they apply to fundamentally different prob-

lems. A large number of publications are available, where the percolation theory (see e.g. Refs. [2, 16–19]) and the effective medium theory (see e.g. Refs. [2, 17–22]) are presented.

In the geometrical models the material is represented by highly idealised structures. One of the simplests model is the cubic or box model, where the grains are presented by cubes in three dimensions (3D) or squares in two dimensions (2D) arranged in a square lattice (see Fig. 1b). The cubic model is sometimes called the brick layer model (BLM). The advantage of the geometrical models is that although the calculation of the electrical properties is fairly simple, they can yield reasonably realistic results. In addition, a number of electric properties of the geometrical models are insensitive to the precise geometry considered [2]: For example, if the layer separating the grains (i.e. the poorly conductive region in Fig. 1b) is thin, then the cubic model has exactly the same overall resistance as the corresponding geometrical model consisting of spheres [2]. The cubic model has been compared with a realistic model of polycrystals: When the grain-boundary resistance dominates, the overall resistance of the realistic 3D polycrystal is, according to numerical simulations, roughly 17 % lower than the overall resistance of the corresponding cubic model [23]. A similar small difference has also been observed in 2D [24]. As a summary, although it could seem unlikely, the cubic model is a fair approximation of a real polycrystalline material.

In the percolation and effective medium theories the volume fraction of the conductive and poorly or non-conductive phases in the material is considered. Mixing ratio is the ratio of the volume of one phase and the total volume. In the 2D case the area fraction is considered instead, and the mixing ratio is defined by the ratio of areas. Usually the percolation theories apply in the case of low mixing-ratio of the conductive phase. The effective medium theory, in turn, applies usually in the case of high mixing-ratio of the conductive phase. However, similar results can be obtained with both theories in the same mixing ratio range.

In the percolation theory the material is divided into regions. Each region belongs either to the conductive or to the non-conductive phase (see Fig. 1c). The percolation theory has two general approaches: the site and the bond model. The sites are points in space. Each site corresponds to a region in the material. These sites are connected to the neighbouring sites by bonds. In the site model the sites are either conductive or non-conductive in random, whereas in the bond model the bonds are random. An important property of material exhibiting percolation-type electrical conduction is the percolation threshold. The percolation threshold is the minimum volume or area fraction of the conductive phase, at which the electric current is able to flow through the material. The material at the percolation threshold and the percolation

path are illustrated in Fig. 1c. The percolation threshold of a bond-model of cubic lattice is 0.5 in 2D and 0.25 in 3D [17], respectively.

In the effective medium theory each grain of the material is treated as if it were surrounded by a homogeneous medium. The effective physical quantity of the whole material is determined self-consistently. Several approaches and effective medium approximations exist. In addition, many nonlinear models have been proposed (see, for instance, Refs. [25–28]).

In the present thesis mostly the properties of single grain-boundaries are studied. The whole granular material is modelled by a one-dimensional (1D) geometrical model structure, where identical grain-boundary regions are connected in series (see Section 2). This allows the total current flow through the whole material to be calculated in a simple manner. One might think that this assumption of the structure of the whole material is quite far from reality. However, the assumption made is that all the relevant grain boundaries in the material can be presented by a set of identical grain boundaries. In other words, the properties of the identical grain boundaries of the model project the properties of all grain-boundaries in the path of the current. Numerous studies (see, for example, Refs. [1, 2, 12] and references therein) have shown that this approach is sound and can explain most of the experimental results in common granular semiconductors.

1.2 Modelling granular semiconductors

Since the surface-to-volume ratio is high in granular semiconductors, the properties of the surfaces of the grains and interfaces between the grains of the material become highly important. In semiconductors, surfaces and interfaces often have a large effect on the electrical properties of the materials. Surfaces and interfaces by themselves perturb the periodicity of the semiconductor crystal. The perturbation can create local electronic states inside the energy band gap of the semiconductor [3, 4]. Real surfaces and interfaces often have surface impurities and defects [2–4]. The surface and interface states related to the material itself are called intrinsic states [2, 29]. In addition to intrinsic states, extrinsic states can be generated by adsorption of gases [2, 5, 29, 30]. (In contrast, Lüth [4] defines only the surface states related to ideal surfaces as intrinsic and the others as extrinsic surface states.)

The existence of the local electronic states gives rise to electronic trapping processes, which can be modelled in the similar way as the bulk trap states, which are discussed, for example, in Ref. [31]. In the case of trapping in an adsorbed atom or molecule (i.e. extrinsic state) the process is also known as ionization. In general, the type of

Table 1: Charging characters of electronic trap states [4].

Type of state	Occupied by electron (i.e. empty of holes)	Empty of electrons (i.e. occupied by hole)
Donor	Neutral (0)	Positive (+)
Acceptor	Negative (−)	Neutral (0)

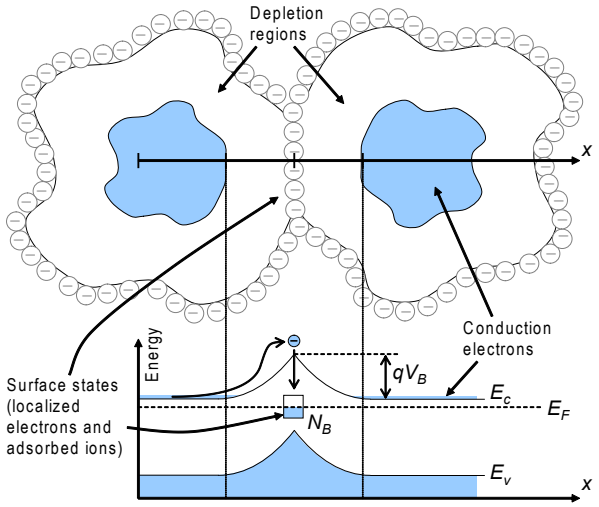

Figure 2: Schematic picture of two connected grains of an n-type semiconductor material. The electronic energy bands along the x-axis in the grain-boundary region are plotted, and trapping of a conduction electron in an acceptor-type electronic interface state is illustrated. N_B is the density of the occupied interface states, E_c the bottom of the conduction band, E_v the top of the valence band, E_F the Fermi level, q the unit charge, and V_B the grain-boundary potential barrier.

the electronic traps states is either donor or acceptor. Depending on the occupancy and type of the trap state the electric charge of the trap state is either positive (+), neutral (0), or negative (−). The possible combinations are listed in Table 1.

Two connected semiconductor grains and the electronic energy bands in the grain-boundary region are illustrated in Fig. 2, where the semiconductor is n-type and the electronic interface states at the grain boundary are acceptor-type. The trapping of an electron in the interface state shown in Fig. 2 gives rise to a local charge at the grain boundary (density N_B per area). This local charge, in turn, causes the bending of electronic energy bands, which is discussed below. The band bending is characterized by a grain-boundary potential barrier V_B, which determines the

transport of electrons across the grain boundary.

The thickness of the grain-boundary interface itself (i.e. the intergranular phase) in materials, where the electrical activity of grain boundaries is high, varies from less than a monolayer up to several monolayers [1, 6]. The typical thickness is 2–10 nm [1], but the diffusion of atoms can result in thicknesses of 100 nm or higher [1]. However, in typical cases the thickness of the grain-boundary interface is so small that it can be considered infinitely thin [1]. This approach is adopted in the present thesis. In some cases the size of the grains has much larger effect on the electronic properties of the granular semiconductor. If the depletion regions shown in Fig. 2 extend across the whole grains, the electronic properties change considerably [2]. This effect is discussed in more detail below.

There are also additional effects observed at grain boundaries: GB scattering of charge carriers [2, 32], tunnelling effects [1], minority charge carrier effects [1, 2], hot electron phenomena [1], and ion and atom movement and segregation [1, 2, 6, 33]. These effects are not considered further in the present thesis. However, the effects listed should be taken into account when the models presented in the present thesis are developed further.

1.2.1 Depletion, inversion, and accumulation regions

The depletion, inversion, and accumulation regions [3, 4] around a grain boundary are sketched in Fig. 3. Acceptor interface states in an n-type semiconductor give rise to depletion regions, where the density of charge carriers is very low, or even inversion regions, where minority charge carriers (i.e. holes in this case) are accumulated. Donor interface states result in an accumulation region, where major charge carriers (i.e. electrons in this case) are accumulated. In a p-type semiconductor the cases are the opposite: donor states result in depletion or inversion, and acceptor states in accumulation, respectively. Fig. 3 shows that in the inversion case the width of the region, where the density of minority charge carriers exceeds the density of majority charge carriers, is so small that, in fact, quantum effects [4] must be taken into account in inversion regions.

The total electric charge corresponding to the interface states is Q_i. This charge is screened (i.e. compensated) by the total net charge in the semiconductor, which is often called the total space charge Q_{sc}. The overall charge neutrality requires that

$$Q_i = -Q_{sc}. \tag{1}$$

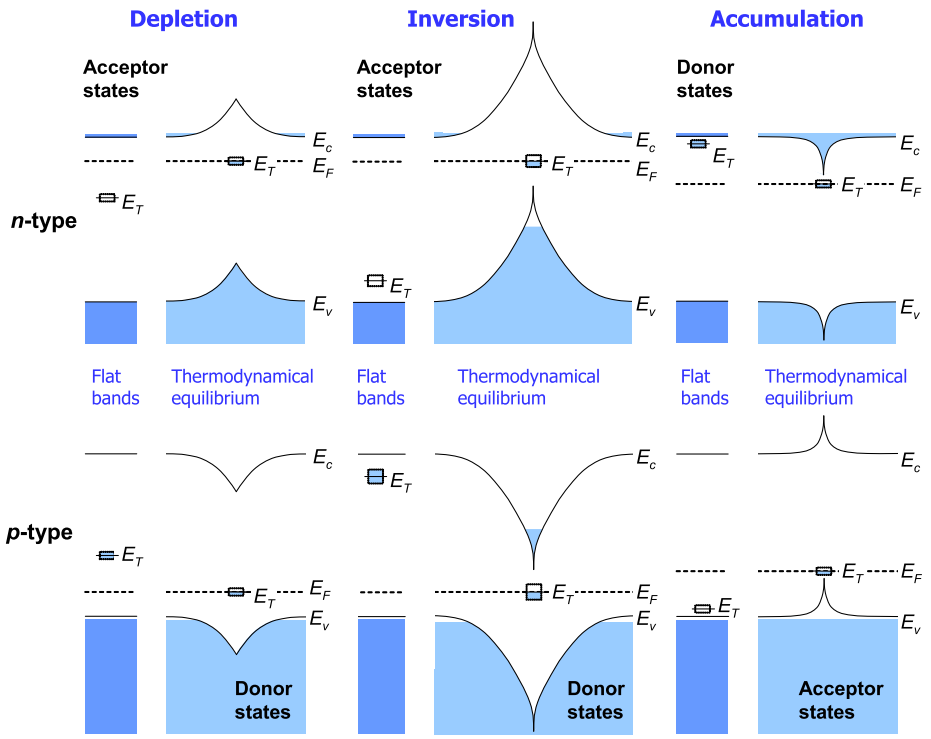

Figure 3: Illustration of energy bands around grain boundaries with depletion (*left*), inversion (*middle*), and accumulation (*right*) regions in n-type (*top*) and p-type semiconductors (*bottom*), respectively. The cases of flat-band and thermodynamical equilibrium are shown. E_c is the bottom of the conduction band, E_v the top of the valence band, E_F the Fermi level, and E_T the energy level of the electronic interface state (i.e. trap state) at the grain boundary. The type of the interface state (donor or acceptor) is indicated in each case. In the flat-band case the electronic interface states are neutral.

The grain size has a large effect on the electrical properties of a granular semiconductor. If the depletion regions (see Fig. 2) extend across the whole grains and no bulk regions lie in-between the two grain boundaries, then the charge neutrality condition (Eq. 1) must be applied in the whole material. This results in a very different kind of material, where the interface and surface states are acting as effective bulk donors and acceptors [2, 34, 35]. Decreasing the grain size below 10 nm gives rise to quantum effects as well [36].

In general, the electric potential ϕ in a semiconductor can be solved from Eq. 1 and Poisson's equation [4, 37]

$$\nabla^2 \phi = -\frac{\rho}{\varepsilon}, \tag{2}$$

where ε is the permittivity of the material and ρ the density of total electric charge, which is given by

$$\rho = q\left(p - N_a - n + N_d\right), \tag{3}$$

where q is the unit charge, p the density of holes, N_a the density of ionized acceptors, n the density of electrons, and N_d the density of ionized donors, which are all spatially dependent.

1.2.2 Theories for calculating charge transport

The two most common theories for calculating charge transport in semiconductors are the thermionic-emission and the drift-diffusion theories. The former theory applies usually to high-mobility and the latter to low-mobility semiconductors, respectively [38]. In addition, a third theory, the so-called thermionic-emission – diffusion theory, which is a mixture of the first two theories, has been synthesised [38]. In all of the theories it is assumed that the height of the GB potential barrier is much larger than $k_B T$, where k_B is Boltzmann's constant and T the absolute temperature, and the charge carriers on both sides of the grain boundary can be described by their thermal equilibrium distributions in spite of the current flow [38].

In all these theories the mean free path (MFP) of charge carriers must be less than the diameter of grains. Otherwise grain-boundary scattering of charge-carriers dominates [2, 12, 32, 39]. The applicability of the theory is evaluated by the MFP of the charge carriers: If the width of the GB region is equal to or less than the MFP of the charge carriers [12], then the thermionic-emission theory applies. In this case the charge carriers do not scatter in the GB region, hence for calculation of the current flow, it is enough to count only the charge carriers which have enough energy to surmount the GB potential barrier [38]. The drift-diffusion theory applies when the width of the GB region is much larger than the MFP of the charge carriers [12]. In this case the charge carriers experience many scattering events in the GB region, i.e. their motion is characterized by a diffusion process.

Regardless of these differences the two theories give similar results for granular semiconductors [12]. This kind of similarity is also present, e.g., in Schottky diodes [38]. In the present thesis the drift-diffusion theory is utilized.

2 Model of a granular n-type semiconductor

In this section the model of a granular n-type semiconductor employed in the present thesis is presented. Depending on the approximation used in the derivation, the model is either fully analytical or semianalytical. The use of numerical device simulation software in the modelling of a granular semiconductor is described in Section 2.5.

In the model, the effect of holes in the material is neglected. However, with minor modifications, the model presented in the present thesis can also be applied to a p-type semiconductor. The model can be employed as long as the hot-electron phenomena and minority carrier effects [1, 14] are low. These effects can arise if the electric field in the GB region is very high [1, 14]. In addition, minority carriers can be generated under illumination, if the energy of the photons is larger that the band gap of the semiconductor [31, 38].

The model is based on the drift-diffusion theory, which has the benefit that since the electron density at the GB can be determined, the electron trapping at the GBs can be described by a rate equation. For the modelling of varistors and gas sensors different rate equations must be used. In varistors the electronic interface states are intrinsic, whereas in gas sensors they are extrinsic (see Section 1.2). In the present thesis the modelling is performed in such a way that the rate equation is treated separately from the rest of the dynamic electrical model. This allows the rate equation to be replaced by an appropriate one without the need of revision of the rest of the model.

In the model, a granular semiconductor is described using a one-dimensional geometrical structure shown in Fig. 4. The sample with a length L has N_{GB} identical GBs connected in series. The GB regions have a length of L_{GB} and they are separated by bulk regions.

Whereas each GB region has the length L_{GB}, each GB itself (i.e. the interface) is infinitely thin and has acceptor-type electronic interface states with a single discrete energy level at E_T. The electronic bands in the GB region are shown in Fig. 5. The densities of the total and the occupied GB states are N_B^{tot} and N_B, respectively. The existence of the interface states gives rise to a band bending and the GB potential barrier [1, 2, 12] (see Fig. 5). In the thermodynamical equilibrium the height of the GB potential barrier is given by [25]

$$V_{B_0} = \frac{qN_B^2}{8\varepsilon N_d} + \frac{k_B T}{q}. \tag{4}$$

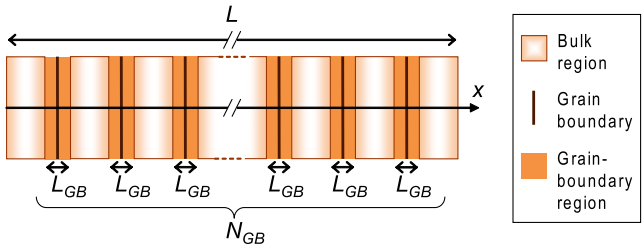

Figure 4: One-dimensional geometrical model structure of a granular semiconductor with N_{GB} identical grain boundaries. Electric current flows in the direction of the x axis.

The GB potential is discussed in more detail in Section 2.1.1.

The length of the GB region L_{GB}, which also is the total length of the depletion regions, can be calculated using the depletion region approximation (i.e. in Eq. 2 $\rho \approx qN_d$ in the depletion region). In contrast to this approximation, the edges of the depletion regions are not abrupt: the distribution tails of the majority charge carriers extend into the depletion region thereby reducing their length [38]. Therefore, L_{GB} is calculated with the formula [Publication I]

$$L_{GB} = \sqrt{\frac{8\varepsilon}{qN_d}\left(V_{B_0} - \frac{2k_BT}{q}\right)}. \tag{5}$$

When voltage U is applied across the sample shown in Fig. 4, the electric current I flow through the sample and the voltage U_{GB} across a single GB region are given by [Publication I]

$$I = \frac{U}{N_{GB}R_{GB} + R_s} \tag{6}$$

$$U_{GB} = \frac{U - R_sI}{N_{GB}}, \tag{7}$$

where $R_{GB} = U_{GB}/I_{GB}$ is the resistance of the GB region, I_{GB} is the electric current in the GB region, $R_s = (1 - N_{GB}L_{GB}/L)R_{bulk}$ is the series resistance due to the bulk regions, $R_{bulk} = L/(q\mu N_dA)$ is the bulk resistance, which is the resistance of a sample without any GBs (i.e. a sample consisting of bulk only), μ is the mobility of electrons, which is assumed to be constant, and A is the cross-sectional area of the sample. Often, A is defined as the effective cross-sectional area instead, since the geometrical shape of the granular material may differ from the ideal case [12].

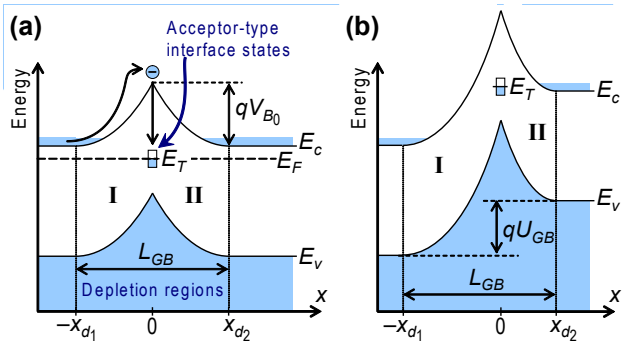

Figure 5: Electronic energy bands in the grain-boundary (GB) region of a n-type semiconductor (a) in the thermodynamical equilibrium and (b) when a voltage U_{GB} is applied across the GB region [Publication III]. Trapping of a conduction electron in acceptor-type interface states (energy level E_T) at the GB ($x = 0$) is illustrated in (a). E_c is the bottom of the conduction band, E_v the top of the valence band, and E_F the Fermi level. x_{d_1} and x_{d_2} are lengths of the depletion regions in the GB region. Regions I ($-x_{d_1} \leq x < 0$) and II ($0 < x \leq x_{d_2}$) are indicated.

2.1 Electric model of grain boundary

2.1.1 Potential in grain-boundary region

Instead of the electric potential ϕ, the potential for electrons $V = -\phi$ is utilized here. When the voltage U_{GB} is applied across the GB, the analytical solution of Poisson's equation obtained with the depletion region approximation [1, 12] can be written as [Publications I and V]

$$V(x) = \begin{cases} V_{B_I}\left(\frac{x}{x_{d_1}} + 1\right)^2 & \text{for } -x_{d_1} < x \leq 0 \text{ (region I)} \\ V_{B_{II}}\left(\frac{x}{x_{d_2}} - 1\right)^2 + U_{GB} & \text{for } 0 \leq x < x_{d_2} \text{ (region II)}, \end{cases} \tag{8}$$

where $V_{B_I} = V_{B_0}\left(1 + \frac{U_{GB}}{4V_{B_0}}\right)^2$ is the effective GB potential barrier in region I, $V_{B_{II}} = V_{B_0}\left(1 - \frac{U_{GB}}{4V_{B_0}}\right)^2$ the effective GB potential barrier in region II, $x_{d_1} = \frac{1}{2}\left(1 + \frac{U_{GB}}{4V_{B_0}}\right) \cdot \frac{N_B}{N_d}$ the depletion width in region I, and $x_{d_2} = \frac{1}{2}\left(1 - \frac{U_{GB}}{4V_{B_0}}\right)\frac{N_B}{N_d}$ the depletion width in region II. Because the depletion widths x_{d_1} and x_{d_2} must be positive, the voltage U_{GB} applied across the GB region must fulfill the condition [Publication V]

$$|U_{GB}| < 4V_{B_0}. \tag{9}$$

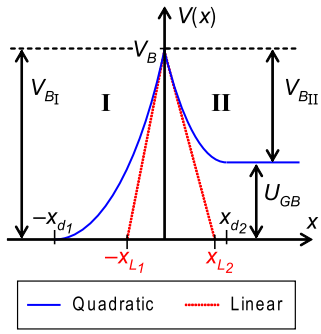

Figure 6: Electron potential V approximated by the quadratic and linear profiles in the grain-boundary region when voltage U_{GB} is applied across the GB [Publication I].

At high voltages ($U_{GB} \gtrsim 4V_{B_0}$) the depletion region approximation fails and the GB potential barrier vanishes. The quadratic potential profile is illustrated in Fig. 6.

The quadratic potential profile (Eq. 8) can be approximated by a linear profile (see Fig. 6) [Publications I and V]

$$V(x) = \begin{cases} V_{B_I} + E_I^{max} x & \text{for } -x_{L_1} < x < 0 \text{ (region I)} \\ V_{B_I} - E_{II}^{max} x & \text{for } 0 < x < x_{L_2} \text{ (region II)}, \end{cases} \tag{10}$$

where $E_I^{max} = E_0^{max}\left(1 + \frac{U_{GB}}{4V_{B_0}}\right)$ is the maximum electric field in region I, $E_{II}^{max} = E_0^{max}\left(1 - \frac{U_{GB}}{4V_{B_0}}\right)$ the maximum electric field in region II, $E_0^{max} = \frac{qN_B}{2\varepsilon}$, $x_{L_1} = V_{B_I}/E_I^{max}$, and $x_{L_2} = V_{B_{II}}/E_{II}^{max}$.

The shape of the potential in the GB region is discussed in more detail in Ref. [40], where numerical simulation results and a slightly more accurate quadratic potential profile with the bulk electric field taken into account in the solution of Poisson's equation are also presented.

2.1.2 Electric current and density of electrons at grain boundary

In the drift-diffusion theory, the electric current density of electrons in one dimension is given by

$$J = qD\frac{dn(x)}{dx} + q\mu n(x)E(x), \tag{11}$$

where D is the diffusion constant of electrons and E the electric field. In the present thesis it is assumed that there is no generation or recombination of charge carriers in the GB region. This simplifies the calculations considerably, because in this case the electron currents in regions I and II (see Fig. 5) are spatially independent.

The electric current densities J_I and J_{II} in regions I and II, respectively, are related by the continuity equation at the GB, which is given by

$$J_{II} - J_I = q\frac{dN_B}{dt}. \tag{12}$$

The electron density outside the depletion regions is equal to N_d and the potential difference across the GB region is U_{GB}. With these boundary conditions and Eq. 12, Eq. 11 can be solved in the GB region. The total current density in the GB region is given by [Publications II and III]

$$J_{GB}^{tot} = J_{GB}^{DC} - \frac{\mathcal{I}_{II}}{\mathcal{I}_{tot}} q\frac{dN_B}{dt} + \varepsilon\frac{dE_I}{dt}, \tag{13}$$

where the last term is the displacement current density, E_I is the electric field in region I, $\mathcal{I}_I = \int_{-x_{d_1}}^{0} \exp\left[qV(x)/(k_BT)\right] dx$, $\mathcal{I}_{II} = \int_{0}^{x_{d_2}} \exp\left[qV(x)/(k_BT)\right] dx$, $\mathcal{I}_{tot} = \mathcal{I}_I + \mathcal{I}_{II}$, and the DC electric current density in the GB region is given by [Publication V]

$$J_{GB}^{DC} = \frac{k_BT\mu N_d}{\mathcal{I}_{tot}} \left[\exp\left(\frac{qU_{GB}}{k_BT}\right) - 1\right]. \tag{14}$$

The density of electrons at the GB is given by [Publications II and III]

$$n_B = n_B^{DC} - \frac{q}{k_BT\mu}\frac{\mathcal{I}_I\mathcal{I}_{II}}{\mathcal{I}_{tot}} \exp\left(-\frac{qV_B}{k_BT}\right)\frac{dN_B}{dt}, \tag{15}$$

where the density of electrons at the GB in the steady state is given by [Publication V]

$$n_B^{DC} = \exp\left(-\frac{qV_B}{k_BT}\right)\left[N_d + \frac{J_{GB}^{DC}\mathcal{I}_I}{\mu k_BT}\right]. \tag{16}$$

Further analytical calculation requires use of approximations. The use of the linear potential profile (Eq. 10) yields [Publications II, III, and VI]

$$J_{GB}^{tot} = J_{GB}^{DC} - \frac{U_{GB}}{4V_{B_0}} q\frac{dN_B}{dt} + \frac{\varepsilon}{L_{GB}}\frac{dU_{GB}}{dt} \tag{17}$$

$$n_B = n_B^{DC} - \frac{\varepsilon}{q\mu N_B}\frac{dN_B}{dt}. \tag{18}$$

The total current (Eq. 17) consists of three terms: the GB potential-barrier limited current (J_{GB}^{DC}), the charging and discharging current, and the current related to the depletion region capacitance. The last term in Eq. 18 represents a delay effect which is caused by the fact that the electrons can enter and exit the GB only via the depletion regions, where they have a finite drift velocity.

The DC electric current density in the GB region and the density of electrons at the GB in the steady state can be calculated analytically using the approximative potential profiles. The quadratic potential profile (Eq. 8) and Eqs. 14 and 16 give [Publication I]

$$J_{GB}^{DC} = \frac{J_0\sqrt{\frac{8k_BT}{\pi q}}\sinh\frac{qU_{GB}}{2k_BT}}{\sqrt{1-\frac{k_BT}{qV_{B_0}}}\left[\exp\left(-\frac{qU_{GB}}{2k_BT}\right)\mathrm{erfi}(a_+)+\exp\left(\frac{qU_{GB}}{2k_BT}\right)\mathrm{erfi}(a_-)\right]} \tag{19}$$

$$n_B^{DC} = N_d\exp\left(-\frac{qV_{B_I}}{k_BT}\right)\frac{1+\frac{\mathrm{erfi}(a_-)}{\mathrm{erfi}(a_+)}}{\exp\left(-\frac{qU_{GB}}{k_BT}\right)+\frac{\mathrm{erfi}(a_-)}{\mathrm{erfi}(a_+)}}, \tag{20}$$

where the imaginary error function is defined by $\mathrm{erfi}(x) \equiv \mathrm{erf}(\mathrm{i}x)/\mathrm{i}$ [41], $\mathrm{i} = \sqrt{-1}$, $J_0 = \mu\sqrt{q^3N_d^3/\varepsilon}$, $a_+ = \sqrt{\frac{qV_{B_0}}{k_BT}}\left(1+\frac{U_{GB}}{4V_{B_0}}\right)$, and $a_- = \sqrt{\frac{qV_{B_0}}{k_BT}}\left(1-\frac{U_{GB}}{4V_{B_0}}\right)$. Analytical formulas for J_{GB}^{DC} and n_B^{DC} in the slightly more accurate case of the quadratic potential profile with bulk electric field taken into account are given in Ref. [40].

The linear potential profile (Eq. 10) and Eqs. 14 and 16 give [Publication I]

$$J_{GB}^{DC} = \frac{\sqrt{2}J_0\sqrt{V_{B_0}-\frac{k_BT}{q}}\left[1-\left(\frac{U_{GB}}{4V_{B_0}}\right)^2\right]\exp\left(-\frac{qV_B'}{k_BT}\right)\sinh\frac{qU_{GB}}{2k_BT}}{1-\exp\left(-\frac{qV_B'}{k_BT}\right)\left(\cosh\frac{qU_{GB}}{2k_BT}+\frac{U_{GB}}{4V_{B_0}}\sinh\frac{qU_{GB}}{2k_BT}\right)} \tag{21}$$

$$n_B^{DC} \approx \frac{N_d\exp\left(-\frac{qV_B'}{k_BT}\right)\left(\cosh\frac{qU_{GB}}{2k_BT}-\frac{U_{GB}}{4V_{B_0}}\sinh\frac{qU_{GB}}{2k_BT}\right)}{1-\exp\left(-\frac{qV_B'}{k_BT}\right)\left(\cosh\frac{qU_{GB}}{2k_BT}+\frac{U_{GB}}{4V_{B_0}}\sinh\frac{qU_{GB}}{2k_BT}\right)}, \tag{22}$$

where $V_B' = V_{B_0}\left[1+\left(\frac{U_{GB}}{4V_{B_0}}\right)^2\right]$. At low voltages Eqs. 21 and 22 reduce to [25, Publications I and V]

$$J_{GB}^{DC} \approx \sqrt{2}J_0\sqrt{V_{B_0}-\frac{k_BT}{q}}\exp\left(-\frac{qV_{B_0}}{k_BT}\right)\sinh\frac{qU_{GB}}{2k_BT} \tag{23}$$

$$n_B^{DC} \approx N_d\exp\left(-\frac{qV_{B_0}}{k_BT}\right)\cosh\frac{qU_{GB}}{2k_BT}. \tag{24}$$

2.2 Electronic trapping at grain boundary

If the holes are neglected, the rate equation for the electronic trapping can be written as [31, 42]

$$\frac{dN_B}{dt} = k_n n_B \left(N_B^{tot} - N_B\right) - k_{-n} N_c N_B, \tag{25}$$

where $k_n = \sigma_n v_{Tn}$ and $k_{-n} = k_n \exp\left[-(E_c - E_T)/(k_B T)\right]$ are the capture and emission coefficients of electrons, respectively, σ_n the capture cross-section of electrons, v_{Tn} the thermal velocity of electrons, E_c the bottom of the conduction band, and N_c the effective density of states in the conduction band. Eq. 25 is the standard trapping equation. In the case of metal-oxide gas sensors a modified rate equation must be used (see Section 4.2.1).

Substituting Eq. 18 in Eq. 25 gives the rate equation with the delay-correction [Publications II and III]:

$$\frac{dN_B}{dt} = \frac{k_n n_B^{DC} \left(N_B^{tot} - N_B\right) - k_{-n} N_c N_B}{1 + \xi \frac{N_B^{tot} - N_B}{N_B}}, \tag{26}$$

where $\xi = k_n \varepsilon/(q\mu)$ is the delay coefficient, which does not affect the trapping in the steady state. Often, the delay coefficient has such a small value ($\xi \ll 1$) that its effect on the rate equation can be neglected.

In the thermodynamical equilibrium at the absolute temperature T_{eq} the occupation probability of the trap states is given by the Fermi–Dirac distribution function [43]

$$f_n^{eq} = \frac{N_B^{eq}}{N_B^{tot}} = \frac{1}{1 + \exp\left[\frac{(E_T - E_F)_{V_B=0} + qV_{B_0}^{eq}}{k_B T_{eq}}\right]}, \tag{27}$$

where $(E_T - E_F)_{V_B=0}$ is the difference between the trap state energy level E_T and the Fermi level E_F in the flat-band case (i.e. without the GB potential barrier V_B) and N_B^{eq} is the density of the occupied electronic GB states and $V_{B_0}^{eq}$ the height of the GB potential barrier in the thermodynamical equilibrium at T_{eq}, respectively. Here the degeneracy of the trap states [3, 5] is neglected. Eq. 27 is solved numerically for N_B^{eq} because it depends on $V_{B_0}^{eq}$ by Eq. 4.

2.2.1 Normalization of the rate equation

Assuming that ε and N_d are constant, Eq. 4 allows us to relate $V_{B_0}^{eq}$ and V_{B_0} as [Publication III]

$$V_{B_0} = \nu^2 \left(V_{B_0}^{eq} - \frac{k_B T_{eq}}{q}\right) + \frac{k_B T}{q}, \tag{28}$$

where $\nu = N_B/N_B^{eq}$ is the normalized density of the occupied electronic GB states. The normalized variable ν also allows us to express the rate equation in a form which shows the dependence of the rate equation on externally controlled parameters T and U_{GB} explicitly. In addition, the normalization reduces the number of the parameter values needed in the calculations. Similarly, Eq. 5 can be normalized as [Publication III]

$$L_{GB} = L_{GB}^{eq}\sqrt{\frac{V_{B_0} - \frac{2k_BT}{q}}{V_{B_0}^{eq} - \frac{2k_BT_{eq}}{q}}}, \tag{29}$$

where L_{GB}^{eq} is the length of the GB region in the thermodynamical equilibrium at T_{eq}.

Using the relations $N_c/N_c^{eq} = (T/T_{eq})^{3/2}$ (the standard temperature dependence for a non-degenerate semiconductor [38]) and $k_n/k_n^{eq} = (T/T_{eq})^{1/2}$ (the standard temperature dependence of v_{Tn} [31] and a temperature-independent σ_n), the normalized rate equation with with the delay-correction can be written as [Publication III]

$$\frac{d\nu}{dt} = \frac{k_0\sqrt{\frac{T}{T_{eq}}}\left[\frac{n_B^{DC}}{n_B^{eq}}\left(\frac{1-f_n^{eq}\nu}{1-f_n^{eq}}\right) - \nu e'\left(\frac{T}{T_{eq}}\right)^{3/2}\right]}{1 + \xi_{eq}\sqrt{\frac{T}{T_{eq}}}\left(\frac{1-f_n^{eq}\nu}{f_n^{eq}\nu}\right)}, \tag{30}$$

where

$$k_0 = k_n^{eq}N_c^{eq}\exp\left(-\frac{E_c - E_T}{k_BT_{eq}}\right), \tag{31}$$

$e' = \exp\left[(E_c - E_T)(1/T_{eq} - 1/T)/k_B\right]$, and $\xi_{eq} = k_n^{eq}\varepsilon/(q\mu)$ is the delay coefficient at T_{eq}.

2.2.2 Solution of the rate equation

In the steady state the solution of Eq. 30 is given by [Publication I]

$$\nu_{DC} = \frac{N_B^{DC}}{N_B^{eq}} = \frac{\frac{n_B^{DC}}{n_B^{eq}}}{f_n^{eq}\frac{n_B^{DC}}{n_B^{eq}} + e'\left(1 - f_n^{eq}\right)\left(\frac{T}{T_{eq}}\right)^{3/2}}, \tag{32}$$

where N_B^{DC} is the density of the occupied electronic GB states in the steady state. A simple approximative analytical solution of Eq. 32 can be obtained by using Eq. 24 in Eq. 32 and linearizing the equation. This results in

$$\nu_{DC} \approx \frac{1 + 2e''\frac{T_{eq}}{T}\left(\frac{qV_{B_0}^{eq}}{k_BT_{eq}} - 1\right)}{f_n^{eq} + e''\left[1 + 2\,\frac{T_{eq}}{T}\left(\frac{qV_{B_0}^{eq}}{k_BT_{eq}} - 1\right)\right]}, \tag{33}$$

where $e'' = e'\left(1 - f_n^{eq}\right)\left(\frac{T}{T_{eq}}\right)^{3/2} / \cosh\frac{qU_{GB}}{2k_BT}$.

In the dynamical case the above equations can be solved only by using numerical techniques. However, using proper approximations the electrical response to a step change of temperature or voltage can be calculated analytically [Publication III]. After the step change in temperature (ΔT), voltage (ΔU_{GB}), or both occurring at $t = 0$, they are given by $T_1 = T_0 + \Delta T$ and $U_{GB1} = U_{GB0} + \Delta U_{GB}$, respectively. If the step changes are small, then the solution of Eq. 30 is given by [Publication III]

$$\nu(t) = \nu_0 + \Delta\nu\left[1 - \exp\left(-\frac{t}{\tau}\right)\right], \tag{34}$$

where ν_0 is the normalized density of the occupied GB states before the step change, $\Delta\nu$ the magnitude of change of ν, and τ the time constant. The formulas $\Delta\nu$ and τ are given in Publication III [Eqs. (38) and (39)].

The time constant τ describes the trap occupancy transient (Eq. 34). If $\Delta\nu$ is small, then the time constant of the total current (excluding the capacitive current) is also the same. Obviously, for very small transients the time constant τ is exactly the same as in the small-signal case (see Section 2.3 and Publication II [Eq. (20)]).

2.2.3 Additional fixed interface states at grain boundary

GBs often have additional electronic interface states which do not participate in the electronic trapping process due to their lower energy levels [1]. The filled electronic interface states below the Fermi level can be represented by fixed acceptor-type electronic interface states that are all occupied and have density N_{BF} [14]. In this case the GB potential barrier in the thermodynamical equilibrium is given by [Publication III]

$$V_{B_0} = \frac{q}{8\varepsilon N_d}\left(N_B + N_{BF}\right)^2 + \frac{k_BT}{q}. \tag{35}$$

Because of Eq. 35, a change must be made in the normalization presented above: Eq. 28 must be rewritten as [Publication III]

$$V_{B_0} = \left(\frac{\nu + r_{BF}/f_n^{eq}}{1 + r_{BF}/f_n^{eq}}\right)^2\left(V_{B_0}^{eq} - \frac{k_BT_{eq}}{q}\right) + \frac{k_BT}{q}, \tag{36}$$

where the ratio of the density of the fixed and the total density of the non-fixed GB states is given by $r_{BF} = N_{BF}/N_B^{tot}$.

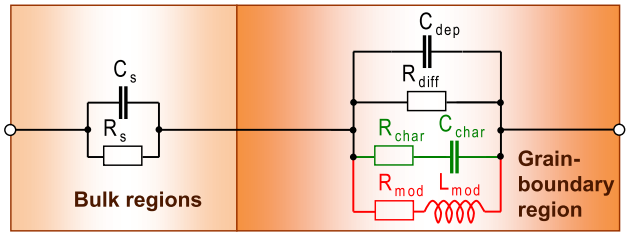

Figure 7: Small-signal electrical equivalent circuit (EEC) model of a granular n-type semiconductor with a single GB [Publication II]. R_s and C_s are the series resistance and capacitance, respectively, representing the bulk regions of the sample. C_{dep} is the capacitor corresponding to the depletion regions of the GB region and R_{diff} the resistor corresponding to the GB-potential-barrier-limited differential conductance. R_{char} and C_{char} are the resistor and the capacitor of the circuit branch corresponding to the charging and discharging the GB traps, respectively. R_{mod} and L_{mod} are the resistor and the inductor of the circuit branch corresponding to the modulation of the GB potential barrier, respectively.

2.3 Small-signal model of granular n-type semiconductor

A small-signal electrical equivalent circuit (EEC) model describes fully the electrical response of the modelled device to a small-signal AC. Usually, small-signal EEC models consist of linear and frequency-independent circuit elements. EEC models are especially useful in understanding the electrical properties of devices and representing experimental data. Fitting an EEC model to experimental data allows extraction of the values of the circuit elements of the EEC model. These values can be used for further study of the underlying physical phenomena.

A small-signal EEC model of the GB region can be derived by linearizing Eqs. 17 and 30 and writing the total current in the frequency space [Publications II and VI]. Because the electronic trapping at GBs changes the GB potential barrier, the term J_{GB}^{DC} in Eq. 17 is split into the ordinary GB potential-barrier-limited and barrier-modulation currents. The EEC model of a granular n-type semiconductor consisting of a single GB is shown in Fig. 7. The EEC consists of passive, linear, and frequency-independent circuit elements only. The values of the circuit elements depend on the DC bias voltage applied across the GB region. Analytical formulas for the values of the circuit elements of the EEC model are given in Publication II [Eqs. (14)–(19) and (21)].

In Fig. 7 $C_{dep} = \varepsilon A / L_{GB}$ is the capacitance of the depletion regions of the GB region

and $1/R_{diff}$ the GB-potential-barrier-limited differential conductance. The circuit branch R_{mod}–L_{mod} corresponds to the modulation of the GB potential barrier and the circuit branch R_{char}–C_{char} to the charging and discharging the GB traps. Although these circuit branches describe fully the electrical behaviour of the modulation and charging effects, the resistor R_{mod}, the inductor L_{mod}, the resistor R_{char}, and the capacitor C_{char} do not have a clear physical or electrical meaning as such. However, the time constant τ of these circuit branches corresponds to the time constant of the electronic trapping at the grain boundary. It is the same for both of the circuit branches: $\tau = L_{mod}/R_{mod} = R_{char}C_{char}$.

The circuit branch R_{mod}–L_{mod} originates from the modulation of the occupancy of the GB states and thereby the GB potential barrier. It is caused by the fact that the applied voltage signal modulates the electron density at the GB, which controls the electron trapping process: The increase of the voltage rises the GB electron density, which causes the increase of the GB trap occupancy and the GB potential barrier, which, in turn, decreases the electric current flow through the GB. This effect is explained in more detail in Section 3.3.2.

The circuit branch R_{char}–C_{char} represents the electric current corresponding to the charging and discharging of the electronic GB traps. It has exactly the same RC form as the EEC representations of electronic trapping [1, 9, 38]. However, unlike in the usual cases the values of the circuit elements R_{char} and C_{char} are negative (see Section 3.2). The values of the circuit elements in the GB potential barrier modulation circuit branch R_{mod}–L_{mod} are also negative. These negative values can be explained as follows: Both the modulation of the GB potential barrier and the charging effects reduce the current flow through the GB region when the voltage is increased. The charging current reduces the overall current because the electrons trapped in the GB states are not able to contribute to the overall current passing through the GB region. When the voltage is decreased, the GB-potential-barrier modulation and discharging effects increase the current. Therefore, the overall effect is that the direction of the current flow in the circuit branches R_{char}–C_{char} and R_{mod}–L_{mod} is opposite to that in the resistor R_{diff}. Thus, the circuit elements in these circuit branches must have negative values. Negative admittance and negative capacitance effects are further discussed in Section 4.4.

The low-frequency circuit elements (i.e. without the depletion capacitance C_{dep}) of the EEC model of the GB region (see Figs. 7 and 8a) can be converted into a circuit

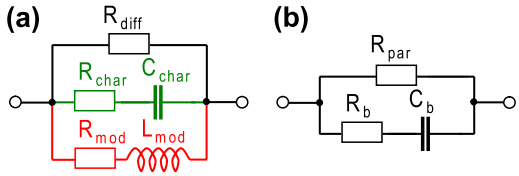

Figure 8: (a) The small-signal EEC model of the low-frequency circuit elements (i.e. without C_{dep}) in the grain-boundary region and (b) the converted circuit [Publication VI].

shown in 8b. The values of the circuit elements are given by [Publication VI]

$$\begin{aligned} R_{par} &= \frac{R_{diff}R_{mod}}{R_{diff}+R_{mod}} \\ R_b &= \frac{R_{mod}R_{char}}{R_{mod}-R_{char}} \\ C_b &= C_{char}\left(1-\frac{R_{char}}{R_{mod}}\right). \end{aligned} \tag{37}$$

The time constant of the R_b–C_b circuit branch is the same as in the modulation and charging circuit branches: $\tau = R_bC_b = L_{mod}/R_{mod} = R_{char}C_{char}$.

The impedance of a granular semiconductor represented by the EEC shown in Fig. 7 is given by [Publication II]

$$Z = \frac{N_{GB}}{Y_{GB}} + \frac{1}{\frac{1}{R_s}+\mathrm{i}\omega C_s}, \tag{38}$$

where ω is the angular frequency and $C_s = \varepsilon A/(L - N_{GB}L_{GB})$ is the series capacitance, and the admittance of the GB region is given by

$$Y_{GB} = \frac{1}{R_{diff}} + \mathrm{i}\omega C_{dep} + \frac{1}{R_{char}+\frac{1}{\mathrm{i}\omega C_{char}}} + \frac{1}{R_{mod}+\mathrm{i}\omega L_{mod}}. \tag{39}$$

2.4 Summary of the model formulas

Here the key formulas of the models are summarized. These formulas are used in the calculations, which are discussed in Section 3.

- Analytical and semianalytical models
  - The length of the GB region

$$L_{GB} = L_{GB}^{eq}\sqrt{\frac{V_{B_0} - \frac{2k_BT}{q}}{V_{B_0}^{eq} - \frac{2k_BT_{eq}}{q}}} \tag{29}$$

  - GB traps with a single energy level

$$V_{B_0} = \nu^2\left(V_{B_0}^{eq} - \frac{k_BT_{eq}}{q}\right) + \frac{k_BT}{q} \tag{28}$$

  - GB traps with a single energy level and additional fixed GB states

$$V_{B_0} = \left(\frac{\nu + r_{BF}/f_n^{eq}}{1 + r_{BF}/f_n^{eq}}\right)^2\left(V_{B_0}^{eq} - \frac{k_BT_{eq}}{q}\right) + \frac{k_BT}{q} \tag{36}$$

  - The total current density

$$J_{GB}^{tot} = J_{GB}^{DC} - \frac{U_{GB}}{4V_{B_0}}q\frac{dN_B}{dt} + \frac{\varepsilon}{L_{GB}}\frac{dU_{GB}}{dt} \tag{17}$$

- The analytical model
  - DC (requires the solution in the thermodynamical equilibrium, which in the present thesis is obtained using the semianalytical model)

$$\nu_{DC} \approx \frac{1 + 2e''\frac{T_{eq}}{T}\left(\frac{qV_{B_0}^{eq}}{k_BT_{eq}} - 1\right)}{f_n^{eq} + e''\left[1 + 2\,\frac{T_{eq}}{T}\left(\frac{qV_{B_0}^{eq}}{k_BT_{eq}} - 1\right)\right]}, \tag{33}$$

    * The simple approximative formulas

$$J_{GB}^{DC} \approx \sqrt{2}J_0\sqrt{V_{B_0} - \frac{k_BT}{q}}\exp\left(-\frac{qV_{B_0}}{k_BT}\right)\sinh\frac{qU_{GB}}{2k_BT} \tag{23}$$

$$n_B^{DC} \approx N_d\exp\left(-\frac{qV_{B_0}}{k_BT}\right)\cosh\frac{qU_{GB}}{2k_BT} \tag{24}$$

  - AC (requires the DC solution, which in the present thesis is obtained using the semianalytical model with the simple approximative formulas)

$$Z = \frac{N_{GB}}{Y_{GB}} + \frac{1}{\frac{1}{R_s} + \mathrm{i}\omega C_s} \tag{38}$$

$$Y_{GB} = \frac{1}{R_{diff}} + \mathrm{i}\omega C_{dep} + \frac{1}{R_{char} + \frac{1}{\mathrm{i}\omega C_{char}}} + \frac{1}{R_{mod} + \mathrm{i}\omega L_{mod}} \tag{39}$$

– Transient (requires the DC solution, which in the present thesis is obtained using the semianalytical model with the linear potential profile formulas)

$$\nu(t) = \nu_0 + \Delta\nu \left[1 - \exp\left(-\frac{t}{\tau}\right)\right] \tag{34}$$

- The semianalytical model
  - Thermodynamical equilibrium at T_{eq}

$$f_n^{eq} = \frac{1}{1 + \exp\left[\frac{(E_T - E_F)_{V_B=0} + qV_{B_0}^{eq}}{k_B T_{eq}}\right]} \tag{27}$$

$$L_{GB}^{eq} = \sqrt{\frac{8\varepsilon}{qN_d}\left(V_{B_0}^{eq} - \frac{2k_B T_{eq}}{q}\right)} \tag{5}$$

    * GB traps with a single energy level

$$V_{B_0}^{eq} = \frac{q\left(N_B^{eq}\right)^2}{8\varepsilon N_d} + \frac{k_B T_{eq}}{q} \tag{4}$$

    * GB traps with a single energy level and additional fixed GB states

$$V_{B_0}^{eq} = \frac{q}{8\varepsilon N_d}\left(N_B^{eq} + N_{BF}\right)^2 + \frac{k_B T_{eq}}{q} \tag{35}$$

  – DC (requires the solution in the thermodynamical equilibrium)

$$\nu_{DC} = \frac{\frac{n_B^{DC}}{n_B^{eq}}}{f_n^{eq}\frac{n_B^{DC}}{n_B^{eq}} + e'\left(1 - f_n^{eq}\right)\left(\frac{T}{T_{eq}}\right)^{3/2}} \tag{32}$$

$$I = \frac{U}{N_{GB}R_{GB} + R_s} \tag{6}$$

$$U_{GB} = \frac{U - R_s I}{N_{GB}} \tag{7}$$

    * The quadratic potential profile formulas

$$J_{GB}^{DC} = \frac{J_0\sqrt{\frac{8k_B T}{\pi q}}\sinh\frac{qU_{GB}}{2k_B T}}{\sqrt{1 - \frac{k_B T}{qV_{B_0}}}\left[\exp\left(-\frac{qU_{GB}}{2k_B T}\right)\mathrm{erfi}(a_+) + \exp\left(\frac{qU_{GB}}{2k_B T}\right)\mathrm{erfi}(a_-)\right]} \tag{19}$$

$$n_B^{DC} = N_d \exp\left(-\frac{qV_{B_I}}{k_B T}\right)\frac{1 + \frac{\mathrm{erfi}(a_-)}{\mathrm{erfi}(a_+)}}{\exp\left(-\frac{qU_{GB}}{k_B T}\right) + \frac{\mathrm{erfi}(a_-)}{\mathrm{erfi}(a_+)}} \tag{20}$$

* The linear potential profile formulas

$$J_{GB}^{DC} = \frac{\sqrt{2}J_0\sqrt{V_{B_0} - \frac{k_BT}{q}}\left[1 - \left(\frac{U_{GB}}{4V_{B_0}}\right)^2\right]\exp\left(-\frac{qV_B'}{k_BT}\right)\sinh\frac{qU_{GB}}{2k_BT}}{1 - \exp\left(-\frac{qV_B'}{k_BT}\right)\left(\cosh\frac{qU_{GB}}{2k_BT} + \frac{U_{GB}}{4V_{B_0}}\sinh\frac{qU_{GB}}{2k_BT}\right)} \quad (21)$$

$$n_B^{DC} \approx \frac{N_d\exp\left(-\frac{qV_B'}{k_BT}\right)\left(\cosh\frac{qU_{GB}}{2k_BT} - \frac{U_{GB}}{4V_{B_0}}\sinh\frac{qU_{GB}}{2k_BT}\right)}{1 - \exp\left(-\frac{qV_B'}{k_BT}\right)\left(\cosh\frac{qU_{GB}}{2k_BT} + \frac{U_{GB}}{4V_{B_0}}\sinh\frac{qU_{GB}}{2k_BT}\right)} \quad (22)$$

* The simple approximative formulas

$$J_{GB}^{DC} \approx \sqrt{2}J_0\sqrt{V_{B_0} - \frac{k_BT}{q}}\exp\left(-\frac{qV_{B_0}}{k_BT}\right)\sinh\frac{qU_{GB}}{2k_BT} \quad (23)$$

$$n_B^{DC} \approx N_d\exp\left(-\frac{qV_{B_0}}{k_BT}\right)\cosh\frac{qU_{GB}}{2k_BT} \quad (24)$$

– Transient (requires the DC solution)

$$\frac{d\nu}{dt} = \frac{k_0\sqrt{\frac{T}{T_{eq}}}\left[\frac{n_B^{DC}}{n_B^{eq}}\left(\frac{1-f_n^{eq}\nu}{1-f_n^{eq}}\right) - \nu e'\left(\frac{T}{T_{eq}}\right)^{3/2}\right]}{1 + \xi_{eq}\sqrt{\frac{T}{T_{eq}}}\left(\frac{1-f_n^{eq}\nu}{f_n^{eq}\nu}\right)} \quad (30)$$

* The linear potential profile formulas

$$J_{GB}^{DC} = \frac{\sqrt{2}J_0\sqrt{V_{B_0} - \frac{k_BT}{q}}\left[1 - \left(\frac{U_{GB}}{4V_{B_0}}\right)^2\right]\exp\left(-\frac{qV_B'}{k_BT}\right)\sinh\frac{qU_{GB}}{2k_BT}}{1 - \exp\left(-\frac{qV_B'}{k_BT}\right)\left(\cosh\frac{qU_{GB}}{2k_BT} + \frac{U_{GB}}{4V_{B_0}}\sinh\frac{qU_{GB}}{2k_BT}\right)} \quad (21)$$

$$n_B^{DC} \approx \frac{N_d\exp\left(-\frac{qV_B'}{k_BT}\right)\left(\cosh\frac{qU_{GB}}{2k_BT} - \frac{U_{GB}}{4V_{B_0}}\sinh\frac{qU_{GB}}{2k_BT}\right)}{1 - \exp\left(-\frac{qV_B'}{k_BT}\right)\left(\cosh\frac{qU_{GB}}{2k_BT} + \frac{U_{GB}}{4V_{B_0}}\sinh\frac{qU_{GB}}{2k_BT}\right)} \quad (22)$$

2.5 Modelling using numerical device simulation software

In addition to the semianalytical and analytical models presented above the SILVACO® ATLAS™ device simulation software [13] is used for calculating the electric properties of granular semiconductors. ATLAS is a FEM-based numerical device simulator, which can be used for calculating the electrical, optical, and thermal behaviour of semiconductor structures and devices in two and three dimensions. It is widely used in semiconductor research. In ATLAS the structure to be modelled is presented by a grid, where each node represents a point in the structure. Due

to the fact that the number of nodes is finite the grid is always an approximation of the structure. After the grid is formed the electric behaviour is calculated using discretized differential equations. The FEM-based modelling demands more central-processing-unit (CPU) time and memory than, for example, the numerical solution of a set of analytical formulas.

In ATLAS the 1D model structure shown in Fig. 4 is represented by a 2D structure, which is only two nodes wide. The electronic interface states are created at the grain boundary with the INTRAP statement, and the Blaze™ module [13] of ATLAS is used in the calculation.

3 Modelling results

In this section the results obtained using the semianalytical and analytical models presented in Section 2 are compared with the results obtained with the SILVACO ATLAS device simulation software. In addition, the semianalytical model is fitted to experimental DC and transient data reported in Ref. [14].

In order to decrease the calculation time and make a good use of the limited number of nodes, the numerical device simulations with ATLAS, the 1D structure shown in Fig. 4, which consists only of a single GB ($N_{GB} = 1$), was chosen for the calculations. In ATLAS the spacing between the nodes in the x direction varies gradually from $1–5 \cdot 10^{-3}$ nm at the GB to 10 nm on the edges of the structure [Publications I–III].

In the calculations [Publications I–III] the typical parameters of wide band-gap semiconductors were used [44]. The values of the parameters used in the calculations are listed in Table 2. These values are similar to those typically observed in granular wide band-gap semiconductors [1, 7, 12, 45, 46]. The values of the additional parameters needed in the ATLAS simulations are reported in Ref. [40].

The set of the formulas (see Section 2.4) of the semianalytical model was solved numerically with MATLAB® [47] using the MATLAB functions *erfz* [48], *fsolve*, and *ode45* [Publications I–III]. In the thermodynamical equilibrium the solution was obtained using Eqs. 4, 5, and 27. A flowchart describing the solution of the thermodynamical equilibrium case is shown in Fig. 9. The DC case was solved using the thermodynamical equilibrium solution and Eqs. 6, 7, 28, 29, 32, and either the formulas of the quadratic (Eqs. 19 and 20) or the linear potential profiles (Eqs. 21 and

Table 2: The values of the parameters used in the DC, AC, and transient calculations [Publications I–III].

Parameter	DC	AC	Transient
Band gap[†] E_g (eV)	3.0	3.0	3.0
The relative permittivity ε_r	9	9	9
Effective mass of electrons m_n^*	$0.3m_0$[‡]	$0.3m_0$[‡]	$0.3m_0$[‡]
Length of sample L (μm)	10	10	1.8
Bulk donor density N_d (cm^{-3})	10^{15}	10^{15}	10^{17}
Electron mobility μ (cm^2/(Vs))	1000	1000	1000
Acceptor-type interface states (electron traps)			
Total density N_B^{tot} (cm^{-2})	$1.4 \cdot 10^{11}$	$1.4 \cdot 10^{11}$	$2.2 \cdot 10^{12}$
Energy level $E_c - E_T$ (eV)	0.60 and 2.00	0.60	0.80

[†]Temperature independent.

[‡]m_0 is the mass of a free electron.

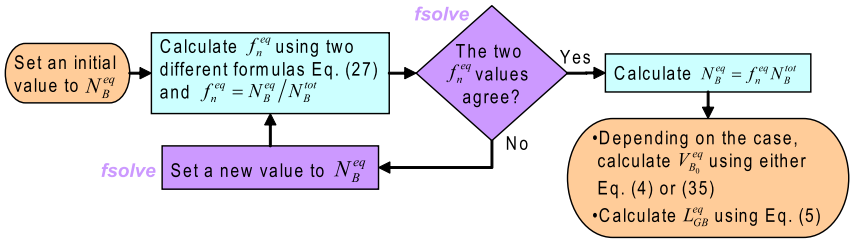

Figure 9: Flowchart describing the numerical solution of the thermodynamical equilibrium case. The steps where the MATLAB function *fsolve* is utilized are indicated.

22), or the simple approximative formulas (Eqs. 23 and 24). A flowchart describing the solution of the DC case is shown in Fig. 10. In addition to the numerical DC solution, an analytical solution was calculated using the thermodynamical solution and Eqs. 23, 24, and 33. The small-signal (i.e. AC) case was calculated using the DC solution obtained using Eqs. 23 and 24, Eqs. 38 and 39, and the formulas in Publication II [Eqs. (14)–(19)]. The transient case was calculated by solving Eq. 30 numerically with the initial condition from the DC case. Because the DC results (see Section 3.1 below) showed that the formula of the linear potential profile for J_{GB}^{DC} (Eq. 21) is accurate, it was used in the transient calculations together with Eq. 17. The number of parameters needed in the calculations can be reduced using the normalized formula given in Ref. [40] [Eq. (3.114)].

3.1 DC characteristics of granular semiconductors

The electric DC current density J_{DC} and the normalized electron density at the GB n_B^{DC}/N_d as functions of DC voltage U_{DC} applied across the sample with two different values of the trap energy level E_T are plotted in Fig. 11. In the case $E_c - E_T = 0.6$ eV the electronic trapping at GBs is present and, when the voltage U_{DC} is increased, the GB potential barrier increases from its thermodynamical-equilibrium value $V_{B_0}^{eq} = 0.348$ V to the maximum value of $V_{B_0}^{max} = 0.52$ V, which corresponds to the filled GB states. In the case $E_c - E_T = 2$ eV all the traps are filled and the height of the GB potential barrier is constant, $V_{B_0} = 0.52$ V.

Fig. 11 shows that the electronic trapping at the GBs changes remarkably the DC characteristics of the sample. Based on the shapes of the I–V curves, the I–V curves can be divided into four characteristic regions: linear, sublinear (only with trapping), superlinear, and series resistance limited (linear). In the literature the characteristic

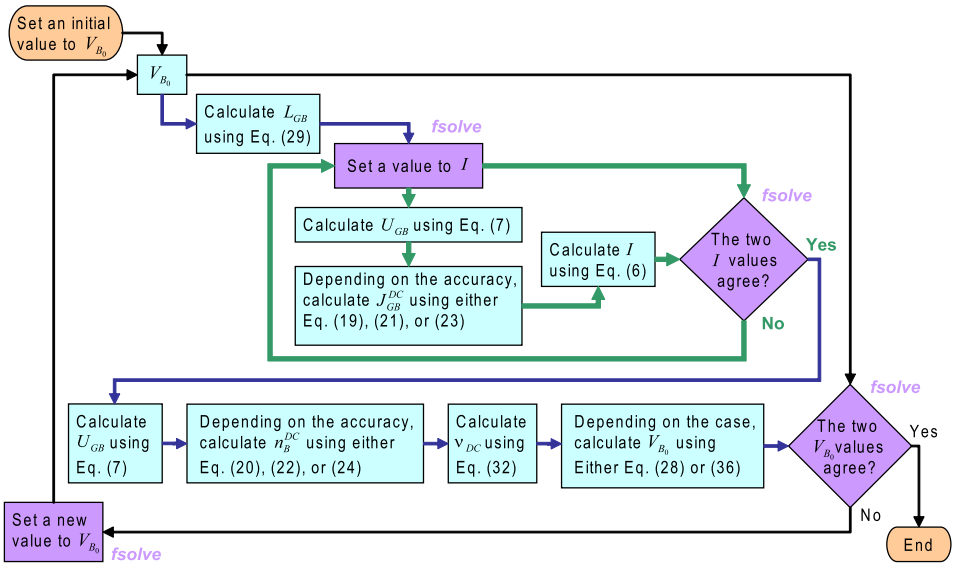

Figure 10: Flowchart describing the numerical solution of the DC case. The steps where the MATLAB function *fsolve* is utilized are indicated.

regions of the I–V curves are referred to differently than in Publications I, III and V: The linear region is called the Ohmic region [1, 6, 9, 49], the sublinear the sub-Ohmic [1, 49] or resistive [6], the superlinear the breakdown [1, 6, 49], and the series resistance limited the second Ohmic region [1, 49], respectively. On the contrary, in Ref. [9] the sublinear region is named as the breakdown and the superlinear region as the post-breakdown region, respectively.

The electric current density in each region of the I–V curve can be described by $J_{DC} \propto U_{DC}^{\alpha_J}$, where α_J is the exponent of the I–V curve. At low voltages current is limited by the GB potential barrier and increases linearly ($\alpha_J = 1$). In the trapping case ($E_c - E_T = 0.6$ eV) a sublinear region follows: The current increases with voltage slower than in the linear region ($\alpha_J < 1$), meaning that the resistance (U_{DC}/J_{DC}) increases with voltage. This is caused by filling of the traps at the GB (see inset in Fig. 11), which in turn increases the GB potential barrier (see Eq. 4) thereby limiting the flow of current. The enhanced electron trapping is caused by the increase in the electron density at the GB n_B^{DC} with the increasing voltage (see Eqs. 19, 22, 24, and 32). However, as the trapping proceeds, the growth of the GB potential barrier hinders the trapping process by decreasing n_B^{DC}.

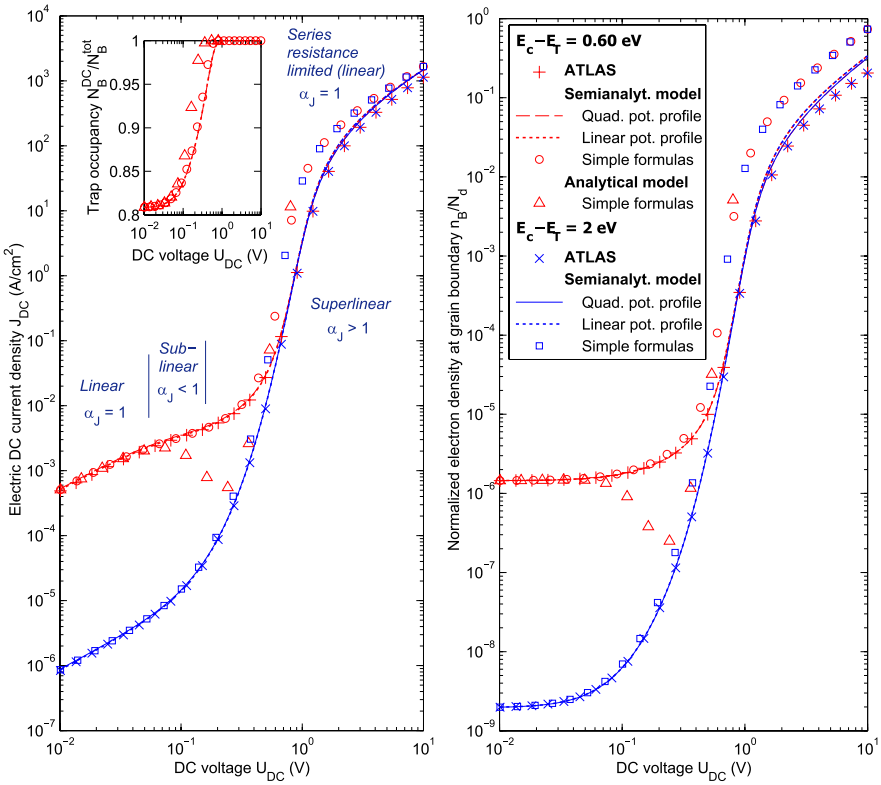

Figure 11: Electric DC current density J_{DC} (*left*) and normalized DC electron density at the GB n_B^{DC}/N_d (*right*) plotted against the DC voltage U_{DC} applied across the sample with different values of the trap energy level E_T [Publication I]. The steady-state trap occupancy N_B^{DC}/N_B^{tot} (*inset*) is shown in the case $E_c - E_T = 0.6$ eV. Calculated using ATLAS, the semianalytical model employing different formulas for J_{GB}^{DC} and n_B^{DC} (see text), and the analytical model (Eqs. 23, 24, and 33) with the parameter values listed in Table 2 at 300 K. The $E_c - E_T = 0.6$ eV and $E_c - E_T = 2$ eV curves unite at high voltages ($U_{DC} > 1$ V).

At higher voltages ($U_{DC} \approx 0.15$ V) the sublinear region ($\alpha_J < 1$) changes into a superlinear region, where the effective GB potential barrier decreases with increasing voltage (see Eq. 8) and the current increases steeply with voltage ($\alpha_J > 1$). In the series-resistance limited region, which lies at the high voltages ($U_{DC} > 1$ V), the resistance of the bulk regions limits the flow of current and the I–V curves return to linear ($\alpha_J = 1$).

The agreement between the semianalytical and ATLAS results is excellent in Fig. 11. A comparison of different formulas for J_{GB}^{DC} and n_B^{DC} used in the calculation is also shown in Fig. 11. The quadratic (Eqs. 19 and 20) and the linear potential profiles (Eqs. 21 and 22) give almost identical results. This is due to the fact that the most contribution in the integral in Eq. 14 comes from the top of the GB potential barrier, which is the same in both profiles. At high voltages ($U_{DC} \gtrsim 1.5$ V) the semianalytical models overestimate J_{DC} and n_B^{DC}. This is caused by the failure of the depletion region approximation, which was also observed in the ATLAS simulations. By taking the electric field in the bulk regions of the material into account when deriving formulas for J_{DC} and n_B^{DC} (see Sections 2.1.1 and 2.1.2 and Ref. [40]), the overestimation can be reduced. At low voltages ($U_{DC} \lesssim 0.3$ V, i.e. less than 60% of $V_{B_0}^{max}$) the simple formulas (Eqs. 23 and 24) are accurate enough to be used in the calculations.

The DC characteristics in the case $E_c - E_T = 0.6$ eV calculated by using the analytical model (Eqs. 23, 24, and 33) is plotted between 10^{-2} and 0.8 V in Fig. 11. The analytical model does not take the series resistance of the bulk regions into account. It works only at very low voltages up to the beginning of the sublinear region ($U_{DC} \lesssim 0.08$ V, i.e. less than 20% of $V_{B_0}^{max}$). Although the analytical model exaggerates the trapping in the sublinear region (see Fig. 11) due to the linearization approximation made in the derivation, it still describes correctly the overall shape of the I–V curve up to the superlinear region.

3.2 Small-signal characteristics of granular semiconductors

Since the values of the circuit elements of the small-signal EEC model (see Fig. 7) depend on the DC bias voltage U_{GB}^{DC} applied across the single GB region, the DC case was solved first. The density of the occupied GB states N_B as a function of U_{GB}^{DC} is plotted in Fig. 12a. As before, N_B increases with U_{GB}^{DC} due to the filling of the traps. This has an effect on the values of the circuit elements, since they depend on N_B.

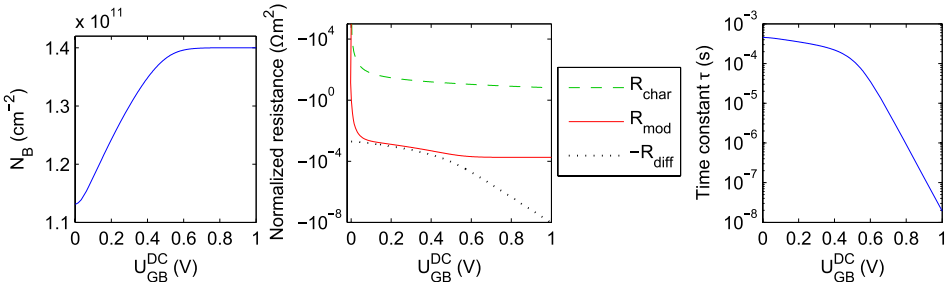

Figure 12: Density of the occupied GB states N_B (*left*), values of resistors of GB EEC (*middle*), and time constant of GB circuit branches τ (*right*) plotted against DC bias voltage U_{GB}^{DC} applied across a single GB [Publication II]. Calculated using the semianalytical model using Eqs. 23 and 24 (the DC solution) and the analytical formulas with the parameter values listed in Table 2 and $\sigma_n = 10^{-14}$ cm^2 at 300 K.

The values of the resistors of the EEC and the time constant of circuit branches τ as functions of U_{GB}^{DC} are shown in Fig. 12. The values of the circuit elements in the circuit branches R_{char}–C_{char} and R_{mod}–L_{mod} are negative. The circuit branches disappear at $U_{GB}^{DC} = 0$, because R_{char} and R_{mod} approach $-\infty$. The time constant τ decreases with U_{GB}^{DC} due to the increase of n_B^{DC}.

The effective parallel conductance and capacitance of the sample (i.e. the real and the normalized imaginary parts of the admittance, $\Re\{Y\}$ and $\Im\{Y\}/\omega$, respectively) are plotted against frequency with various values of the DC bias voltage U_{DC} applied across the sample in Fig. 13. The comparison between the analytical and the ATLAS numerical simulation data is shown. The agreement between the analytical and the ATLAS results is very good in the whole frequency range for low DC bias voltages ($U_{DC} \lesssim 0.1$ V, i.e. less than 20% of $V_{B_0}^{max}$), whereas for high U_{DC} there is a larger discrepancy, because the simplified formulas, Eqs. 23 and 24, were used in the derivation of the model.

The different regions and electrical phenomena in the material determine the electrical behaviour of the granular semiconductor in different frequency ranges: At very high frequencies ($> 10^{11}$ Hz in Fig. 13) the bulk regions (i.e. R_s and C_s) define the electrical response of the material (see Figs. 7 and 13). At intermediate frequencies (10^4–10^8 Hz) the ordinary GB conductance and capacitance (i.e. R_{diff} and C_{dep}) determine the admittance. The electronic trapping at GBs represented by the circuit branches R_{char}–C_{char} and R_{mod}–L_{mod} gives a strong response at low frequencies ($< 10^2$ Hz), mostly due to the modulation of the GB potential barrier (i.e. the

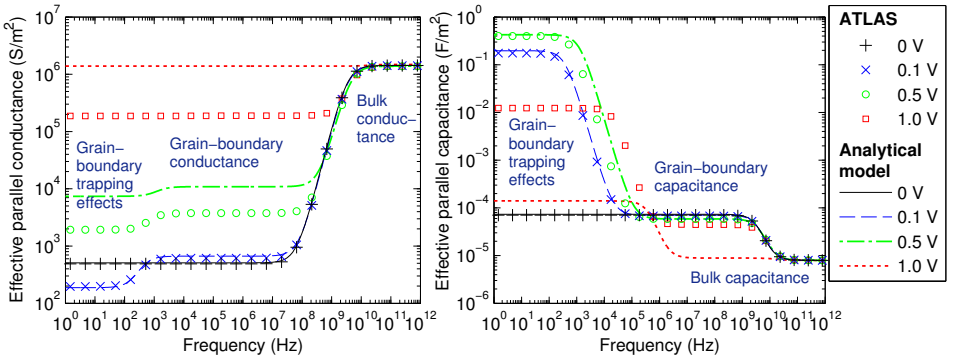

Figure 13: Effective parallel conductance (*left*) and capacitance (*right*) plotted against frequency with various values of the DC bias voltage U_{DC} applied across the sample [Publication II]. Calculated using ATLAS and the analytical model with the parameter values listed in Table 2 and Fig. 12 and the DC solution of N_B shown in Fig. 12 at 300 K.

circuit branch R_{mod}–L_{mod}). Fig. 13 also shows that the trapping effects disappear at $U_{DC} = 0$ V and the GB trapping effects shift to higher frequencies with increasing U_{DC}. In addition to these effects, the electrical properties of each grain vary statistically in real granular materials. This gives rise to further dispersion in the admittance spectrum of the material [1].

3.3 Transient electrical characteristics of granular semiconductors

In Publication III the electrical transients induced by both voltage and temperature changes were calculated for the low voltages, where the effect of the bulk resistance disappears and Eqs. 6 and 7 reduce to $I = I_{GB}$ and $U_{GB} = U/N_{GB}$. The DC results calculated with the same parameter values as the transient case are given in Publication III.

The densities of the charging and discharging currents (see Eq. 17) were negligible in all the calculated transients. However, if trapping takes place in a much larger area than the path of the current (which is possible, for example, in the case of mobile ions or traps), then the magnitudes of the charging and discharging currents would be greatly amplified [40, Publication VI].

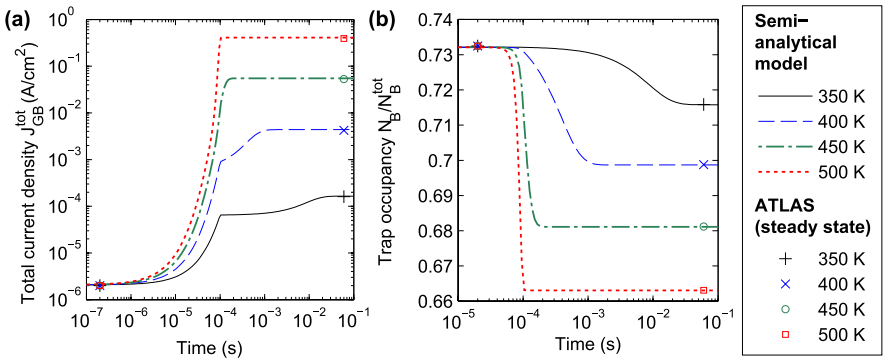

Figure 14: Evolution of (a) the total electric current density in the GB region and (b) the trap occupancy after ramping linearly up temperature between 0–0.1 ms from 300 K to various values (350–500 K) [Publication III]. The data was calculated using the semianalytical model and ATLAS with the applied voltage $U_{GB} =$ 10 mV and the parameter values listed in Table 2 and $\sigma_n = 10^{-14}$ cm^2.

3.3.1 Temperature change

The transients induced by temperature changes were calculated using the semianalytical model. The calculation of these kinds of transients is not supported by ATLAS. However, the steady-state results of ATLAS are shown here for comparison. Transients caused by ramping up (i.e. linearly increasing) temperature are shown in Fig. 14. Fast temperature ramping is possible, for example, by using microhotplate devices (see Section 4). ATLAS and the semianalytical model are in excellent agreement in the steady states.

When the temperature is linearly increased from the initial value of 300 K, the total current density in the GB region J_{GB}^{tot}, which consists almost entirely of the DC component J_{GB}^{DC} (see Eq. 17), increases exponentially with temperature (see 0–10^{-4} s in Fig. 14). The increase is caused by the explicit temperature dependence of the DC current component J_{GB}^{DC} (see Eq. 19, 21, or 23). At 10^{-4} s the temperature ramping phase of the transients of Fig. 14 change into an intermediate phase where the trap occupancy and the total current density are constant. In the 350 K transient of Fig. 14 this phase lies between $1 \cdot 10^{-4}$ s and $2 \cdot 10^{-4}$ s. In the transients with higher temperature, the intermediate phases are much shorter.

The intermediate phase is followed by the releasing phase, where the GB traps are emptied causing the decrease of the height of the GB potential barrier, thereby increasing the flow of current. In the 350 K transient of Fig. 14 the releasing phase

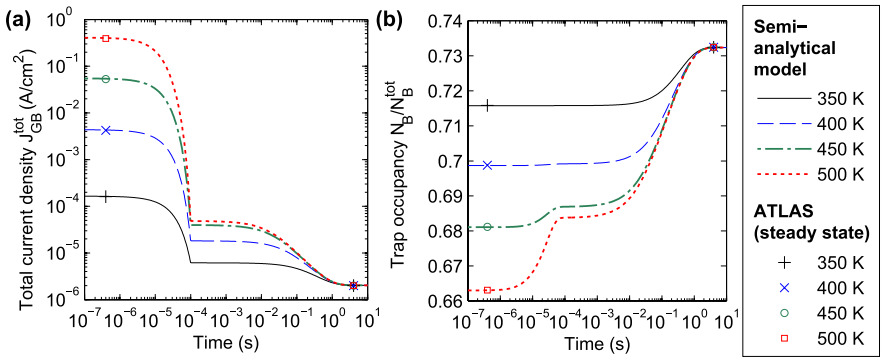

Figure 15: Evolution of (a) the total electric current density in the GB region and (b) the trap occupancy after ramping linearly down temperature from various values (350–500 K) to 300 K between 0–0.1 ms [Publication III]. The data was calculated using the semianalytical model and ATLAS with the applied voltage $U_{GB} = 10$ mV and the parameter values listed in Table 2 and $\sigma_n = 10^{-14}$ cm^2.

lies between $2 \cdot 10^{-4}$ s and $4 \cdot 10^{-2}$ s. The releasing phase begins earlier and the transient has higher magnitude when the final temperature is higher. In fact, in the 450 K and 500 K up-ramps the intermediate phase disappears and the release of electrons begins already in the temperature ramping phase.

The release of electrons from the GB traps is caused by the enhancement of the electron emission process (see Eqs. 26 and 30) due to the increased thermal energy of the electrons. The exponential increase in the electron density n_B at the GB with temperature (see Eq. 20, 22, or 24) retards the overall trap releasing process, because the increased n_B enhances the trapping of electrons.

Transients caused by ramping down (i.e. linearly decreasing) temperature are shown in Fig. 15. Again, ATLAS and the semianalytical model are in excellent agreement in the steady states. Similarly as in the temperature up-ramps transients of Fig. 14, the total current density J_{GB}^{tot} in the GB region in the down-ramps of Fig. 15 consists mostly of the DC component and decreases exponentially with decreasing temperature.

As for the temperature up-ramp transients, the temperature down-ramp transients consist of three phases: the temperature ramping phase (10^{-7}–10^{-4} s in Fig. 15), the intermediate phase (where J_{GB}^{tot} and the trap occupancy are constant), and the trapping phase. In the 350 K transient of Fig. 15 the intermediate phase is between

10^{-4} s and 10^{-2} s, and the trapping phase between 10^{-2} s and 10^{1} s. The decrease of temperature causes filling of the GB traps due to the reduced trap emission rate, which is caused by the decrease of the thermal energy of the electrons. At higher initial temperatures (450 K and 500 K) the electrons are trapped in the GB interface states already in the temperature ramping phase. Again, this enhancement in the electron trapping is caused by the fact that the electron density n_B at the GB is exponentially larger at higher temperatures.

3.3.2 Voltage change

In Publication III two different cases were considered: the on and off-transients induced by voltage changes. In the on-transient the voltage U_{GB} across the GB region is first zero, and then it is ramped up to a desired value. In the off-transient U_{GB} has first an initial (non-zero) value, and then it is ramped down to a certain value. Compared to ATLAS, the MATLAB calculations employing the semianalytical model were 4 orders of magnitude faster on a standard PC computer, yet having the same accuracy (see below and Publication III). In addition, in Publication III it is argued that ATLAS miscalculates slightly the time-dependencies of the transients. Due to this small difference, slightly different values for the electron capture cross-section σ_n had to be used in ATLAS.

The on-transients calculated with various values of the applied voltage U_{GB} are shown in Fig. 16. The results of ATLAS and the semianalytical model are in a good agreement. At higher voltages (1.0 V and 1.6 V) in the first half of the transients the semianalytical model predicts slightly higher trap occupancy and lower current than ATLAS. This is due to the fact that the depletion region approximation and the assumption of low U_{GB} were utilized in the derivation of the semianalytical model. The 1.0 V and 1.6 V applied voltage steps correspond to 80% and 130% of the maximum of the GB potential barrier height $V_{B_0}^{max}$, respectively. As the transient proceeds the difference between the results decreases. ATLAS and the semianalytical model are in excellent agreement in the last half of the transient.

The on-transient has three distinct phases: The ramping phase in the beginning, the trapping phase at the end, and the intermediate phase between the two phases. The off-transient also consists of these phases. However, the final phase is the releasing phase instead of the trapping phase. In the ramping phase (0–1 ns in Fig. 16a) the total current is high and it consists almost entirely of the capacitive current (see Eq. 17). Obviously, the capacitive current disappears after the ramping phase when U_{GB} remains constant. In the intermediate phase, between 10^{-9} and 10^{-2} s in the

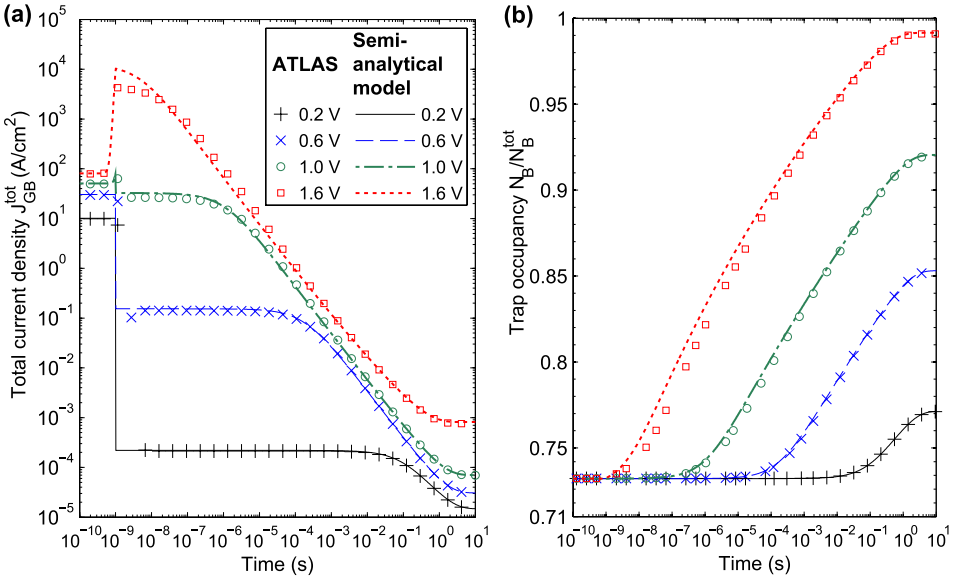

Figure 16: Dynamic behaviour of (a) total electric current density in the GB region and (b) trap occupancy after applying various voltage U_{GB} up-ramps between 0–1 ns (on-transient) calculated at 300 K using ATLAS and the semianalytical model with the parameter values listed in Table 2 [Publication III]. For the capture cross-sections the following values were used: $\sigma_n = 10^{-14}$ cm^2 (ATLAS), and $\sigma_n = 0.292 \cdot 10^{-14}$ cm^2 (model).

0.2 V on-transient in Fig. 16, the current and the trap occupancy are constant. In this phase the total current consists mostly of the DC component J_{GB}^{DC} (see Eq. 17). However, the conduction current J_{GB}^{DC} is higher than in the steady state, because the occupancy of the GB traps has not yet been adjusted to the increased electron density n_B at the GB (see Eq. 20, 22, or 24). In the trapping phase (beginning at 10^{-2} s in the 0.2 V on-transient in Fig. 16) the electrons are trapped in the GB interface states, which decreases the current flow exponentially. The time at which the trapping phase begins depends on the time constant τ of the electron trapping process (see Publication III and Section 3.3.3 below). As the GB potential barrier increases, the concentration n_B decreases and the electron trapping process finally reaches the steady state.

The effect of the increase in the applied voltage is shown in Fig. 16. In addition to the increased capacitive current in the ramping phase, the rate and the magnitude of the transient increase with voltage. This is due to the exponential increase of the

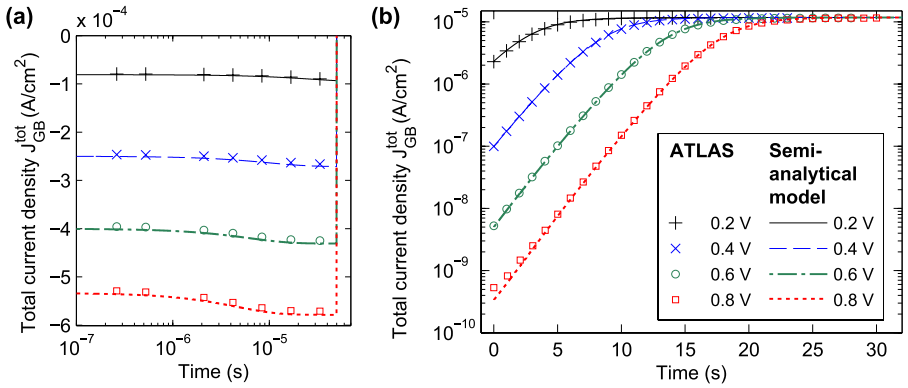

Figure 17: Dynamic behaviour of total electric current density in the GB region after ramping down the voltage U_{GB} from various initial values to 0.1 V in 50 μs (off-transient) calculated (a) in the ramping phase (logarithmic time scale) and (b) in the rest of the transient (linear time scale) at 300 K using ATLAS and the semianalytical model with the parameter values listed in Table 2 [Publication III]. For the capture cross-sections the following values were used: $\sigma_n = 10^{-14}$ cm^2 (ATLAS), and $\sigma_n = 0.292 \cdot 10^{-14}$ cm^2 (model).

electron density at the GB with the voltage. The increased rate of the transient with the voltage can be seen as the shortening of the intermediate phase in Fig. 16. In fact, at 1.6 V there is no intermediate phase. Additionally, at 1.6 V in the beginning of the trapping phase (10^{-9}–10^{-7} s in Fig. 16a) the effective GB potential is so low that the total current density, mostly determined by the DC current component, exceeds the total current in the ramping phase by two orders of magnitude.

The off-transients calculated with various values of the initial applied voltage U_{GB} are shown in Figs. 17 and 18. Again, the semianalytical model agrees very well with ATLAS over the whole duration of the transient for all the values of the initial voltage. The off-transients were calculated with longer ramping times (50 μs) than the on-transients (1 ns) because of converging problems with ATLAS [Publication III]. This affects only the ramping phase, because electrons are not yet released from the traps between 0–10 ms.

Because the voltage is lowered, the total currents, which consist mostly of the capacitive currents, are negative in the ramping phase (0–50 μs in Fig. 17a). In Fig. 17a the increase in the magnitude of the total currents in the ramping phase at 1–10 μs is caused by the decrease of the DC component J_{GB}^{DC} which flows in the opposite direction to the capacitive current.

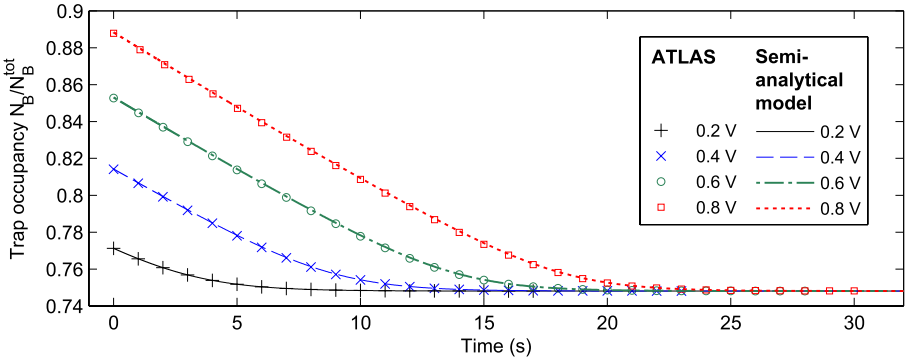

Figure 18: Trap occupancy during the off-transients of Fig. 17 [Publication III].

The releasing phases of the off-transients differ markedly from the trapping phases of the on-transients. Whereas the trap occupancy in the on-transients change logarithmically as a function of time (see Fig. 16b), the off-transients are nearly linear (see Fig. 18). In addition, the off-transients are slower than the on-transients, and the beginning of the trap releasing phase of the off-transients (at around 0 s in Figs. 17b and 18) does not depend on the initial voltage. These differences are caused by the fact that when the trap occupancy decreases in the off-transient, the electron density at the GB increases exponentially due to the decrease of the GB potential. This, in turn, increases the trapping of electrons, which hinders the overall release of electrons from the GB interface states.

3.3.3 Temperature and voltage dependence of the time constant

In Publication III it was shown that if the voltage step is small (e.g. the GB trap occupancy N_B/N_B^{tot} changes by less than 0.005 during the transient), then the analytical formula of the response (Eq. 34) is accurate. The inaccuracy increases with the magnitude of the voltage change: In the case of the on-transient the analytical response is faster and smaller than the response given by the semianalytical model. In the case of the off-transient the behaviour of the analytical response is the opposite to the on-transient case: the analytical response is slower and larger than the one predicted by the semianalytical model.

The analytical formula for the time constant τ [Publication III (Eq. (39))] allows the study of its dependencies on various parameters. The time constant τ describes the speed of the electronic GB trapping process, which determines the electrical

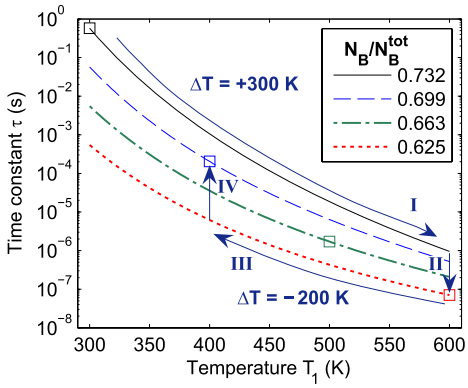

Figure 19: Time constant τ of the trap-occupancy transient plotted as a function of temperature T_1 with various values of the trap occupancy N_B/N_B^{tot}. The temperature step is from T_0 to $T_1 = T_0 + \Delta T$. Calculated for $U_{GB} = 0$ V using the analytical formula given by Eq. (39) of Publication III with the parameter values listed in Table 2 and $\sigma_n = 10^{-14}$ cm^2 [Publication III]. The squares indicate the temperature which corresponds to the steady-state value of N_B/N_B^{tot}. The arrows describe the evolution of τ during transients with increasing ($T_0 = 300$ K, $T_1 = 600$ K) and decreasing temperature ($T_0 = 600$ K, $T_1 = 400$ K), respectively. The phases of the transients (I–IV) are indicated.

response of the granular semiconductor. The evolution of the grain-boundary trap occupancy can be qualitatively described by a first order response, where the time constant τ is changing during the transient [Publication III].

The dependence of τ on temperature with the values of the trap occupancy N_B/N_B^{tot} in the range 0.625–0.732 is shown in Fig. 19. Fig. 19 shows that τ decreases nearly exponentially with temperature for all the values of the trap occupancy.

The curves of Fig. 19 show the evolution of τ during the transients. The squares indicate at which temperature the given trap occupancy N_B/N_B^{tot} is reached in the steady state. In Fig. 19, the part of the curve with higher T_1 than in the steady-state case (i.e. the right-hand side of the curve) corresponds to a temperature ramp-up transient and the part of the curve with lower T_1 than in the steady-state case (i.e. the left-hand side of the curve) to a temperature ramp-down transient, respectively. The time constant τ changes during the transients because the trap occupancy N_B/N_B^{tot} changes. In the temperature ramp-up transients τ always decreases, whereas in the temperature ramp-down transients it always increases.

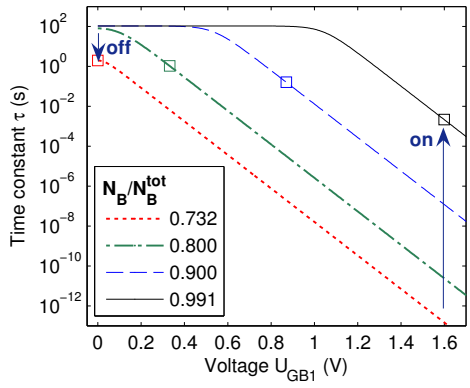

Figure 20: Time constant τ of the trap-occupancy transient plotted as a function of the voltage U_{GB1} applied across the GB region with various values of the trap occupancy N_B/N_B^{tot}. The voltage step is from U_{GB0} to $U_{GB1} = U_{GB0} + \Delta U_{GB}$. Calculated at 300 K using the analytical formula given by Eq. (39) of Publication III with the parameter values listed in Table 2 and $\sigma_n = 10^{-14}$ cm^2 [Publication III]. The squares indicate the value of U_{GB} which corresponds to the steady-state value of N_B/N_B^{tot}. The arrows describe the evolution of τ during an on-transients ($U_{GB0} = 0$ V, $U_{GB1} = 1.6$ V) and an off-transients ($U_{GB0} = 1.6$ V, $U_{GB1} = 1$ mV).

The evolution of τ is illustrated in Fig. 19 for two cases: a temperature ramp-up from 300 K to 600 K and a ramp-down from 600 K to 400 K. Arrows I and II indicate the temperature ramp-up transient. In the steady state at 300 K the trap occupancy N_B/N_B^{tot} is 0.732 and the time constant τ is 0.6 s (see the black square in Fig. 19). When the temperature is rapidly ramped to 600 K, τ drops to 1 μs (arrow I). As the transient proceeds, the trap occupancy N_B/N_B^{tot} decreases causing τ to decrease (arrow II). The lowest value τ reaches, is its new steady-state value: 70 ns (see the red square in Fig. 19). Similarly, in the temperature ramp-down transient from 600 K to 400 K τ jumps from the steady-state value of 70 ns to 6 μs, when the temperature is rapidly decreased (arrow III). Then τ increases with the trap occupancy to the new steady-state value of 0.2 ms (arrow IV).

The dependence of τ on the applied voltage U_{GB} with the trap occupancy values of 0.732–0.991 is shown in Fig. 20. The curves show that at high voltages τ decreases exponentially with U_{GB}. At low voltages there is a flat region. The width of the flat region increases with the trap occupancy.

Similarly as in Fig. 19, the squares in Fig. 20 indicate the voltages U_{GB} corresponding

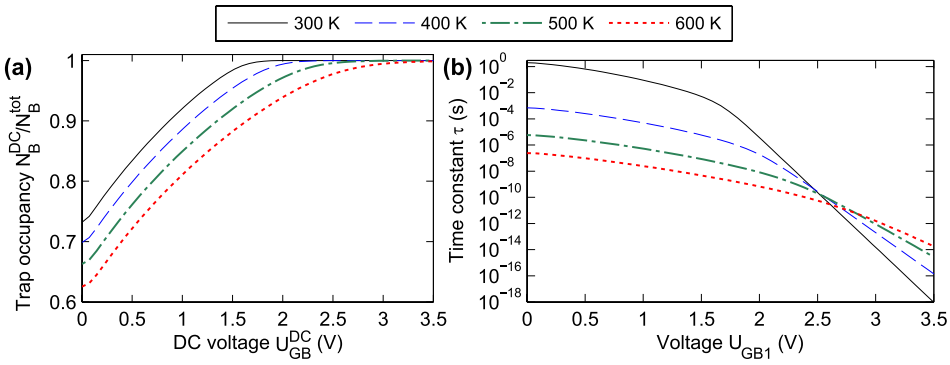

Figure 21: (a) Steady-state trap occupancy and (b) the time constant τ of the infinitesimally small trap-occupancy transient plotted as functions of the DC voltage U_{GB}^{DC} applied across the GB region at various temperatures calculated using (a) the semianalytical model and (b) the analytical formula for τ given by Eq. (39) in Publication III with the parameter values listed in Table 2 and $\sigma_n = 10^{-14}$ cm^2 [Publication III]. Additionally, the τ curves (b) were calculated using the values of N_B^{DC}/N_B^{tot} in (a).

to the steady-state trap occupancies. In Fig. 20 the part of the curve with higher U_{GB1} than in the steady-state case corresponds to an on-transient and the part of the curve with lower U_{GB1} than in the steady-state case corresponds to an off-transient. Right after the voltage change the on-transients have always shorter τ than the off-transients. Again, τ changes during the transients as the trap occupancy changes: τ increases in the on-transients and decreases in the off-transients. In Fig. 20 an arrow indicates an on-transient, where the applied voltage is increased from 0 V to 1.6 V. During the on-transient τ increases with the trap occupancy from the first value after the voltage change, 0.15 ps, to the new steady-state value of 2.0 ms. In the 1.6 V – 1 mV off-transient shown in Fig. 20 τ decreases with the trap occupancy from the first value after the voltage change, 107 s, to the new steady-state value of 2 s.

Fig. 21a shows how the steady-state trap occupancy depends on the DC voltage U_{GB}^{DC} at 300–600 K. The curves were calculated using the semianalytical model in the DC case. As observed before, the steady-state trap occupancy decreases with temperature. In addition, the DC voltage needed to fill the GB traps increases with temperature.

The time constant τ at each DC voltage point at 300–600 K is plotted in Fig. 21b, where τ belongs to a transient caused by infinitesimal changes in either voltage or

temperature. In Fig. 21b the effect of the explicit voltage dependence of τ given by the analytical formula [Publication III (Eq. (39))] (see plots in Fig. 20) and the implicit voltage dependence caused by the voltage dependence of the steady-state trap occupancy N_B^{DC}/N_B^{tot} are combined. The voltage dependence of N_B^{DC}/N_B^{tot} further increases the exponential decrease of τ with voltage. This can be seen in Fig. 21b: there are no flat regions (i.e. voltage independent regions) in the curves. In addition, Fig. 21b shows the nearly exponential decrease of τ with temperature for $U_{GB1} = 0$ V.

3.4 Fitting of the model to experimental data

In Publication III the semianalytical model was fitted to the experimental data obtained from DC and transient measurements of ZnO powder samples. The experiments were carried out by Tua et al. [14]. Unfortunately the transient data is only available for high voltages ($U_{GB} \geq 3.8$ V) [14]. The high voltage region is slightly out of the scope of the semianalytical model because it does not account for hot-electron and minority-carrier effects, which might be present in the experiments [1, 14].

The electrical response was calculated using the semianalytical model with the parameters J_0, $V_{B_0}^{eq}$, r_{BF}, f_n^{eq}, k_0, and L_{GB}^{eq}. The numerical calculation, where Eq. 36 was used instead of Eq. 28 and the charging current was neglected in Eq. 17, and model fitting using MATLAB are described in Publication III.

The measured and fitted electric current density – voltage curves are plotted in Fig. 22. All the GB traps are filled at the high voltages (see Fig. 22b). Fig. 22a shows that the semianalytical model fits surprisingly well to the experimental data in the whole voltage range. The difference between the trap state energy level E_T and the Fermi level E_F in the flat-band case, $(E_T - E_F)_{V_B=0}$, was solved from Eq. 27 using the fitted parameter values. The values of the parameter of the semianalytical model, $(E_T - E_F)_{V_B=0} = -1.040$ eV and $r_{BF} = 2.069$, are similar to the values reported in Ref. [14] which were obtained using the model based on the thermionic-emission theory and hot-electron and minority carrier effects: $(E_T - E_F)_{V_B=0} = -0.8129$ eV and $r_{BF} = 1.840$.

The measured and fitted on-transients are shown in Fig. 23. The reported voltage U_{GB} waveform [14] shown Fig. 23b was also used in the calculations. The voltage U_{GB} applied across the single GB in the transient is high: 3.8 V. The high voltage causes rapid filling of the GB traps (see Fig. 23c).

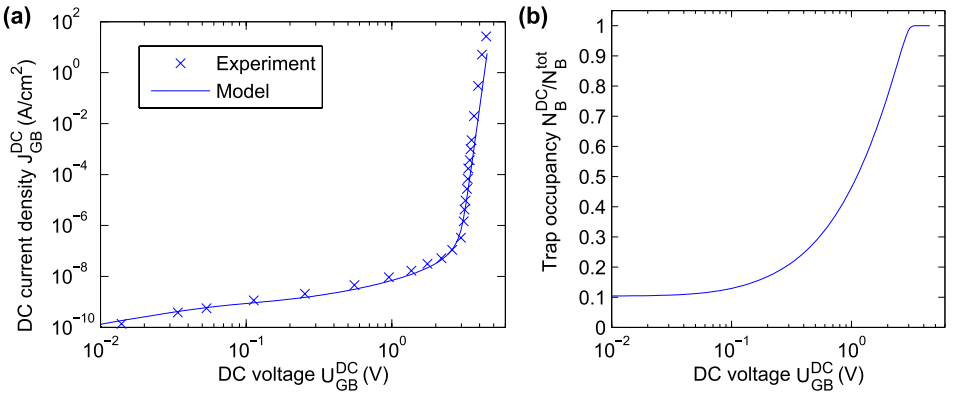

Figure 22: (a) Measured [14] and calculated DC electric current density J_{GB}^{DC} and (b) the trap occupancy N_B^{DC}/N_B^{tot} plotted as functions of the DC voltage U_{GB}^{DC} applied across the GB region [Publication III]. The data was calculated using the semianalytical model with $T = 296$ K and the fitted parameter values $J_0 = 2.024 \cdot 10^9$ A/(cm^{2}V$^{1/2}$), $V_{B_0}^{eq} = 1.095$ V, $r_{BF} = 2.069$, and $f_n^{eq} = 0.1036$.

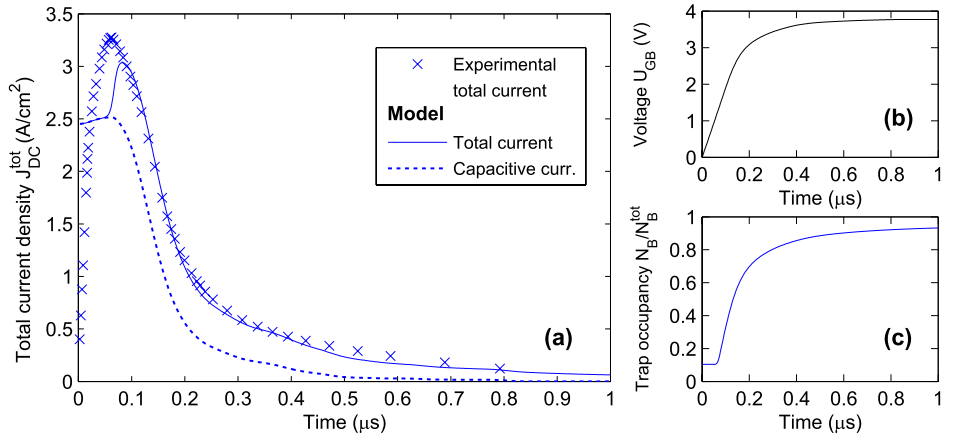

Figure 23: (a) Measured [14] and calculated total electric current density J_{GB}^{tot}, (b) the experimental voltage U_{GB} applied across the GB region, and (c) the trap occupancy N_B^{DC}/N_B^{tot} plotted as functions of time [Publication III]. The density of the calculated capacitive current is shown by the dotted curve. The data was calculated using the experimental U_{GB} data and the semianalytical model with the parameter values in Fig. 22 and the fitted parameter values $k_0 = 0.1142$ 1/s and $L_{GB}^{eq} = 59.30$ nm.

In Fig. 23a the agreement between the experimental and calculated data is excellent for 0.1–1 μs but there is a large difference for 0–0.1 μs: The experimental current rises from zero and the calculated current from 2.45 A/cm^2. As Fig. 23a shows, the current in the beginning of the transient is entirely capacitive. As the transient proceeds the rate of increase of U_{GB} decreases and the capacitive current decays. Due to the time derivative (see Eq. 17) even minute changes in the waveform of U_{GB} have large effects on the capacitive current. This probably is the origin of the observed differences in the beginning of the measured and calculated transients.

3.5 Comparison to other models

In the literature (see Refs. [1, 12, 14] and references therein) mainly the thermionic-emission theory has been employed in the modelling of granular semiconductors. Based on the thermionic-emission theory, a deep-level transient spectroscopy (DLTS) technique for granular semiconductors has also been devised [50]. The DLTS technique and the thermionic-emission based models have been successfully used for accounting for the electrical properties of silicon [50] and a wide range of varistor materials, such as ZnO and SnO_2 [1, 9].

The drift-diffusion theory has also be used in the modelling of granular semiconductors: general DC models (see Refs. [1, 12, 25, 45] and references therein) and models describing the electrical response of gas-sensing granular semiconductors (i.e. metal oxides) to temperature changes [29, 51–55] have been reported. The latter models are valid only for very low voltages (i.e. in the linear I–V region) and they utilize a simple description of the electronic trapping process in the case of chemisorbed oxygen. In addition, the latter models do not describe the dynamic electrical behaviour of the GB region and transients induced by voltage changes. In summary, before the present thesis, a thorough DC, AC, and transient modelling has been performed by using the thermionic-emission theory only.

Although the drift-diffusion and thermionic-emission theories apply to different cases (see Section 1.2.2), they give similar results: At low voltages (i.e. in the linear region) the magnitude of electric current differs only by a pre-exponential constant [12]. The DC characteristics predicted by the thermionic-emission theory are similarly nonlinear [1]. Also, in the thermionic-emission results there is a similarly strong AC response, which is caused by electronic trapping at low frequencies and disappears at zero DC bias voltage [1]. The results of these two theories are also similar in the transient case: In Section 3.4 the model of the present thesis was fitted to the

experimental DC and transient data. The model fitting resulted in similar parameter values as the fitting of the model based on the thermionic-emission theory [14].

Compared to the present thesis the major difference in the other models, in addition to the use of the thermionic-emission theory, is the consideration of the effects caused by multiple GB electronic states or a continuous spectrum of GB states with a various shapes in energy [1], minority carriers [1], and bulk trap states [1, 9]. The latter two are secondary effects which are not present in all cases. Although the case of the electronic GB state with a single discrete energy level is simple, the cases of 1–2 trap states with different discrete energy levels are quite common in granular semiconductors [1, 6, 7, 12, 29].

4 Metal-oxide based resistive gas sensors

Gas-sensitive metal oxides are often deposited as porous polycrystalline films, through which gas molecules can pass. Metal oxides have been studied intensively as gas-sensing materials since the 1960s [56]. The first commercial chemoresistor sensor based on polycrystalline tin oxide (SnO_2) ceramic was released in 1968 by the Figaro Engineering Co. Inc. [56]. Nowadays resistive (i.e. conductometric) gas sensors based on metal oxides are widely available commercially. A wide range of reducing gases (e.g. carbon monoxide (CO), hydrogen (H_2), hydrogen sulfide (H_2S), and hydrocarbons) and oxidizing gases (e.g. oxygen (O_2), ozone (O_3), ammonia (NH_3), chlorine (Cl_2), and nitrogen oxide (NO_x, i.e. NO and NO_2)) can be detected with metal-oxide sensors [7, 8, 11, 15, 57–59]. These sensors are used in fields of safety (e.g. toxic gas and gas leakage detection), security and military (e.g. detection of chemical-warfare agents (CWAs)), environmental monitoring (e.g. air quality monitoring), process control, medicine (e.g. diagnosis and health monitoring), and artificial olfaction (e.g. electronic noses) [7, 8, 15, 58, 60, 61].

Metal oxides are usually granular semiconducting materials [7, 10, 12]. Therefore, the models presented in Sections 1 and 2 can be used for describing these materials. Modelling is discussed in more detail in Section 4.2. Metal-oxide semiconductors are intrinsically either n- (e.g. SnO_2, TiO_2, ZnO, Fe_2O_3, In_2O_3, and WO_3) or p-type semiconductors (e.g. CuO, NiO, and Co_3O_4) [7, 8, 57, 59, 62]. Depending on the dominating gas-sensing mechanism, the materials are either bulk (e.g. TiO_2) or surface type (e.g. SnO_2, ZnO, and WO_3) [7, 10, 62].

The present thesis focuses on the most common gas-sensing metal oxides: the surface-sensitive n-type metal oxides. In these granular materials the main gas-sensing mechanism is based on the adsorption of oxidizing gases, oxygen from air being the most common, on the surfaces of the grains [7, 8, 10–12, 62]. The adsorbed oxidizing gases act as acceptor-type electron traps. As described in Section 1.2, the electric charge of the occupied traps, i.e. ions, give rise to GB potential barriers, which reduce the electrical conductivity of the n-type granular material. Reducing gases are generally sensed based on their reaction with the preadsorbed oxygen ions, leading to an increase in material conductivity as the ions are consumed.

In practice, all resistive metal-oxide gas sensors are operated at an elevated temperature. This ensures that the relevant chemical reactions are activated and they are more specific, i.e. the gas sensors are more selective, and the gas sensors have a reasonable response time [15]. In addition, humidity affects less the sensor response well above a temperature of 100 °C [15]. The typical operating temperature of the

semiconducting metal-oxide gas sensors is 200–400°C [11]. The most common and well-known materials, SnO_2, ZnO, TiO_2 and WO_3, operate at this temperature range [11]. In some cases metal-oxide chemoresistors are operated at up to 700–1200°C [8]. Typically, the metal-oxide sensing material of these gas sensors is heated up with an electric current flowing through a heater resistor. The resistance of the gas-sensing film is measured with separate electrodes. There is also a special one-electrode design, where the heater acts as the measurement electrode of the gas sensing material [63].

The gas-sensing element of the first commercial semiconductor sensor, the Taguchi-type ceramic sensor, is a ceramic bead which has a heater wire inside [56]. The next generation sensors were fabricated with the screen-printing technique on a small and thick ceramic substrates such as alumina [11]. The method allows batch processing which reduced the sensor to sensor variation within the production lots [11]. The main drawback of the Taguchi-type ceramic and the screen-printed sensors is the need for high heating power, which is caused by the large size and the poor thermal insulation of the gas-sensing element [11]. The solution to this drawback is the micromachined sensor, i.e. microsensor, which has a microhotplate for heating up the sensing material [11]. Micromachining provides a small sensor size together with lower power consumption (typically 30–150 mW [11] compared to from 200–1000 mW of the screen-printed sensors [11]) as well as low cost [15]. The first microhotplate designs appeared in the late 1980s [15] and, according to Ref. [15], the first microhotplate sensor was reported in 1993 by Corcoran et al. [64].

The microhotplate design allows the use of various methods for the deposition of the gas-sensing film. They are listed in Table 3. The use of different deposition method leads to a different microstructure of the layer [11]. The screen-printed and drop deposited films are thick (several micrometers), and the CVD, PVD, and RGTO films are thin films (20–1000 nm), respectively [11]. The structure and chemical composition of the gas-sensing film has a large effect on the sensitivity and selectivity of the gas sensor. Commonly the sensitivity of the metal-oxide gas sensors is good and the selectivity is poor [11, 15, 57]. The response of the gas sensor can be optimized, for example, by tuning the microstructure of the gas-sensing film or by using noble metals or metal oxides as additives acting as catalyzers and sensitizers [7, 59, 65]. In addition to the optimization of the gas-sensing material, the poor selectivity can be overcome by using pattern recognition and sensor arrays consisting of a multitude of different sensors [7, 11, 60]. Sensor arrays can even be manufactured on the same chip. The small size and integrability of the microhotplate metal-oxide gas sensors allow them to be used in smart sensors and integrated microsystems [15, 66]. In a smart sensor the sensor and the microelectronic circuitry is integrated

Table 3: Techniques used for deposition of metal-oxide films [11, 68–70].

Deposition type		Technology
Paste/slurry deposition		Screen-printing
		Drop deposition
		Dip coating
		Spray deposition
Chemical vapour deposition (CVD)		Thermal CVD
		Plasma activated CVD
		Laser induced CVD
		Electroless plating
		Atomic layer deposition (ALD)
Physical vapour deposition (PVD)		
	Sputtering	Standard sputtering
		Reactive sputtering
		Cathode sputtering
		With bias voltage
	Evaporation	Molecular beam epitaxy/deposition (MBE/MBD)
		Thermal evaporation
		Reactive evaporation
		Ion plating
		Reactive ion plating
		Arc evaporation
		Laser evaporation
Other		Rheotoxial growth and thermal oxidation (RGTO)

on a single chip (an example of this is reported in Ref. [67]).

The microhotplate gas sensors are manufactured on a single-crystal-silicon wafer. Two different designs are utilized: the closed-membrane type and the suspended-membrane type [11, 15, 71]. The closed-membrane-type microhotplate is shown in Fig. 24. The active area of the microhotplate is located in the middle of the membrane. The membrane is fabricated by removing the silicon from the back side of the wafer by etching [11]. In the suspended-membrane-type microhotplate the active area of the microhotplate is suspended by microbridges. The pit below the microhotplate is made by etching from the front side [11]. Because the suspended-membrane type has less connecting area to the substrate, it typically has lower power consumption.

In the horizontal sensor design the heater resistor is placed on the same plane as the sensing electrodes [11]. In the vertical approach shown in Fig. 24 the heater resistor is on a different plane as the sensing electrodes. The membrane consists of a membrane layer and an insulating layer. The membrane layer is typically silicon nitride and the insulating layer is silicon oxide, but they can also consist of multiple

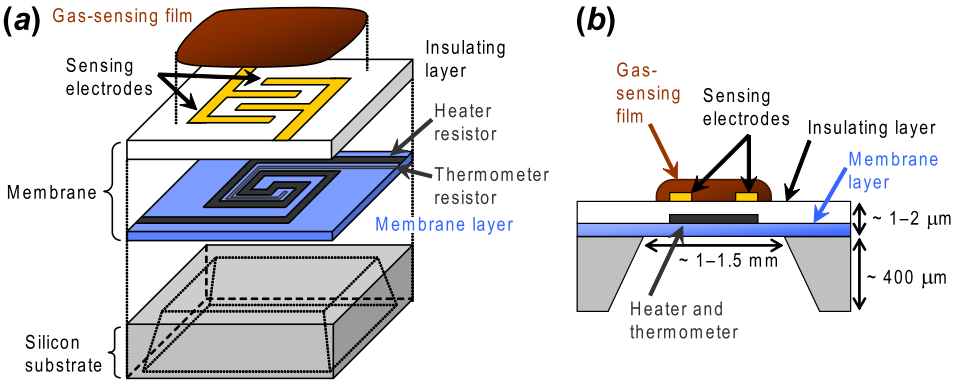

Figure 24: A schematic picture of a closed-membrane-type microhotplate gas sensor viewed from (*a*) top and (*b*) side. The typical dimensions [11] are shown.

layers of silicon nitride and oxide [11].

The heater resistor is located between the membrane and the insulating layers. It is usually made of platinum, polysilicon, or $p++$-doped silicon [11, 15, 29, 67, 71, 72]. By measuring the resistance of the heater resistor while heating, the temperature of the microhotplate can be calculated. The resistance of a platinum heater resistor depends linearly on the temperature [15]. An additional thermometer resistor made of the same material as the heater resistor can also be used for the measurement of the sensor temperature [11]. In addition to the resistors, metal-oxide-semiconductor field-effect transistors (MOSFETs) have been used as the heater element [73–75] and *pn*-diodes as temperature sensors [74, 75].

The heat loss mechanisms and thermal behaviour of microhotplates has been studied extensively (see, for example, Refs. [11, 15, 76] and references therein). The small thermal capacity of the microhotplate leads also to a small thermal time constant, which can be as low as 1 ms or less [11, 71]. This allows rapid modulation of the operating temperature of the microhotplate gas sensor. Temperature modulation techniques [11, 77–81] can be used for improving the overall selectivity of the sensors.

The sensing electrodes are metallic and they are typically interdigitated (see Fig. 24). The interdigitation improves the conductance between the sensing electrodes and the gas-sensing material simply by increasing the cross-sectional area of the electric current. Platinum and gold are the most common contact metals, although aluminium and tungsten have also been used [11, 29].

In order to make the temperature distribution flatter on the microhotplate, a silicon

island or plug [11, 76, 82] or a metallic hotplate layer [29, 83] can be added. A buried or a counter electrode can be used to apply an additional electric field to the gas-sensing film from below in order to create a depletion zone in the bottom of the gas-sensing film [11, 77, 84–88]. By controlling the width of the depletion region, the sensitivity of the gas sensor can be increased. Adding a further electrode pair above or below the gas-sensing film allows the separation of the diffusion and surface effects by a resistive measurement [11, 85, 88].

Microhotplates have also been fabricated using silicon-on-insulator (SOI) substrates and complementary metal-oxide-semiconductor (CMOS) compatible technologies [67, 71, 73–75]. In addition, fabrication on polymers has been reported [89]. This brings the advantages of simplified processing, improved robustness and flexibility, and easier integration of microhotplate-based gas sensors in radio-frequency identification (RFID) flexible tags and textiles [89].

4.1 Novel microhotplate gas sensor with ALD SnO_2 gas-sensing film

Atomic layer deposition (ALD) has been shown to produce higher-quality epitaxial films than conventional chemical vapour deposition (CVD) [68]. While ALD SnO_2 has been used in gas sensing applications before, for instance, Refs. [90–92], Publication IV presents for the first time its use in a microhotplate design.

The fabricated sensor is of the standard closed-membrane type (see Fig. 24). The complete fabrication process is described in detail in Publication IV. The sensor chip, which has two size variations for the active area (500 μm $\times$ 500 μm and 1000 μm $\times$ 1000 μm), mounted inside the aluminium shielding ring on the alumina printed circuit board (PCB), the sensor chip, and an atomic force microscope (AFM) image of the ALD SnO_2 gas-sensing film are shown in Fig. 25. The shielding ring (see Fig. 25a) together with an o-ring allows gas-tight connection to the gas testing equipment described in Publications IV and V.

The sensor has separate heater and thermometer resistors (see Fig. 25b). Plasma-enhanced chemical vapour deposited (PECVD) silicon dioxide (SiO_2) was successfully used as the intermetal dielectric. In addition to the conventional heater and thermometer resistor material platinum, the use of tungsten was investigated as well. However, in spite of the use of a protective tungsten nitride layer above and below the metal layer, tungsten began to oxidize after continuous operation at 300 °C for 12–16 days. Since the oxidation of tungsten did not affect the sensor operation before this time, the sensors with the tungsten heater and thermometer can be

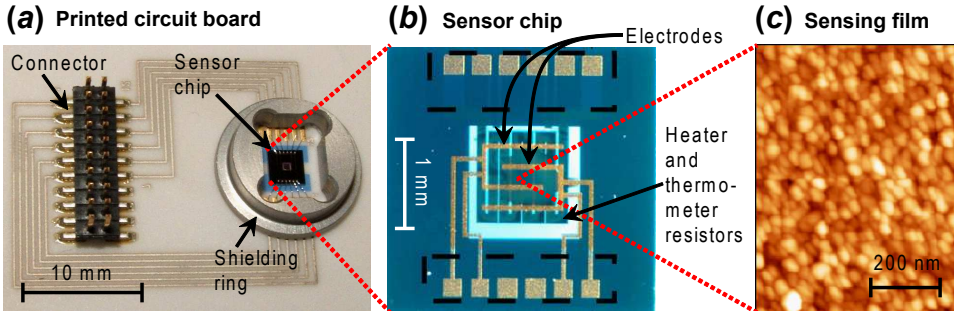

Figure 25: (a) The sensor chip mounted inside the aluminum shielding ring on the alumina printed circuit board (PCB). (b) The completed microhotplate chip. The dashed lines indicate the areas from which the ALD-deposited SnO_2 was removed by etching. The contact pads are located inside these areas. (c) AFM height image of the ALD-deposited SnO_2 gas-sensing film.

used for prototyping and testing purposes. With the low heating powers of 80 mW (500 μm $\times$ 500 μm device) and 180 mW (1000 μm $\times$ 1000 μm device) at 300 °C and the stabilization times of a few seconds, the characteristics of the microhotplates are comparable to the typical characteristic reported in literature [11].

Unlike in the standard process [11] the ALD film (see Fig. 25c) was deposited and patterned by wet etching prior to the KOH etching of the silicon from the back side. The ALD step was crucial in the fabrication process, since the deposition temperature is high: 500 °C. In order to stabilize the structure, it was annealed at 500 °C for 24 h before the ALD step. The 17.5 nm thick ALD SnO_2 film consists of nanosized grains in the size range of 35-50 nm. The RMS surface roughness is approximately 3.6 nm. Long sensor operation tests at 300 °C showed that the ALD film exhibited a very low drift in the electrical resistance, which can be seen as an indication of a structurally stable SnO_2 layer.

The response of the sensor to ethanol, acetone, and acrylonitrile vapours is shown in Fig. 26. These chemicals are all widely used in many fields of industry, and are representative of the kind of flammable or toxic materials that are easily vaporized into the workplace air. The sensitivity of the sensor to a specific gas can be calculated with the formula

$$S = \frac{G_{sh}^{gas}}{G_{sh}^{air}}, \tag{40}$$

where G_{sh}^{gas} is the sheet conductance of the gas-sensing film in the presence of the target gas and G_{sh}^{air} in clean air. The sensitivities and the $t_{50\%}$ and $t_{90\%}$ response

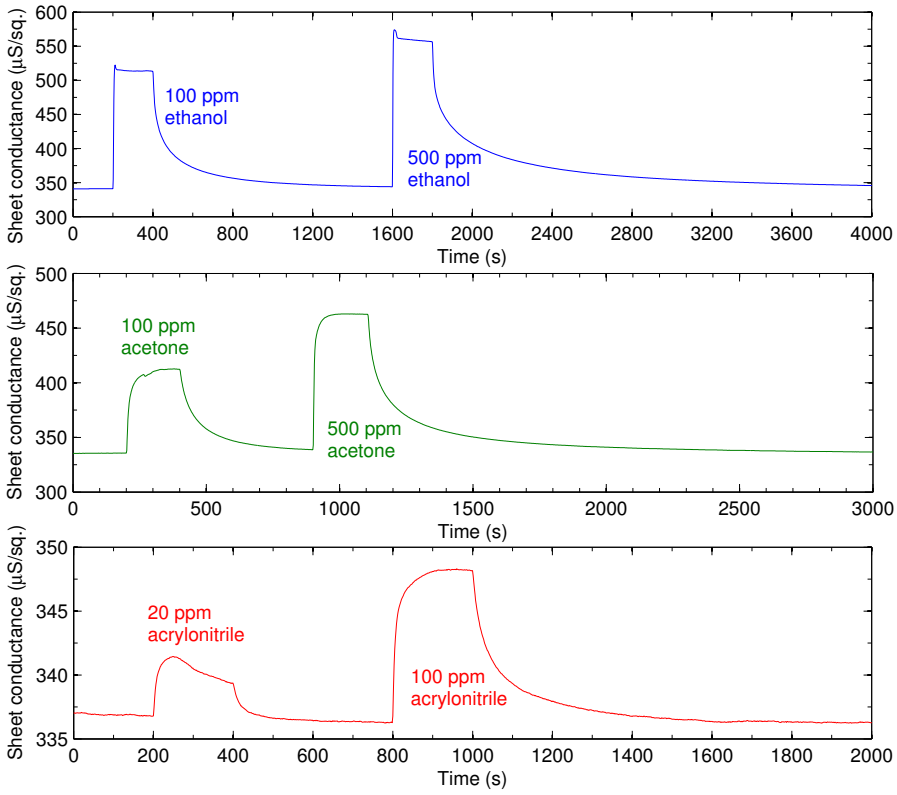

Figure 26: The response of a 500 μm $\times$ 500 μm device at 300 °C operating temperature to 200 s pulses of two different concentrations of ethanol (*top*), acetone (*centre*), and acrylonitrile (*bottom*) [Publication IV]. The sheet conductance of the gas-sensing film is shown. Measured in clean air at 32 % relative humidity (RH).

times (the time taken for 50% and 90% of the overall response to occur, respectively) calculated for the pulses shown in Fig. 26 are listed in Table 4.

Being reducing gases, ethanol, acetone, and acrylonitrile rapidly increase the conductivity of the gas-sensing film (see Fig. 26). This is in agreement with other n-type metal-oxide gas sensors [10]. The sensitivities listed in Table 4 appear relatively low compared to values reported in literature (see e.g. Ref. [93]). However, the current sensors have not been doped with any catalyst material, as is commonly done in this type of sensors to improve sensitivity. In addition, the dense thin film produced

Table 4: Sensitivities and response times of small (500 μm $\times$ 500 μm) sensor operating at 300 °C [Publication IV].

Gas	Sensitivity	$t_{50\%}$ (s)	$t_{90\%}$ (s)
Ethanol 100 ppm	1.51	3.4	5.9
Ethanol 500 ppm	1.64	2.3	3.0
Acetone 100 ppm	1.23	8.1	46.2
Acetone 500 ppm	1.38	4.2	20.2
Acrylonitrile 20 ppm	1.008	3.0	5.6
Acrylonitrile 100 ppm	1.035	5.2	43.5

by the ALD process may be expected to have a lower response than a thick porous film produced from powder or paste, with its inherent large surface-to-volume ratio. The responses to the gases are extremely fast, as seen from the response times listed in Table 4.

4.2 Modelling resistive metal-oxide gas sensors

Models describing resistive surface-type metal-oxide gas sensors have two general parts: the adsorption and conduction models. These models are usually connected to each other. Therefore, they must be solved simultaneously. The gas adsorption model describes how gases are adsorbed on the surface of the granular film and how the electrical properties of the surfaces and the grain boundaries are changed as the result of the adsorption. Mainly the electronic states are considered. Although granular metal-oxide materials can support various types of electronic states (see Section 1.2), it is often assumed that the electronic states related to the adsorbed gas species (i.e. extrinsic states) dominate. In the present thesis only these extrinsic states are considered. The conduction model described the electrical conduction through the granular film. In this thesis the conduction is described by the model presented in Section 2.

From the adsorption theory point of view the adsorption can be described, for example, either by the Langmuir or Wolkenstein isotherms. In the simple Langmuir model the bonding energy between the adsorbate and the surface is independent on the coverage of adsorbate [4, 46]. Being more complicated, the Wolkenstein model takes into account the electronic coupling between the semiconductor and the adsorbate [5, 7, 30, 46]. Several models based on Wolkenstein's approach have been proposed [43, 46, 94–98].

There is also a simplified approach, where the adsorption itself is described in a simplified manner, for example, by the mass-action-type rate equations. These kinds of models [29, 51–54] are often called the surface state models. They are conceptually similar as in the early modelling work of Clifford and Tuma [99, 100]. The surface-state models focus on the electronic trapping in extrinsic surface states (i.e. oxygen ionization), since it is the key phenomenon in metal-oxide gas sensors. In the present thesis the gas adsorption is described by the surface-state model presented below.

4.2.1 Surface state model

In the typical operating temperatures of resistive n-type surface-sensitive metal-oxide gas sensors, 300–400°C, oxygen is chemisorbed dissociatively and the atomic oxygen O^- ion is the dominant oxygen species on the surface [12, 29, 46, 101, 102]. In this case the oxygen chemisorption reaction can be written as [52–54]

$$\frac{1}{2}\,\mathrm{O}_{2\,\mathrm{gas}} + \mathrm{S}_{\mathrm{ads}} \;\rightleftarrows\; \mathrm{O}_{\mathrm{ads}}, \tag{41}$$

where $\mathrm{S}_{\mathrm{ads}}$ denotes an adsorption site and $\mathrm{O}_{\mathrm{ads}}$ a chemisorbed neutral oxygen atom (i.e. adatom). The oxygen ionization, i.e. electron extrinsic surface state trapping reaction, can be written as [52–54]

$$\mathrm{O}_{\mathrm{ads}} + \mathrm{e}^-_{\mathrm{free}} \underset{\longleftarrow}{\overset{k_i}{\longrightarrow}} \mathrm{O}^-_{\mathrm{ads}}, \tag{42}$$

where $\mathrm{e}^-_{\mathrm{free}}$ is a free electron and $\mathrm{O}^-_{\mathrm{ads}}$ an ionized oxygen adatom (i.e. adion), and k_i and k_{-i} are the rate constants for oxygen ionization, i.e. electron extrinsic surface state trapping and emission, respectively.

The interaction of the reducing gas R with the gas-sensing film is often complex and involves many steps [10, 103]. However, it usually is enough to represent the reaction of the ionized surface oxygen $\mathrm{O}^-_{\mathrm{ads}}$ with the reducing gas by a simple irreversible reaction [52–54]

$$\mathrm{O}^-_{\mathrm{ads}} + \mathrm{R} \;\xrightarrow{k_r}\; \mathrm{RO} + \mathrm{S} + e^-_{\mathrm{free}}, \tag{43}$$

where the reducing gas R reacts with the preadsorbed oxygen ions $\mathrm{O}^-_{\mathrm{ads}}$ and leaves the surface as RO. k_r is the rate coefficient of the reaction between the reducing gas R and the preadsorbed oxygen ions $\mathrm{O}^-_{\mathrm{ads}}$. Reactions (42) and (43) lead to the rate equation for the density of the occupied GB states [52–54]:

$$\frac{dN_B}{dt} = k_i n_B N_{\mathrm{O}} - k_{-i} N_B - k_r[\mathrm{R}] N_B, \tag{44}$$

where $N_{\mathrm{O}} = [\mathrm{O_{ads}}]$ is the density of the neutral adsorbed oxygen, $N_B = N_{\mathrm{O^-_{ads}}} = [\mathrm{O^-_{ads}}]$ the density of ionized oxygen adatoms (i.e. the density of the occupied extrinsic surface states), n_B the electron density at the grain boundary, and [R] the concentration of the reducing gas. The total density of the adsorbed oxygen is $N_{\mathrm{O}}^{tot} = [\mathrm{O_{ads}}] + [\mathrm{O^-_{ads}}] = N_{\mathrm{O}} + N_B$.

Assuming that reducing gas or applied voltage do not affect the total density of the adsorbed oxygen, the steady-state solution of the rate equation (Eq. 44) at the temperature $T = T_{eq}$ can be written in a normalized form as [Publication V]

$$\nu_{DC} = \frac{N_B^{DC}}{N_B^{eq}} = \frac{\frac{n_B^{DC}}{n_B^{eq}}}{1 + \alpha_R + f_n^{eq}\left(\frac{n_B^{DC}}{n_B^{eq}} - 1 - \alpha_R\right)}, \tag{45}$$

where the parameter $\alpha_R = \frac{k_r}{k_{-i}}[\mathrm{R}]$ determines how strongly the reducing gas removes the oxygen ions.

4.3 Bias voltage dependence of sensitivity

The bias voltage dependence of sensitivity in metal-oxide (SnO_2) gas sensors was reported for the first time by Durrani [104]. The same effect was also reported in WO_3 gas sensor in Publication V, where we also described the effect using a quantitative model. Later, the effect was also reported in HfO_2 gas sensors by Durrani and Al-Kuhaili [105].

In Publication V the bias voltage dependence of the gas sensitivity was studied on commercial resistive WO_3 closed-membrane-type microhotplate gas sensors MOS1 and MOS2 from Environics Oy developed for ChemPro®100i handheld chemical detector [106]. The details of the sensors and the experiments are given in Publication V. The phenomenon was studied by carefully measuring the I–V relations of the sensors in clean air and in the presence of a reducing gas (50 ppm ethanol). During the I–V measurements the power of the measurement signal heats up the sensors. In order to remove this effect, the temperature of the sensors was kept constant by using a PI controller.

The sensor responses were described using the models presented in Sections 2 and 4.2.1. The GB DC electric current density J_{GB}^{DC} and the steady-state electron density at the GBs n_B^{DC} were calculated with the simple approximative formulas (Eqs. 23 and 24) and the effect of the bulk of the granular film was neglected. Thus, the

DC electric current flow through the granular gas-sensing film can be written in an approximate form as [Publication V]

$$I_{DC} = \sqrt{2} I_0 \sqrt{V_{B_0}} \exp\left(-\frac{qV_{B_0}}{k_B T}\right) \sinh \frac{qU_{DC}}{2k_B T N_{GB}^{eff}}, \tag{46}$$

where $I_0 = A_{eff} J_0$, A_{eff} is the effective cross-sectional area of the film, N_{GB}^{eff} the effective number of grain boundaries in the path of the electric current, and the GB potential barrier V_{B_0} is calculated using the approximative formula $V_{B_0} = qN_B^2/(8\varepsilon N_d)$ and the corresponding normalized formula [Publication V (Eq. (28))] instead of Eqs. 4 and 28. The sensitivity of the sensor is calculated with the formula

$$S = \frac{I_{gas}}{I_{air}}, \tag{47}$$

where I_{gas} is the electric current in the presence of the target gas (i.e. in air-ethanol atmosphere) and I_{air} in clean air, respectively. Numerical calculations using Eqs. 45, 46, and 47, and model fitting are described in detail in Publication V.

The measured and fitted I–V curves of the MOS2 sensor in dry clean air and in air-ethanol atmospheres are shown in Fig. 27a. The I–V curves have the same three characteristic regions (i.e. linear, sublinear, and superlinear) which were observed in the theoretical calculations presented in Section 3.1. The fourth region, i.e. the series resistance limited region, is not shown in Fig. 27a because high enough voltages would have caused too much heating of the gas-sensing film. The sensitivity calculated from Fig. 27a is plotted in Fig. 27b. The sensitivity decreases strongly with increasing DC bias voltage. Fig. 27 shows that the model is in excellent agreement with the experimental data. Similar I–V and sensitivity curves were also observed in humid air and with the MOS1 sensor. The model was also able to represent that data well.

The calculated GB potential V_{B_0} and the ion ratio (i.e. the trap occupancy) N_B^{DC}/N_B^{tot} of the MOS2 sensor as functions of DC bias voltage are shown in Fig. 28. The obtained values for the GB potential barrier $V_{B_0}^0$ are in the range 0.89–1.07 V [Publication V]. This range is typical for metal-oxides, including WO_3 [1, 7, 12, 46].

The sensitivity degradation effect can be explained using the present model. It is caused by the differences in the shapes of the I–V curves in clean air and in the presence of the reducing gas. These differences, in turn, are caused by differences in electron trapping (i.e. oxygen ionization). In clean air the traps are already almost filled and practically no further trapping is possible at higher voltages (see Fig. 28). In the reducing gas atmosphere the filling of the traps is possible because

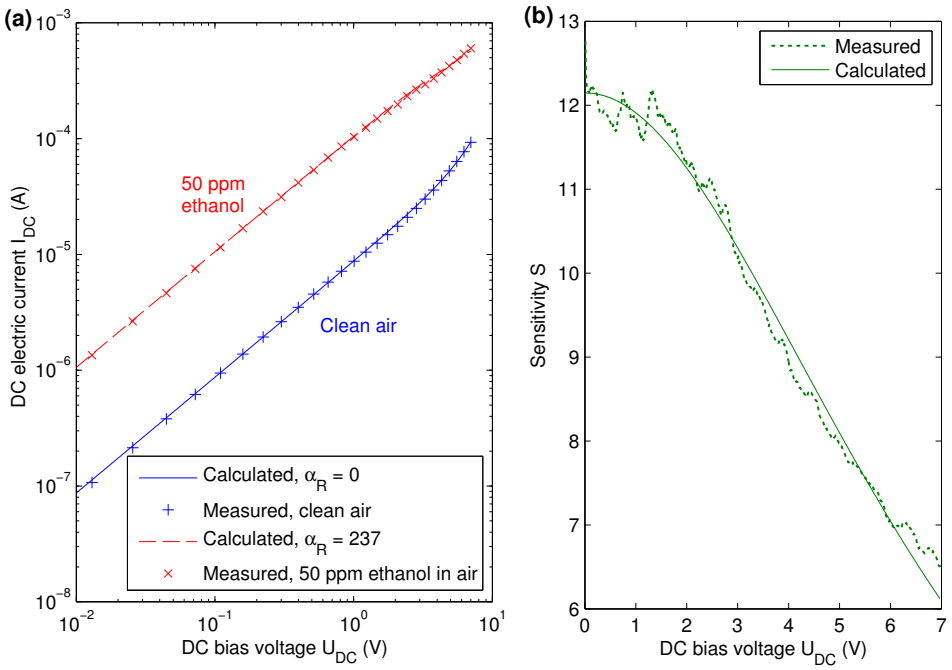

Figure 27: Measured and calculated (a) I–V curves of the MOS2 sensor in dry clean air and air-ethanol atmospheres at 360 °C operating temperature and (b) the corresponding sensitivities as functions of the DC bias voltage [Publication V]. The fitted model parameter values are $I_0 = 336.2$ AV$^{-0.5}$, $f_n^{eq} = 0.9948$, $V_{B_0}^{eq} = 0.8935$ V, and $N_{GB}^{eff} = 33.83$.

the reducing gas removes some of the oxygen ions, i.e. the occupied traps (see Fig. 28). This has a large effect on the I–V curves: The trapping in reducing gas atmosphere limits the increase of the electric current with voltage compared to the clean air case, where practically no further trapping takes place causing the current to increase exponentially with voltage soon after the linear region. Because of these differences in the sublinear region of the I–V curves, the overall effect is that the sensitivity decreases with increasing DC bias voltage.

The influence of trapping on sensitivity is, however, more complicated in general. The case discussed here corresponds to trap filling regime, since already in thermodynamical equilibrium in clean air over 99% of traps are filled. It turns out that at the opposite limit, where the occupancy of traps f_n^{eq} is lower ($f_n^{eq} \lesssim 0.7$), the sensitivity remains almost constant or increases slightly with the bias voltage.

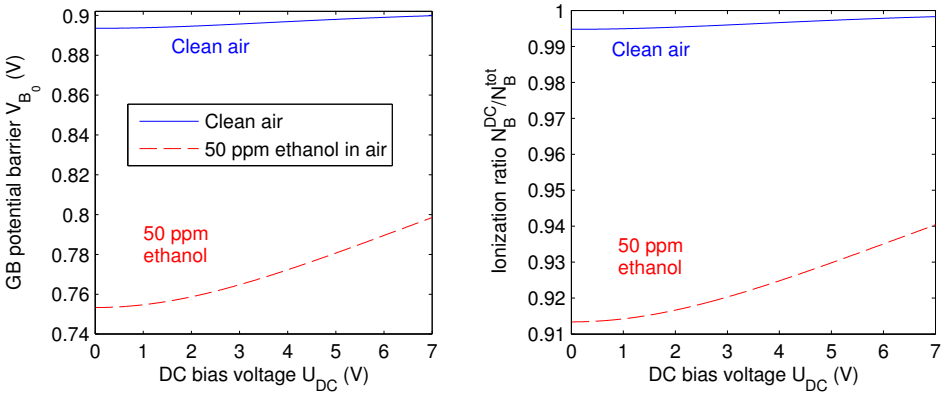

Figure 28: Calculated GB potential barrier V_{B_0} (*left*) and the ion ratio (i.e. the trap occupancy) N_B^{DC}/N_B^{tot} (*right*) in the MOS2 sensor as functions of DC bias voltage [Publication V]. The model parameters are from Fig. 27.

The present model was used for studying the bias-voltage dependent sensitivity effect in the general case. The I–V curves of a theoretical gas-sensing film, and the corresponding sensitivities, the GB potential barrier height, and the ion ratio as a functions of the DC bias voltage in clean air and in air-reducing gas atmospheres are plotted in Fig. 29. They were calculated with various values of the GB trap occupancy in the thermodynamical equilibrium f_n^{eq}. Fig. 29a shows that with lower values of f_n^{eq} the sublinear region in I–V curves is more dominating and the strongly increasing current region, i.e. the superlinear region, is shifted to higher voltages. This is due to the fact that more empty GB states are available for trapping when f_n^{eq} is low (see Fig. 29d). The constant sensitivity observed with low f_n^{eq} is caused by the fact that the trapping takes place to the same extent when the sensor is both in air-reducing gas atmosphere and in clean air. This results in similar bias voltage dependence of V_{B_0} in both atmospheres, and thus the sensitivity does not change with the voltage. A slight increase of sensitivity with increasing DC bias voltage is caused by the fact that with lower values of f_n^{eq} the GB potential barrier V_{B_0} increases slightly faster in clean air than in the presence of reducing gas (a few millivolts in Fig. 29c). This is amplified by the exponential dependence of the electric current on V_{B_0} (see Eq. 46).

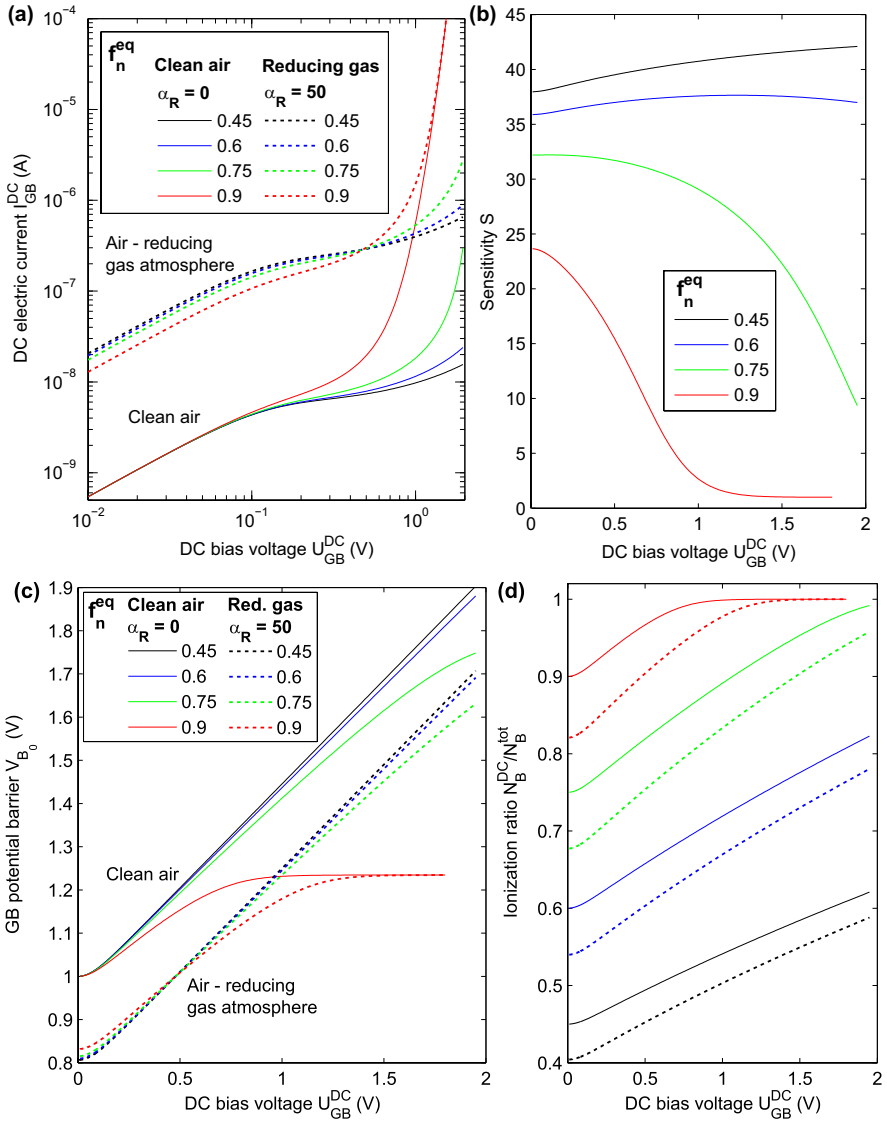

Figure 29: (a) Calculated I–V curves of a theoretical gas-sensing film and (b) sensitivities, (c) GB potential barrier V_{B_0}, and (d) ion ratio N_B^{DC}/N_B^{tot} as functions of the DC bias voltage. Calculated with various values of the GB trap occupancy in the thermodynamical equilibrium f_n^{eq} and $I_0 = 1$ AV$^{-0.5}$, $V_{B_0}^{eq} = 1$ V, and $N_{GB}^{eff} = 1$ in clean air and in air-reducing gas atmospheres at 600 K.

4.4 Negative admittance effect

Negative admittance, negative capacitance, or anomalous inductive effect has been reported in various semiconductor devices and materials [1, 107, 108]: for example, in organic light-emitting diodes (OLEDs), ZnO varistors, and quantum well infrared photodetectors. In SnO_2 negative capacitance has been observed by Varghese et al. [109] and Kaur et al. [110]. Both of the groups explained the phenomenon by the movement of adsorbed ions. In Publication VI we showed that the effect can also be explained by the barrier-limited conduction and electron trapping at grain boundaries, which are the fundamental phenomena in granular semiconductors. In Publication VI, the negative admittance effect was studied on the same samples as in Section 4.3 and Publication V. The model presented in Section 2.3 was utilized in the quantitative explanation of the results.

4.4.1 Measurement of admittance spectra

The sub-hertz regions of the admittance spectra of the sensors were measured with a special measurement scheme. A LabVIEW™ program runs a Keithley 236 unit operating as a voltage source via a general purpose interface bus (GPIB). The applied voltage is varied and the unit also measures the current. The applied voltage signal consists of a constant DC bias and uniformly distributed pseudorandom components. This input signal has a flat power spectral density, which allows the measurement of the admittance spectrum.

The admittance spectra were calculated from the recorded current and voltage signals using a built-in LabVIEW function. First, the LabVIEW function transforms the current and voltage signals recorded in the time domain into the frequency domain using a fast Fourier transform (FFT) algorithm [111]. Before the transformation the signals are multiplied by a window function. In this thesis the Hanning (i.e. Hann) window function was used because it produces a good compromise between the high accuracy in magnitude and the high accuracy in frequency [112]. After the transformation the LabVIEW function calculates the admittance spectrum using the formula $Y(\omega) = I(\omega)/V(\omega)$, where $I(\omega)$ and $V(\omega)$ are the recorded current and voltage signals in the frequency domain.

Since the FFT algorithm is based on invariant sampling interval, the LabVIEW program has special waiting loops in order to keep the sampling interval constant. The correct operation of this measurement scheme was verified by a test circuit built from commercial passive components. Further experimental details are given in Publication VI.

4.4.2 Results of experiments with commercial gas sensors

In Publication VI it was shown that the EEC model shown in Fig. 8a fits well to the experimental data measured in dry air. It was also shown that those fitted circuit element values could be represented by the small-signal model presented in Publication II and Section 2.3.

In the experiments in humid air the negative admittance effect was more pronounced. The admittance spectra of MOS1 sensor measured in clean humid air at various DC bias voltages are shown in Fig. 30. The EEC model of Fig. 8b was fitted to the experimental data in Fig. 30. The fitted circuit element values are shown in Fig. 31. Both the resistor R_b and the capacitor C_b are negative as shown in Fig. 31. Furthermore, the DC-bias dependence of R_b, C_b, and the time constant is in agreement with the formulas and the theoretical results in Publication II and Section 3.2. In Fig. 30 the real part of the admittance is positive. This indicates that the resistor R_{diff} dominates (Fig. 8 and Eq. 37). In dry air the imaginary part of admittance is positive [Publication VI], whereas in humid air, Fig. 30, it is negative. This indicates that the GB potential barrier modulation R_{mod}–L_{mod} circuit branch dominates in dry air and the charging and discharging circuit branch R_{char}–C_{char} in humid air conditions.

In order to explain the spectra measured in humid air and the fitted circuit element values, the model of Section 2.3, should have an extraordinary high charging and discharging current. This suggests that the electron trapping in GB states takes place in a much larger area than in the path of the electric current, indicating ion movement along the grain boundaries. An alternative explanation could be that water molecules alter the electronic trapping process in such a way that the rate equation describing the trapping (Eq. 44) changes into a form where R_b and C_b are negative. This rate equation should show stronger voltage dependence than Eq. 44.

In Refs. [109, 110] the negative admittance effect was explained by the movement of ions alone. However, our results suggest that the main causes of the negative admittance and capacitance effects are the barrier modulation and the charging properties of the grain-boundary region, whereas the ions provide enhancement of the charging and discharging component only. This explanation is in agreement with the work of Greuter and Blatter [1], where they explained that the negative admittance effect originates from the fundamental properties of granular semiconductors. Greuter and Blatter suggest, however, that the negative capacitance effect arises only at high voltages due to minority carrier effects [1].

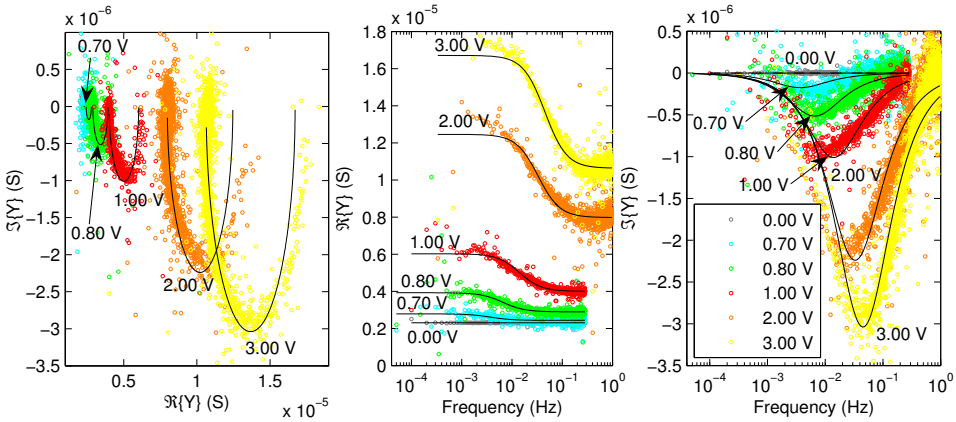

Figure 30: Measured and fitted admittance spectra of MOS1 sensor in humid clean air (30–40 %RH) measured at various DC bias voltages at 300 °C [Publication VI]. The Cole-Cole plot (*left*) is shown, and the real (*middle*) and the imaginary (*right*) parts of admittance are plotted against the frequency. The fitted spectra were calculated with the fitted circuit element values shown in Fig. 31.

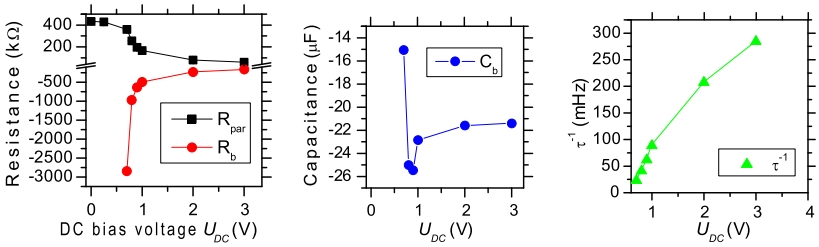

Figure 31: Fitted values of the resistors R_{par} and R_b, the capacitor C_b, and the inverse of the time constant $\tau = R_b C_b$ of the EEC model of Fig. 8b as functions of the DC bias voltage [Publication VI].

Future work

Ideas for further studies:

- **Fabrication of good samples for further testing the model.** The use of commercial gas sensors has several drawbacks: The manufacturers do not report all the details of their gas sensors and gas-sensing materials, the study of the sensing materials with more sophisticated techniques is not possible due to the packaging, and the microhotplate sensors inheritly have large parasitic capacitance which makes the measurement of higher frequency effects, such as the capacitance of the depletion region, challenging.
- **Inclusion of the effects of illumination and generation and recombination of charge carriers in the grain-boundary region [42, 113] to the model.**
- **Extension of the model to nanosized grains.** There has already been some work in this field [34–36, 114]. However, for example, the effect of applied voltage in nanograin materials has not yet been studied. In addition, quantum effects should be taken into account when the grain size is below 10 nm [36].
- **Use of the bias-voltage modulation in the selectivity improvement of metal-oxide gas sensors.** The results of the present thesis showed that the sensitivity of the metal-oxide gas sensors depends on the DC bias voltage used in the resistance measurement. This effect could be exploited in the selectivity improvement of these kinds of gas sensors.

Conclusions

A thorough modelling of DC, AC, and transient characteristics for granular n-type semiconductors using the diffusion theory was performed in the present thesis for the first time. The transient model describes the electrical large-signal response to both voltage and temperature changes. The analysis is based on the dynamic electrical model of the grain-boundary region and electronic trapping in the acceptor-type electronic interface states at the grain boundaries.

The accuracy of the models presented in the present thesis depends on the approximations made in the derivation of each model. The models were verified by performing numerical device simulations with SILVACO ATLAS. The DC results show that the semianalytical model is accurate in a large voltage range. Compared to the linear grain-boundary potential profile used in the calculations, the use of the quadratic grain-boundary potential profile gives only a slight improvement over the linear one. The simple approximative formulas work well at low voltages and the analytical model at very low voltages only (e.g. less than 60% and 20% of the maximum grain-boundary potential barrier height, which corresponds to the filled grain-boundary states). The AC results show that the analytical electrical equivalent circuit model works well at a very broad frequency range (e.g. 1–10^{12} Hz) at low DC bias voltages (e.g. less than 20% of the maximum grain-boundary potential barrier height).

The transient results show that the semianalytical model is accurate for the whole duration of the transients up to moderate applied voltages (e.g. 130% of the maximum grain-boundary potential barrier height). The approximative analytical formulas describing the electrical response are accurate only when the voltage and temperature changes are small (e.g. the grain-boundary trap occupancy changes by less than 0.005 during the transient). Therefore, the semianalytical model allows a fast and much more accurate calculation of transients. Compared to ATLAS the transient calculations employing the semianalytical model were 4 orders of magnitude faster on a standard PC computer, yet having the same accuracy. Because the semianalytical model allows rapid calculations, the fitting of the model to experimental transient data is possible within a reasonable time.

The semianalytical model was fitted to experimental DC and transient data measured from the ZnO powder samples reported in Ref. [14]. The model fits well to the data. Generally, all the presented modelling results are similar to those of other investigators, although the models by others are based on the thermionic-emission theory.

In general, the existence of electronic traps at grain boundaries of granular semiconductors results in nonlinear DC, extraordinary AC, and highly complex transient electrical characteristics. Based on the shapes of the I–V curves, the I–V curves can be divided into four characteristic regions: linear, sublinear, superlinear, and series resistance limited regions. The electrical-equivalent-circuit presentations of the AC characteristics have, in addition to the common resistors and capacitors, special RL and RC circuit branches associated with electronic trapping at the grain boundaries. These special circuit branches have negative admittance. The electrical transients are complex and nonlinear as they vary highly in both duration and magnitude. All of these electrical characteristics originate from the fact that the grain-boundary electronic traps are intrinsically coupled to the grain-boundary potential barrier which exponentially controls the flow of electric current through the grain boundary.

In the experimental part of the present thesis, focusing on resistive metal-oxide based gas sensors, an ALD SnO_2 gas-sensing film was used in a microhotplate gas sensor for the first time. Due to the special demands of the ALD process, new solutions were required for the design and the fabrication sequence, including film patterning methods and reordering of process steps. It was demonstrated that devices with ALD SnO_2 gas-sensing films exhibit good response and recovery to ethanol, acetone, and acrylonitrile vapours, as well as show good stability.

The model of granular semiconductors presented in the first half of this thesis was extended to the case of n-type surface-sensitive metal oxides, which are common materials utilized in gas sensors. In the model the adsorption of gases is described by a surface-state model. The model was employed in the quantitative explanation of the bias-dependent sensitivity effect in metal-oxide gas sensors, which was also observed experimentally in commercial WO_3 gas sensors. According to the model the effect is caused by DC electrical properties of granular metal oxide material in the case, where the electronic grain-boundary trap states (i.e. oxygen ions adsorbed at the grain boundaries) are mostly filled in the thermodynamical equilibrium in clean air.

Typically metal-oxide gas sensors have poor selectivity. The results of this thesis suggest that the bias-dependent sensitivity effect could be exploited in the improvement of the selectivity of the metal-oxide gas sensors. An increase in the selectivity could be achieved, for example, by using a bias-voltage modulation during the gas sensor operation.

Granular semiconductors exhibit another effect in metal-oxide gas sensors: the negative admittance effect. It was reported for the first time in metal oxide gas sensors

in the present thesis. The results show that the current component related to the modulation of the grain-boundary barrier dominates in dry clean air and the charging or discharging current dominates in humid air. The gas sensor response in dry clean air was in agreement with the present model, but additional ion motion coupled to the model was needed for the explanation of the strong charging current in humid air.

In conclusion, the present thesis gives a good basis for the modelling of all devices and sensors based on granular semiconductors. The models were already employed for successfully explaining the new effects observed in metal-oxide gas sensors.

References

[1] F. Greuter and G. Blatter, "Electrical properties of grain boundaries in polycrystalline compound semiconductors," *Semiconductor Science and Technology*, vol. 5, pp. 111–137, 1990.

[2] J. W. Orton and M. J. Powell, "The Hall effect in polycrystalline and powdered semiconductors," *Reports on Progress in Physics*, vol. 43, pp. 1263–1307, 1980.

[3] A. Many, Y. Goldstein, and N. B. Grover, *Semiconductor Surfaces*. Amsterdam, The Netherlands: North-Holland Publishing Company, 1965.

[4] H. Lüth, *Solid surfaces, interfaces and thin films*. Berlin, Germany: Springer, 4th ed., 2001.

[5] T. Wolkenstein, *Electronic Processes on Semiconductor Surfaces during Chemisorption*. New York, USA: Plenum Publishing Corporation, 1991.

[6] C. R. M. Grovenor, "Grain boundaries in semiconductors," *Journal of Physics C: Solid State Physics*, vol. 18, pp. 4079–4119, 1985.

[7] C. O. Park and S. A. Akbar, "Ceramics for chemical sensing," *Journal of Materials Science*, vol. 38, pp. 4611–4637, 2003.

[8] G. Eranna, B. C. Joshi, D. P. Runthala, and R. P. Gupta, "Oxide materials for development of integrated gas sensors - a comprehensive review," *Critical Reviews in Solid State and Materials Sciences*, vol. 29, pp. 111–188, 2004.

[9] P. R. Bueno, J. A. Varela, and E. Longo, "SnO_2, ZnO and related polycrystalline compound semiconductors: An overview and review on the voltage-dependent resistance (non-ohmic) feature," *Journal of the European Ceramic Society*, vol. 28, pp. 505–529, 2008.

[10] D. Kohl, "Function and applications of gas sensors," *Journal of Physics D: Applied Physics*, vol. 34, pp. R125–R149, 2001.

[11] I. Simon, N. Bârsan, M. Bauer, and U. Weimar, "Micromachined metal oxide gas sensors: opportunities to improve sensor performance," *Sensors and Actuators B: Chemical*, vol. 73, pp. 1–26, 2001.

[12] N. Barsan and U. Weimar, "Conduction model of metal oxide gas sensors," *Journal of Electroceramics*, vol. 7, pp. 143–167, 2001.

[13] Silvaco Data Systems Inc. `http://www.silvaco.com/`.

[14] P. F. Tua, M. Rossinelli, and F. Greuter, "Transient response of electrically active grain boundaries in polycrystalline semiconductors," *Physica Scripta*, vol. 38, pp. 491–497, 1988.

[15] J. W. Gardner, V. K. Varadan, and O. O. Awadelkarim, *Microsensors, MEMS, and Smart Devices*. New York, USA: John Wiley & Sons Ltd, 2001.

[16] J. W. Essam, "Percolation theory," *Reports on Progress in Physics*, vol. 43, pp. 833–912, 1980.

[17] S. Kirkpatrick, "Percolation and conduction," *Reviews of Modern Physics*, vol. 45, pp. 574–588, 1973.

[18] M. Sahimi, *Applications of Percolation Theory*. London, UK: Taylor & Francis, 1994.

[19] J. P. Clerc, G. Giraud, J. M. Laugier, and J. M. Luck, "The electrical conductivity of binary disordered systems, percolation clusters, fractals and related models," *Advances is Physics*, vol. 39, no. 3, pp. 191–309, 1990.

[20] R. Landauer, "The electrical resistance of binary metallic mixtures," *Journal of Applied Physics*, vol. 23, pp. 779–784, 1952.

[21] W. R. Tinga, W. A. G. Voss, and D. F. Blossey, "Generalized approach to multiphase dielectric mixture theory," *Journal of Applied Physics*, vol. 44, no. 9, pp. 3897–3902, 1973.

[22] J. Helsing and A. Helte, "Effective conductivity of aggregates of anisotropic grains," *Journal of Applied Physics*, vol. 69, no. 6, pp. 3583–3588, 1991.

[23] G. Dezanneau, A. Morata, A. Tarancón, M. Salleras, F. Peiró, and J. R. Morante, "Grain-boundary resistivity versus grain size distribution in three-dimensional polycrystals," *Applied Physics Letters*, vol. 88, p. 141920, 2006.

[24] J. Fleig and J. Maier, "A finite element study on the grain boundary impedance of different microstructures," *Journal of The Electrochemical Society*, vol. 145, pp. 2081–2089, 1998.

[25] J. Sinkkonen, "DC conductivity of a random barrier network," *Physica Status Solidi (b)*, vol. 102, pp. 621–627, 1980.

[26] L. Sali and D. J. Bergman, "Effective medium approximation for strongly nonlinear media," *Journal of Statistical Physics*, vol. 86, pp. 455–479, 1997.

[27] K. W. Yu and G. Q. Gu, "Effective conductivity of nonlinear composites. II. Effective-medium approximation," *Physical Review B*, vol. 47, no. 12, pp. 7568–7571, 1993.

[28] W. En-bo, S. Jin-bao, and G. Guo-qing, "Effective response of a non-linear composite in external AC electric field," *Physica B*, vol. 324, pp. 322–328, 2002.

[29] J. Ding, T. J. McAvoy, R. E. Cavicchi, and S. Semancik, "Surface state trapping models for SnO_2-based microhotplate sensors," *Sensors and Actuators B: Chemical*, vol. 77, pp. 597–613, 2001.

[30] F. F. Vol'kenshtein, *The Electronic Theory of Catalysis on Semiconductors*. New York, USA: Pergamon Press Ltd., 1963.

[31] D. K. Schroder, *Semiconductor material and device characterization*. Hoboken, USA: Wiley-Interscience, 3rd ed., 2006.

[32] A. Oprea, E. Moretton, N. Bârsan, W. J. Becker, J. Wöllenstein, and U. Weimar, "Conduction model of SnO_2 thin films based on conductance and Hall effect measurements," *Journal of Applied Physics*, vol. 100, no. 033716, 2006.

[33] B. Kamp, R. Merkle, R. Lauck, and J. Maier, "Chemical diffusion of oxygen in tin dioxide: Effects of dopants and oxygen partial pressure," *Journal of Solid State Chemistry*, vol. 178, pp. 3027–3039, 2005.

[34] A. Rothschild and Y. Komem, "On the relationship between the grain size and gas-sensitivity of chemo-resistive metal-oxide gas sensors with nanosized grains," *Journal of Electroceramics*, vol. 13, pp. 697–701, 2004.

[35] N. Yamazoe and K. Shimanoe, "Receptor function of small semiconductor crystals with clean and electron-traps dispersed surfaces," *Thin Solid Films*, vol. 517, pp. 6148–6155, 2009.

[36] V. Guidi, M. Carotta, C. Malagù, and G. Martinelli, "Modeling of the inter-granular energy-barrier height in very-fine nanograins through a semi-classical approach," *Sensors and Actuators B: Chemical*, vol. 137, pp. 521–523, 2009.

[37] J. Vanderlinde, *Classical Electromagnetic Theory*. Kluwer, 2nd ed., 2004.

[38] S. M. Sze, *Physics of Semiconductor Devices*. New York, USA: Wiley-Interscience, 2nd ed., 1981.

[39] K. Ellmer and R. Mientus, "Carrier transport in polycrystalline ITO and ZnO:Al II: The influence of grain barriers and boundaries," *Thin Solid Films*, vol. 516, pp. 5829–5835, 2008.

[40] A. Varpula, "Modelling of electrical properties of granular semiconductors," Licentiate's thesis, Helsinki University of Technology, 2009.

[41] E. W. Weisstein, "Erfi," 2004. From MathWorld
http://mathworld.wolfram.com/Erfi.html.

[42] J. Sinkkonen, S. Novikov, A. Varpula, and J. Haapamaa, "Characterization of epiready n^+-GaAs (100) surfaces by SPV-transient," *Proceedings of SPIE*, vol. 6800, p. 68001D, 2008.

[43] A. Rothschild and Y. Komem, "Numerical computation of chemisorption isotherms for device modeling of semiconductor gas sensors," *Sensors and Actuators B: Chemical*, vol. 93, pp. 362–369, 2003.

[44] K. W. Böer, *Survey of Semiconductor Physics, Volume II.* New York, USA: Van Nostrand Reinhold, 1992.

[45] I. V. Rozhansky and D. A. Zakheim, "Modeling of the electrical properties of polycrystalline ceramic semiconductors with submicron grains," *Microelectronic Engineering*, vol. 81, pp. 494–502, 2005.

[46] J. Guérin, K. Aguir, and M. Bendahan, "Modeling of the conduction in a WO_3 thin film as ozone sensor," *Sensors and Actuators B: Chemical*, vol. 119, pp. 327–334, 2006.

[47] The MathWorks Inc. http://www.mathworks.com/.

[48] P. Godfrey and P. J. Acklam, "erfz, error function for complex inputs implemented in MATLAB." Available at MATLAB Central,
http://www.mathworks.com/matlabcentral/fileexchange/3574, 2001.

[49] G. Blatter and F. Greuter, "Carrier transport through grain boundaries in semiconductors," *Physical Review B*, vol. 33, no. 6, pp. 3952–3966, 1986.

[50] A. Broniatowski, "Measurement of the grain-boundary states in semiconductors by deep-level transient spectroscopy," *Physical Review B*, vol. 36, no. 11, pp. 5895–5905, 1987.

[51] R. Ionescu, E. Llobet, S. Al-Khalifa, J. W. Gardner, X. Vilanova, J. Brezmes, and X. Correig, "Response model for thermally modulated tin oxide-based microhotplate gas sensors," *Sensors and Actuators B: Chemical*, vol. 95, pp. 203–211, 2003.

[52] A. Fort, S. Rocchi, M. B. Serrano-Santos, M. Mugnaini, V. Vignoli, A. Atrei, and R. Spinicci, "CO sensing with SnO_2-based thick film sensors: Surface state model for conductance responses during thermal-modulation," *Sensors and Actuators B: Chemical*, vol. 116, pp. 43–48, 2006.

[53] A. Fort, M. Mugnaini, S. Rocchi, M. B. Serrano-Santos, V. Vignoli, and R. Spinicci, "Simplified models for SnO_2 sensors during chemical and thermal transients in mixtures of inert, oxidizing and reducing gases," *Sensors and Actuators B: Chemical*, vol. 124, pp. 245–259, 2007.

[54] A. Fort, S. Rocchi, M. B. Serrano-Santos, R. Spinicci, and V. Vignoli, "Surface state model for conductance responses during thermal-modulation of SnO_2-based thick film sensors: Part I–model derivation," *IEEE Transactions on Instrumentation and Measurement*, vol. 55, no. 6, pp. 2102–2106, 2006.

[55] A. Fort, M. Mugnaini, S. Rocchi, M. B. Serrano-Santos, R. Spinicci, and V. Vignoli, "Surface state model for conductance responses during thermal-modulation of SnO_2-based thick film sensors: Part II–experimental verification," *IEEE Transactions on Instrumentation and Measurement*, vol. 55, no. 6, pp. 2107–2117, 2006.

[56] K. Ihokura and J. Watson, *The stannic oxide gas sensors: principles and applications*. Boca Raton, USA: CRC Press, 4th ed., 1994.

[57] H. Nanto and J. R. Stetter, "Introduction to chemosensors," in *Handbook of Machine Olfaction - Electronic Nose Technology* (T. C. Pearce, S. S. Schiffman, H. T. Nagle, and J. W. Gardner, eds.), ch. 4, pp. 79–104, Darmstadt, Germany: Wiley-VCH, 2003.

[58] D.-D. Lee and D.-S. Lee, "Environmental gas sensors," *IEEE Sensors Journal*, vol. 1, no. 3, pp. 214–224, 2001.

[59] G. Korotcenkov, "Metal oxides for solid-state gas sensors: What determines our choice?," *Materials Science and Engineering B*, vol. 139, pp. 1–23, 2007.

[60] T. C. Pearce, S. S. Schiffman, H. T. Nagle, and J. W. Gardner, eds., *Handbook of Machine Olfaction - Electronic Nose Technology*. Darmstadt, Germany: Wiley-VCH, 2003.

[61] N. Yamazoe, "Towards innovations of gas sensor technology," *Sensors and Actuators B: Chemical*, vol. 108, pp. 2–14, 2005.

[62] P. T. Moseley, "Solid state gas sensors," *Measurement Science and Technology*, vol. 8, pp. 223–237, 1997.

[63] P. Mielle, "Practical aspects in design of the one-electrode semiconductor gas sensors: Status report," *Sensors and Actuators B: Chemical*, 2006. In press.

[64] P. Corcoran, H. V. Shurmer, and J. W. Gardner, "Integrated tin oxide sensors of low power consumption for use in gas and odour sensing," *Sensors and Actuators B: Chemical*, vol. 15, pp. 32–37, 1993.

[65] G. Korotcenkov, "Gas response control through structural and chemical modification of metal oxide films: state of the art and approaches," *Sensors and Actuators B: Chemical*, vol. 107, pp. 209–232, 2005.

[66] J. W. Gardner and M. Cole, "Integrated electronic noses and microsystems for chemical analysis," in *Handbook of Machine Olfaction - Electronic Nose Technology* (T. C. Pearce, S. S. Schiffman, H. T. Nagle, and J. W. Gardner, eds.), ch. 10, pp. 231–266, Darmstadt, Germany: Wiley-VCH, 2003.

[67] D. Barrettino, M. Graf, M. Zimmermann, C. Hagleitner, A. Hierlemann, and H. Baltes, "A smart single-chip micro-hotplate-based gas sensor system in CMOS-technology," *Analog Integrated Circuits and Signal Processing*, vol. 39, pp. 275–287, 2004.

[68] J. Sundqvist, J. Lu, M. Ottosson, and A. Hårsta, "Growth of SnO_2 thin films by atomic layer deposition and chemical vapour deposition: A comparative study," *Thin Solid Films*, vol. 514, pp. 63–68, 2006.

[69] G. Sberveglieri, G. Faglia, S. Gropelli, P. Nelli, and A. Camanzi, "A new technique for growing large surface area SnO_2 thin film (RGTO technique)," *Semiconductor Science and Technology*, vol. 5, pp. 1231–1233, 1990.

[70] A. Diéguez, A. Romano-Rodríguez, J. R. Morante, P. Nelli, L. Sangaletti, and G. Sberveglieri, "Analysis of the thermal oxidation of tin droplets and its implications on gas sensor stability," *Journal of The Electrochemical Society*, vol. 146, no. 9, pp. 3527–3535, 1999.

[71] S. Z. Ali, F. Udrea, W. I. Milne, and J. W. Gardner, "Tungsten-based SOI microhotplates for smart gas sensors," *Journal of Microelectromechanical Systems*, vol. 17, no. 6, pp. 1408–1417, 2008.

[72] P. Fau, M. Sauvan, S. Trautweiler, C. Nayral, L. Erades, A. Maisonnat, and B. Chaudret, "Nanosized tin oxide sensitive layer on a silicon platform for domestic gas applications," *Sensors and Actuators B: Chemical*, vol. 78, pp. 83–88, 2001.

[73] M. Graf, S. K. Müller, D. Barrettino, and A. Hierlemann, "Transistor heater for microhotplate-based metal-oxide microsensors," *IEEE Electron Device Letters*, vol. 26, no. 5, pp. 295–297, 2005.

[74] F. Udrea, S. Maeng, J. W. Gardner, J. Park, M. S. H. S. Z. Ali, Y. Choi, P. K. Guha, S. M. C. Vieira, H. Y. Kim, S. H. Kim, K. C. Kim, S. E. Moon, K. H. Park, W. I. Milne, and S. Y. Oh, "Three technologies for a smart miniaturized gas-sensor: SOI CMOS, micromachining, and CNTs - challenges and performance," in *Electron Devices Meeting, 2007. IEDM 2007.*, IEEE International, Dec 2007.

[75] P. K. Guha, S. Z. Ali, C. C. C. Lee, F. Udrea, W. I. Milne, T. Iwaki, J. A. Covington, and J. W. Gardner, "Novel design and characterisation of SOI CMOS microhotplates for high temperature gas sensors," *Sensors and Actuators B: Chemical*, vol. 127, pp. 260–266, 2007.

[76] D. Briand, S. Heimgartner, M.-A. Grétillat, B. van der Schoot, and N. F. de Rooij, "Thermal optimization of micro-hotplates that have a silicon island," *Journal of Micromechanics and Microengineering*, vol. 12, pp. 971–978, 2002.

[77] S. Ahlers, T. Becker, W. Hellmich, C. Bosch-v. Braunmühl, and G. Müller, "Temperature- and field-effect-modulation techniques for thin-film metal oxide gas sensors," in *Advanced Gas Sensing – The Electroadsorptive Effect and Related Techniques* (T. Doll, ed.), ch. 6, pp. 123–159, Norwell, MA, USA: Kluwer Academic Publishers, 2003.

[78] S. Nakata, H. Okunishi, and S. Inooka, "Gas-sensing system based on the cyclic temperature: Further characterization by the second harmonic perturbation," *Analytica Chimica Acta*, vol. 517, pp. 153–159, 2004.

[79] S. Nakata, H. Okunishi, and Y. Nakashima, "Distinction of gases with a semiconductor sensor under a cyclic temperature modulation with second-harmonic heating," *Sensors and Actuators B: Chemical*, vol. 119, pp. 556–561, 2006.

[80] A. Hierlemann and R. Gutierrez-Osuna, "Higher-order chemical sensing," *Chemical Reviews*, vol. 108, no. 2, pp. 563–613, 2008.

[81] A. P. Lee and B. J. Reedy, "Temperature modulation in semiconductor gas sensing," *Sensors and Actuators B: Chemical*, vol. 60, pp. 35–42, 1999.

[82] D. Briand, A. Krauss, B. van der Schoot, U. Weimar, N. Barsan, W. Göpel, and N. de Rooij, "Design and fabrication of high temperature micro-hotplates for drop coated gas sensors," *Sensors and Actuators B: Chemical*, vol. 68, pp. 223–233, 2000.

[83] B. H. Weiller, P. D. Fuqua, and J. V. Osborn, "Fabrication, characterization, and thermal failure analysis of a micro hot plate chemical sensor substrate," *Journal of The Electrochemical Society*, vol. 151, no. 3, pp. 59–63, 2004.

[84] M. Hausner, U. Storm, H. Karagözoglu, J. Zacheja, and J. Binder, "Air monitoring by a combined resistive and field effect sensor device," in *Digest of Techinical Papers Vol. 2*, pp. 963–966, Transducers '97, 1997.

[85] M. Hausner, J. Zacheja, and J. Binder, "Multi-electrode substrate for selectivity enhancement in air monitoring," *Sensors and Actuators B: Chemical*, vol. 43, pp. 11–17, 1997.

[86] W. Hellmich, G. Müller, C. Bosch-v. Braunmühl, T. Doll, and I. Eisele, "Field-effect-induced gas sensitivity changes in metal oxides," *Sensors and Actuators B: Chemical*, vol. 43, pp. 132–139, 1997.

[87] Y. N. Kunishima, M. Miyayama, and H. Yanagida, "Effects of the external electric field from a substrate on conductance changes of SnO_2 thin films by CO gas," *Japanese Journal of Applied Physics*, vol. 35, pp. 3478–3482, 1996.

[88] M. Hausner, U. Storm, O. Bartels, and J. Binder, "Multielectrode micromachined gas sensors," in *Advanced Gas Sensing – The Electroadsorptive Effect and Related Techniques* (T. Doll, ed.), ch. 5, pp. 101–121, Norwell, MA, USA: Kluwer Academic Publishers, 2003.

[89] D. Briand, S. Colin, A. Gangadharaiah, E. Vela, P. Dubois, L. Thiery, and N. F. de Rooij, "Micro-hotplates on polyimide for sensors and actuators," *Sensors and Actuators A: Physical*, vol. 132, pp. 317–324, 2006.

[90] K. Kovács, M. Utriainen, C. Dücsô, E. B. Várhegyi, M. Ádám, L. Niinistö, and F. Réti, "Gas sensitive SnO_2 thin films by atomic layer epitaxy," in *Proceedings of the 6th NEXUSPAN Workshop*, (Vilnius, Lithuania), pp. 89–91, 1999.

[91] A. Rosental, A. Tarre, A. Gerst, T. Uustare, and V. Sammelselg, "Atomic-layer chemical vapor deposition of SnO_2 for gas-sensing applications," *Sensors and Actuators B: Chemical*, vol. 77, pp. 297–300, 2001.

[92] X. Du and S. M. George, "Thickness dependence of sensor response for CO gas sensing by tin oxide films grown using atomic layer deposition," *Sensors and Actuators B: Chemical*, vol. 135, pp. 152–160, 2008.

[93] S. Mishra, C. Ghanshyam, N. Ram, S. Singh, R. P. Bajpai, and R. K. Bedi, "Alcohol sensing of tin oxide thin film prepared by sol-gel process," *Bulletin of Materials Science*, vol. 25, no. 3, pp. 231–234, 2002.

[94] S. Gomri, J.-L. Seguin, J. Guerin, and K. Aguir, "A mobility and free carriers density fluctuations based model of adsorption-desorption noise in gas sensor," *Journal of Physics D: Applied Physics*, vol. 41, p. 065501, 2008.

[95] J. Guérin, M. Bendahan, and K. Aguir, "A dynamic response model for the WO_3-based ozone sensors," *Sensors and Actuators B: Chemical*, vol. 128, pp. 462–467, 2008.

[96] U. Pulkkinen, T. T. Rantala, T. S. Rantala, and V. Lantto, "Kinetic Monte Carlo simulation of oxygen exchange of SnO_2 surface," *Journal of Molecular Catalysis A: Chemical*, vol. 166, pp. 15–21, 2001.

[97] T. S. Rantala, V. Lantto, and T. T. Rantala, "Rate equation simulation of the height of Schottky barriers at the surface of oxidic semiconductors," *Sensors and Actuators B: Chemical*, vol. 13-14, pp. 234–237, 1993.

[98] A. Rothschild, Y. Komem, and N. Ashkenasy, "Quantitative evaluation of chemisorption processes on semiconductors," *Journal of Applied Physics*, vol. 92, no. 12, pp. 7090–7097, 2002.

[99] P. K. Clifford and D. T. Tuma, "Characteristics of semiconductor gas sensors I. Steady state gas response," *Sensors and Actuators*, vol. 3, pp. 233–254, 1983.

[100] P. K. Clifford and D. T. Tuma, "Characteristics of semiconductor gas sensors II. Transient response to temperature change," *Sensors and Actuators*, vol. 3, pp. 255–281, 1983.

[101] N. Barsan, M. Schweizer-Berberich, and W. Göpel, "Fundamental and practical aspects in the design of nanoscaled SnO_2 gas sensors: a status report," *Fresenius' Journal of Analytical Chemistry*, vol. 365, pp. 287–304, 1999.

[102] M. Batzill and U. Diebold, "The surface and materials science of tin oxide," *Progress in Surface Science*, vol. 79, pp. 47–154, 2005.

[103] L. Gajdošík, "The concentration measurement with SnO_2 gas sensor operated in the dynamic regime," *Sensors and Actuators B: Chemical*, vol. 106, pp. 691–699, 2005.

[104] S. M. A. Durrani, "Biasing voltage dependence of sensitivity of electron beam evaporated SnO_2 thin film CO sensor," *Sensors*, vol. 6, pp. 1153–1160, 2006.

[105] S. M. A. Durrani and M. F. Al-Kuhaili, "Effect of biasing voltages and electrode metals and materials on the sensitivity of electron beam evaporated HfO_2 thin film CO sensor," *Materials Chemistry and Physics*, vol. 109, pp. 56–60, 2008.

[106] Environics Oy. `http://www.environics.fi/`.

[107] M. Ershov, H. C. Liu, L. Li, M. Buchanan, Z. R. Wasilewski, and A. K. Jonscher, "Negative capacitance effect in semiconductor devices," *IEEE Transactions on Electron Devices*, vol. 45, no. 10, pp. 2196–2206, 1998.

[108] L. S. C. Pingree, B. J. Scott, M. T. Russell, T. J. Marks, and M. C. Hersam, "Negative capacitance in organic light-emitting diodes," *Applied Physics Letters*, vol. 86, p. 073509, 2005.

[109] O. K. Varghese and L. K. Malhotra, "Studies of ambient dependent electrical behavior of nanocrystalline SnO_2 thin films using impedance spectroscopy," *Journal of Applied Physics*, vol. 87, no. 10, pp. 7457–7465, 2000.

[110] M. Kaur, S. K. Gupta, C. A. Betty, V. Saxena, V. R. Katti, S. C. Gadkari, and J. V. Yakhmi, "Detection of reducing gases by SnO_2 thin films: an impedance spectroscopy study," *Sensors and Actuators B: Chemical*, vol. 107, pp. 360–365, 2005.

[111] S. K. Mitra, *Digital signal processing: a computer-based approach*. Singapore: McGraw-Hill, 1998.

[112] National Instruments Corporation, "Windowing: Optimizing FFTs using window functions," 2006. Web published at `http://zone.ni.com/devzone/cda/tut/p/id/4844#2`.

[113] H. F. Mataré, "Enhanced carrier collection at grain-boundary barriers in solar cells made from large grain polycrystalline material," *Solid-State Electronics*, vol. 22, pp. 651–658, 1979.

[114] C. Malagù, G. Martinelli, M. A. Ponce, and C. M. Aldao, "Unpinning of the Fermi level and tunneling in metal oxide semiconductors," *Applied Physics Letters*, vol. 92, p. 162104, 2008.

The electrical properties of granular semiconductors are modelled. The developed models allow predicting DC, AC and transient characteristics of these granular materials. They give as accurate results as commercial software, but several orders of magnitude faster. Granular semiconductors are widely used in, e.g., microelectronic circuits and solar cells. Electric current in them depends strongly on the potential barriers at grain boundaries. This results in extraordinary electrical properties, which are utilized in, e.g., varistors and gas sensors. Gas-sensor applications range from toxic-gas detection to electronic noses used for, e.g., diagnosing diseases and assessing wine quality. Gas-sensing granular semiconductors are metal oxides such as tin dioxide, which is used in the presented micro-gas sensor. Two new phenomena in gas sensors, the bias-voltage dependent sensitivity and the negative admittance, were discovered and modelled in the present thesis.

Aalto-DD 21/2011

ISBN: 978-952-60-4063-9 (pdf)
ISBN: 978-952-60-4062-2
ISSN-L: 1799-4934
ISSN: 1799-4942 (pdf)
ISSN: 1799-4934

Aalto University
School of Electrical Engineering
Department of Micro and Nanosciences
aalto.fi

BUSINESS + ECONOMY

ART + DESIGN + ARCHITECTURE

SCIENCE + TECHNOLOGY

CROSSOVER

DOCTORAL DISSERTATIONS